UNIVERSITY OF CALIFORNIA SAN DIEGO

Engineering Active Transdermal Systems with Enhanced Targeted Drug Delivery

A dissertation submitted in partial satisfaction of the
requirements for the degree Doctor of Philosophy

in

Nanoengineering

by

Miguel Angel Lopez Ramirez

Committee in charge:

Professor Joseph Wang, Chair
Professor Silvio Gutkind
Professor Tina Ng
Professor Nisarg Shah
Professor Liangfang Zhang

2021

The dissertation of Miguel Angel Lopez Ramirez is approved,
and it is acceptable in quality and form for publication
on microfilm and electronically.

University of California San Diego

2021

DEDICATION

This thesis is dedicated to my beloved family. First and foremost, my parents, who have been the source of inspiration and support since this engineering journey started a decade ago. During my academic and professional life have been always present, from the worst to the most exciting/challenging events of my life. Without your enormous and unconditional love and support I would not become the individual that I am today.

During my PhD journey, I have had the opportunity to learn and grow not only as a professional, but as a parent. These 5 years have given me the opportunity to get to know extraordinary and beautiful little human beings, but more importantly, to learn the kindness, patience, naivety, and unconditional love that I could ever imagine. I owe thanks to my wife, for her restless moral and emotional support, continued and unfailing love and understanding through all my travails, my absences and impatience. I could not have done it without you.

EPIGRAPH

“That, finally, the door opens . . .

and it opens outward, we’ve been

inside what we wanted all along.”

David Foster Wallace

TABLE OF CONTENTS

LIST OF FIGURES

LIST OF TABLES

ACKNOWLEDGEMENTS

I want to acknowledge my advisor Joseph Wang for granting me this once in a life changing opportunity to grow as a professional and as a person; nothing of this could be possible without the unconditional help since I embarked in this Ph.D. journey. The experiences at UCSD have shown me the importance of having inspiring team members and friends, that have allowed me to grow professionally as a scientist/engineer.

I would like to thank my lab mates (postdocs, grad students, and undergrads) who made numerous contributions to my research projects, and those who taught me everything, friendship, scientific knowledge, and where always helpful since my first day of arrival (Berta and Fernando). I would not have been able to accomplish what I have done so far without their high standard contributions, patience, and dedicated time.

I feel grateful for the advice and support of my committee, and owe special thanks to Dana Jimenez, who always was present when help was needed.

My life has changed since I was granted the opportunity to become part of the triton family. UCSD is a great and outstanding place to follow your professional dreams, comprised of brilliant students, accommodations, and faculty. I was blessed to be part of great research at the nanoengineering department, but to meet exceptional people across different backgrounds and countries. I want to thank everyone from UCSD school of medicine and Moore's Cancer Center for your valuable help during my Ph.D., where we successfully achieved great collaborations.

In addition, I would like to thank the MEXUS-CONACYT fellowship for providing financial support for my graduate studies.

This accomplishment was possible thanks to the unconditional support and encouragement of my family: my parents, wife and kids, a key and very important part of my life, who gives me balance, joy, and strength.

Chapter 2.1 and 2.2 are based, in part, on the material as appears in Advanced Materials, 2020, by Miguel Angel Lopez Ramirez, Fernando Soto, Chao Wang, Ricardo Rueda, Sourabh Shukla, Cristian Silva Lopez, Daniel Kupor, David A. McBride, Jonathan K. Pokorski, Amir Nourhani, Nicole F. Steinmetz, Nisarg J. Shah, Joseph Wang. The dissertation author was the primary investigator and author of this paper.

Chapter 2.3 is based, in part, on the material as appears in ACS Applied Nano Materials, 2020, by Christine E. Boone, Chao Wang, Miguel Angel Lopez Ramirez, Veronique Beiss, Sourabh Shukla, Paul L. Chariou, Daniel Kupor, Ricardo Rueda, Joseph Wang, Nicole F. Steinmetz. The dissertation author was a coauthor of this paper.

Chapter 3 is based, in part, on the material as appears in Journal of Materials Chemistry B, 2021, by Miguel Angel Lopez Ramirez, Daniel Kupor, Leonardo Marchiori, Fernando Soto, Ricardo Rueda, Maria Reynoso, Lakshmi Rekha Narra, Krishnan Chakravarthy, Joseph Wang. The dissertation author was the primary investigator and author of this paper.

Chapter 4 is based, in part, on the material as appears in Advanced Materials, 2020, by Miguel Angel Lopez Ramirez, Fernando Soto, Chao Wang, Ricardo Rueda, Sourabh Shukla, Cristian Silva Lopez, Daniel Kupor, David A. McBride, Jonathan K. Pokorski, Amir Nourhani, Nicole F. Steinmetz, Nisarg J. Shah, Joseph Wang. The dissertation author was the primary investigator and author of this paper.

VITA

2015 Bachelor of Science, National Technological Institute of Mexico

2017 Master of Science, University of California San Diego

2021 Doctor of Philosophy, University of California San Diego

SELECTED PUBLICATIONS

1. Lopez-Ramirez, M. A., Soto, F., Wang, C., Rueda, R., Shukla, S., Silva-Lopez, C., Kupor, D., McBride, D. A., Pokorski, J. K., Nourhani, A., Steinmetz, N. F., Shah, N. J., Wang, J. Built-in active microneedle patch with enhanced autonomous drug delivery. *Advanced Materials*, **2020**. *32*, 1905740.
2. Boone, C. E., Wang, C., Lopez-Ramirez, M. A., Beiss, V., Shukla, S., Chariou, P. L., Kupor, D., Rueda, R., Wang, J., Steinmetz, N. F. Active microneedle administration of plant virus nanoparticles for cancer in situ vaccination improves immunotherapeutic efficacy. *ACS Applied Nano Materials*, **2020**, *3*, 8037-8051.
3. Lopez-Ramirez, M. A., Kupor, D., Marchiori, L., Soto, F., Rueda, R., Reynoso, M., Rekha-Narra, L., Chakravarthy, K., Wang, J. Combinatorial microneedle patch with tunable release kinetics and dual fast-deep/sustained release capabilities. *Journal of Materials Chemistry B*, **2021**. *9*, 2189-2199.

FIELD OF STUDY

Major Field: Nanoengineering, Bioengineering and Material Science

Studies in Nanoengineering

Professor Joseph Wang

ABSTRACT OF THE DISSERTATION

Engineering Active Transdermal Systems with Enhanced Targeted Drug Delivery

by

Miguel Angel Lopez Ramirez

Doctor of Philosophy in Nanoengineering

University of California San Diego, 2021

Professor Joseph Wang, Chair

Over the last decade, the use of microneedle devices has facilitated a painless localized and practical delivery of therapeutic payloads across the skin, with considerable promise in a variety of biomedical applications. However, their efficacy has been limited by the slow diffusion of molecules often requiring external actuation. This dissertation aims to demonstrate the unique advantages of active microneedle platforms.

The first theme focuses on the development of an autonomous and degradable, active microneedle platform for deeper and faster intradermal therapeutic delivery, and corresponding *in vivo* performance in a B16F10 mouse melanoma model.

The second theme explores a versatile and effective in situ active microneedle vaccination system for the direct intratumoral delivery of an immunoadjuvant, cowpea mosaic virus nanoparticles, *in vivo*.

The third theme describes a dual-action combinatorial programmable microneedle system by integrating fast and sustained-release compartments with tunable release kinetics. We demonstrate that the fine tuning of microneedle materials allows the device to be tailored to deliver initial payloads in minutes, while simultaneously deliver a second drug over prolonged period of times ranging from weeks to months.

Chapter 1. Introduction

1.1 Microneedle Platforms/Devices Opportunities and Challenges

The staggering rate of technological evolution and advancement in microfabrication methods over the last decade have left an unprecedented amount of exciting and remarkable technologies/devices that were previously thought impossible. Indeed, universally transformative breakthrough innovations in the healthcare sector that have impacted our lives and helped us live with greater ease.

The increasing decentralization of the healthcare sector towards home/community patient care has recently become more important and frequent during the last decade.[1-3] Even though oral administration is the most popular route[4] to deliver therapeutic agents due to its ease of ingestion, pain avoidance, versatility, and patient compliance, an estimated 16-23%[5,6] of the general population and 40-60%[7] of all patients in long-term care facilities suffer from dysphagia (difficulty in swallowing). When the administration of therapeutic agents is unsuitable through oral routes due to poor drug absorption or enzymatic degradation in the gastrointestinal tract or liver[8-10], an injection using a painful hypodermic needle is considered the primary option for clinical treatment purposes. The standard/hypodermic needle and syringe has become an invaluable practical tool enabling the delivery of a wide variety of therapeutic agents across diverse locations of the human body, because its simplicity, and straightforward usability.[11,12]

Despite widespread adoption of the needle and syringe in the clinical setting, this old technology has become key part where shortcomings arise in drug delivery applications

with many drawbacks and limitations. Among those are: the high possibility of needlestick injury (NSI) representing a recurrent hazard accounting 80% of percutaneous injuries[13], invasiveness, cross contamination (~1.3 million deaths per year)[14], fear to needles (needle phobia)[15,17], need to maintain the cold chain (logistical challenges, distribution, and storage) and generation of sharp bio-hazardous waste.

For thousands of years, humanity have employed wide variety of substances over the skin for therapeutic effects. The introduction and innovation in effective and practical needle-free delivery systems has grown substantially in recent years, becoming a reality in the clinical setting.[17] In the modern area, transdermal drug delivery systems (TDD)[18], a painless topical formulation alternative to both oral and needle-injection delivery has been developed for the local treatment of medical conditions. Indeed, they avoid hepatic first pass metabolism, however, lacks efficiency, as the outer corneocyte layer of the skin of ~15µm, stratum corneum (SC)[19-21] prevents and limits the diffusion of drugs to deeper areas of the skin of interest, where therapeutic drug absorption take effect.

Microneedle technologies, a minimally invasive approach, in contrast, have considerably captivated the attention of the healthcare community. They have overcome the skin permeability limitations of current delivery modalities, avoiding the firs-pass effect, eliminating the issue of needle phobia, targeting locally the therapeutic delivery diminishing side effects, reducing dosing frequency, easier application without the need of medical practitioners, but, more importantly, by eradicating the safety issues associated with the hollow bore stainless steel needles.[22-26]

Microneedles are micron-sized projections-like needles with different design and shape (conical, pyramidal, cylindrical), with typical lengths ranging from 100-1000μm, and much sharper tips when compared to standard gauge needles, used to disrupt/overpass the SC layer forming micro-scale channels, but without reaching capillaries, blood vessels nor nerve endings. As a result, an approach that increases therapeutic efficacy in a painless and minimally invasive manner. The state-of-the-art microneedles have proven successful a wide variety of biomedical applications ranging from transdermal drug delivery (e.g., diabetes, dermatological, cosmetic, immunotherapy, cancer, and vaccines) and global biologics market by sensing (blood sampling, signal monitoring and biosensors).[27-32] Additionally they have shown great promise in preclinical and clinical studies for vaccine delivery and insulin delivery.[33-35]

The biggest challenge in the effective use of microneedles relies in their composition. Microneedles should have appropriate combination of mechanical strength, along with adequate design, dimensions, needle density, and toughness for an efficient skin penetration. To design intelligent microneedle delivery systems with high reliability, these factors along with a wise material selection should be taken fully into account to effectively deliver therapeutic agents.[36,37]

1.2 Classification and Methods of Fabrication of Microneedle Devices

Microneedle technology has experienced an enormous progress over the past decades since the first demonstration. Microneedles can be classified based on multiple parameters, including material composition, structure/design, drug transportation method and manufacturing technique. A wide variety of microneedle designs have been

developed over the course of years: i.e., solid, hollow, dissolvable, swellable and porous. In general, microneedles can be made of a variety of materials. Researchers have devoted time towards making them biocompatible, or biodegradable; until now, made of silicone, metal, glass, ceramics, sugars, hydrogels, and polymers.[38-51] Silicon microneedles were developed in the very early stages; despite their outstanding hardness/mechanical properties to breach dermal barriers, the associated relation between cost to manufacture/performance ended up being expensive requiring cleanroom processing.[27,52] Metal microneedles can be manufactured at low costs by different traditional manufacturing techniques (e.g., micromilling, laser cutting, electroplating), however, despite their outstanding mechanical properties and safety profile (stainless steel, titanium), still produce bio-hazardous waste.[53,54]

Dissolvable microneedles have received tremendous attention from researchers and medical practitioners, as they are low cost to manufacture and are made of water-soluble biocompatible-degradable polymers that encapsulate therapeutic agents in a dry needle-like matrix. Polymers are considered the most promising material, as upon skin insertion, the polymer matrix dissolves over a timescale of minutes-hours, thus leaving behind no bio-hazardous-sharp waste after application.[55] In contrast to previous microneedle generations (silicon), polymers usually have high toughness, avoid fracture upon insertion to the skin and release therapeutic agents once the needle-like structure degrades or dissolves.

Various techniques are commonly employed for microneedle fabrication. Photolithography is a well stablished technology that involves the use of silicon wafers,

where either a positive or negative photoresist is coated, UV-lighted through a mask, and etched to form microneedle structures with specific thickness, size, and shape.[56-60] Even though this technique produces high quality-reproducible microneedle arrays, requires cleanroom access (complex, costly and time consuming) with narrow material selection.

In general, most polymers have a relative low melting temperature, therefore, fabrication techniques such as micromolding have brought increasing attention, due to its considerable mass production and low-cost opportunities in the industry.[61-63] Micromolding has become one of the most often employed methods in the drug delivery area, due to its simplicity, high reproducible structure shape/sharpness, and scalability. Micromolding is a technique where either a molten or a liquid (polymeric, ceramic, or metallic material) is casted/poured into a micromold with negative microneedle-like features. After degassing and under vacuum or centrifugal force, the now filled poured-casted material cavities on the mold are then transformed to the final solid form by air, cooling or UV exposure and further demolded.

Another excellent candidate is 3D printing; 3D printing has been a technology that over the time has introduced a universally tremendous impact in a broad spectrum of areas, from aerospace, automotive to biomedical applications.[64,65] The high versatility and reproducibility of 3D printing, along with its fast and reliable cost-effective fabrication capabilities have encouraged research in the fabrication of transdermal microneedle devices. 3D printing employs either polymer filaments or polymer-based photocurable resin. 3D printing is used as a general term that involves different methods such as: Fused Filament Fabrication (FFF)[66], stereolithography (SLA)[67], and direct light

processing (DLP).[68] However, microstereolithography (μSLA) techniques have been the most promising methods to reproduce microneedles at a low cost and high throughput with reliable geometry, density, sharpness, and dimensions. The manufacturing of 3D models based on a computer aided design (CAD) by μSLA is based on the spatially controlled solidification (curing) of a photocurable polymer in a micron layer-by-layer fashion (10-50μm layers).

Primarily, TDD and sensing devices rely on robust and adequate mechanical properties to breach dermal barriers with ease. The microneedle structure should be sufficiently enough stiff and strong to evenly pierce the human SC of the skin without rupturing or bending during the application. Additionally, the microneedle structure should dissolve rapidly upon insertion, therefore, meeting these properties is a critical and key requirement for an efficient and successful application. The factors that determine whether a microneedle device has a successful insertion are the material composition, dimensions (height, base; aspect ratio), tip sharpness, and geometry. Microneedles with a tip sharpness of less than 50 μm, a base/width of ~500 μm and height less ~1000 μm than have shown to produce less pain upon application; such resolution and dimensions are considerably important to minimize skin damage and mitigate body immune responses.[69] Moreover, additional factors such as the skin elasticity and thickness should be taken fully into account, as they are unrelated to the microneedle materials, geometry, and fabrication method.[70-73]

1.3 Microneedle Kinetics and Materials for Smart/Controlled Delivery

While designing a TDD and platforms, it is usually a requirement to consider the onset and duration of the therapeutic activity of the loaded payload and desired application. Polymeric microneedles are largely suited for wide variety of applications as there is a broad number of material-wise dissolvable options available. and currently being employed in the biomedical field. Smart-dissolvable based microneedles can be classified as follows: rapid acting (<1 h), intermediate acting (1-6h), long acting (24h-1w) and ultra-long acting (>4w).[74] For example, illnesses such as hypertension, and diabetes will demand ultra-long-acting sustained release of their corresponding therapeutics, increasing patient compliance by eliminating the need of multiple daily treatments/injections.[75-77] Chronic pain and acute illnesses would require a combination between rapidly acting and long-acting treatment for weeks.[78,79] On the contrary, vaccine applications, and the treatment of malignancies such as cancer, and bacterial infections should require fast-acting release platforms.[80,81]

Dissolving microneedles employ biocompatible polymers that are mixed along with the therapeutic payload to form the needle geometry/structure. By tunning and adjusting the type of material and polymer concentration/composition within the formulation, the rate of release (release kinetics) can be controlled. Numerous polymeric materials, natural or synthetically driven are commonly used as the matrix due to their low-cost, and mass production capabilities; for example: polyvinylpyrrolidone (PVP), polyvinyl alcohol (PVA), carboxymethylcellulose (CMC), starch, sodium alginate (SA), dextran and various sugars.[82] Furthermore, the use biodegradable polymers such as: chitosan, silk

fibroin, and poly(lactide-co-glycolide) (PLGA) have been explored as materials for designing microneedles with long and ultra-long-acting sustained drug-release properties, as they biodegrade over time rather than dissolve.[83-86] Even though the microneedle structure provides a simple matrix and platform with room and stability to load drugs or vaccines in their free form, an alternative by incorporating micro-nano particle formulations that encapsulate different formulations of the therapeutic payload has been previously reported.[87-90] This is realized to protect sensitive antigens/drugs from possible harsh fabrication processes as further protective layers.

1.4 References

1. S. J. Singer, J. Burgers, M. Friedberg, M. B. Rosenthal, L. Leape, E. Schneider, Med. Care Res. Rev. 2011, 68, 112–127.

2. C. H. Ellenbecker, L. Samia, M. J. Cushman, K. Alster, Patient safety and quality in home health care. Patient safety and quality: An evidence-based handbook for nurses, 2008. Chapter 13. https://www.ncbi.nlm.nih.gov/books/NBK2631/ (accessed: July 14, 2021).

3. D. M. Levine, K. Ouchi, B. Blanchfield, A. Saenz, K. Burke, M. Paz, K. Diamond. C. T. Pu, J. L. Schnipper, Ann. Intern. Med. 2020, 172, 77–85.

4. M. R. Prausnitz, Adv. Drug Deliv. Rev. 2004, 56, 581–587

5. G. D. Eslick, N. J. Talley, Aliment. Pharmacol. Ther. 2008, 27, 971–979.

6. M. Ruth, I. Månsson, N. Sandberg, Scand. J. Gastroenterol. 1991, 26, 73–81.

7. C. Shanley, G. O'Loughlin, J. Gerontol. Nurs. 2000, 26, 35–48.

8. B. Homayun, X. Lin, H. J. Choi, Pharmaceutics 2019, 11, 129.

9. H. Gupta, D. Bhandari, A. Sharma, Recent Pat. Drug Deliv. Formul. 2009, 3, 162–173.

10. S. Ahadian, J. A. Finbloom, M. Mofidfar, S. E. Diltemiz, F. Nasrollahi, E. Davoodi, V. Hosseini, I. Mylonaki, S. Sangabathuni, H. Montazerian, K. Fetah, R. Nasiri, M. R. Dokmeci, M. M. Stevens, T. A. Desai, A. Khademhosseini, Adv. Drug Deliv. Rev. 2020, 157, 37–62.

11. L. Engelke, G. Winter, S. Hook, J. Engert, Vaccine, 2015, 33, 4663–4674.

12. G. M. Glenn, R. T. Kenney, Mass Vaccination: Global Aspects—Progress and Obstacles 2006, 304, 247–268

13. NaSH Summary Report for Blood and Body Fluid Exposure, 2011, https://www.cdc.gov/nhsn/PDFs/NaSH/NaSH-Report-6-2011.pdf (accessed: July 14, 2021).

14. M. A. Miller, E. Pisani, Bull. World Health Organ. 1999, 77, 808.

15. J. G. Hamilton, Fam. Pract. 1995, 41, 169–182.

16. L. S. Cook, J. Infus. Nurs. 2016, 39, 273–279.

17. H. Rosen, T. Abribat, Nat. Rev. Drug Discov. 2005, 4, 381–385.

18. M. R. Prausnitz, R. Langer, Nat. Biotechnol. 2008, 26, 1261-1268.

19. J. Hadgraft, Int. J. Pharm. 1999, 184, 1–6.

20. A. Z. Alkilani, M. T. McCrudden, R. F. Donnelly, Pharmaceutics 2015, 7, 438–470.

21. A. M. Barbero, H. F. Frasch, J. Control. Release 2017, 260, 234–246.

22. G. Ma, C. Wu, J. Control. Release 2017, 251, 11–23.

23. S. H. Bariya, M. C. Gohel, T. A. Mehta, O. P. Sharma, J. Pharm. Pharmacol. 2012, 64, 11–29.

24. R. Nagarkar, M. Singh, H. X. Nguyen, S. Jonnalagadda, J. Drug Deliv. Sci. Technol. 2020, 59, 101923.

25. T. Waghule, G. Singhvi, S. K. Dubey, M. M. Pandey, G. Gupta, M. Singh, K. Dua, Biomed. Pharmacother. 2019, 109, 1249–1258.

26. D. D. Zhu, X. P. Zhang, B. L. Zhang, Y. Y. Hao, X. D. Guo, Adv. Ther. 2020, 3, 2000033.

27. Donnelly, R., & Douroumis, D. Drug Deliv. Transl. Res. 2015, 5, 311–312

28. K. Lee, H. C. Lee, D. S. Lee, H. Jung, Adv. Mater. 2010, 22, 483–486.

29. B. P. Chaudhri, F. Ceyssens, P. De Moor, C. Van Hoof, R. Puers, J. Micromech. Microeng. 2010, 20, 064006.

30. L. Ventrelli, Marsilio L. Strambini, G. Barillaro, Adv. Healthc. Mater. 2015, 4, 2606–2640.

31. J. Xu, R. Danehy, H. Cai, Z. Ao, M. Pu, A. Nusawardhana, D. Rowe-Magnus, F. Guo, ACS Appl. Mater. Interfaces 2019, 11, 14640–14646.

32. M. J. Uddin, N. Scoutaris, S. N. Economidou, C. Giraud, B. Z. Chowdhry, R. F. Donnelly, D. Douroumis, Mater. Sci. Eng. C 2020, 107, 110248.

33. S. Bhatnagar, K. Dave, V. V. K. Venuganti, J. Control. Release 2017, 260, 164–182.

34. X. Jin, D. D. Zhu, B. Z. Chen, M. Ashfaq, X. D. Guo, Adv. Drug Deliv. Rev. 2018, 127, 119–137.

35. X. Li, X. Huang, J. Mo, H. Wang, Q. Huang, C. Yang, T. Zhang, H. J. Chen, T. Hang, F. Liu, L. Jiang, Q. Wu, H. Li, X. Xie, Adv. Sci. 2021, 2100827.

36. S. D. Gittard, B. Chen, H. Xu, A. Ovsianikov, B. N. Chichkov, N. A. Monteiro-Riviere, R. J. Narayan, J. Adhes. Sci. Technol. 2013, 27, 227–243.

37. P. Aggarwal, C. R. Johnston, Sens. Actuators B Chem. 2004, 102, 226–234.

38. N. Wilke, A. Mulcahy, S. R. Ye, A. Morrissey, Microelectronics J. 2005, 36, 650–656.

39. M. A. L. Teo, C. Shearwood, K. C. Ng, J. Lu, S. Moochhala, Biomed. Microdevices 2005, 7, 47–52.

40. S. P. Davis, W. Martanto, M. G. Allen, M. R. Prausnitz, IEEE. Trans. Biomed. Eng. 2005, 52, 909–915.

41. H. Kalluri, C. S. Kolli, A. K. Banga, AAPS J. 2011, 13, 473–481.

42. S. Lee, W. Jeong, D. J. Beebe, Lab Chip 2003, 3, 164–167.

43. P. N. Ayittey, J. S. Walker, J. J. Rice, P. P. De Tombe, Pflug. Arch. Eur. J. Physiol. 2009, 457, 1415–1422.

44. K. Ita, J. Drug Deliv. Sci. Technol. 2018, 44, 314–322.

45. B. Cai, W. Xia, S. Bredenberg, H. Li, H. Engqvist, Eur. J. Pharm. Biopharm. 2015, 94, 404–410.

46. T. Miyano, Y. Tobinaga, T. Kanno, Y. Matsuzaki, H. Takeda, M. Wakui, K. Hanada, Biomed. Microdevices 2005, 7, 185–188.

47. C. J. Martin, C. J. Allender, K. R. Brain, A. Morrissey, J. C. Birchall, J. Control. Release 2012, 158, 93–101.

48. M. Kim, B. Jung, J. H. Park, Biomaterials 33, 668–678.

49. A. Sivaraman, A. K. Banga, Drug Deliv. Transl. Res. 2017, 7, 16–26.

50. S. P. Sullivan, N. Murthy, M. R. Prausnitz, Adv. Mater. 2008, 20, 933–938.

51. W. Yu, G. Jiang, Y. Zhang, D. Liu, B. Xu, J. Zhou, Mater. Sci. Eng. C 2017, 80, 187–196.

52. A. K. Banga, Expert Opin. Drug Deliv. 2009, 6, 343–354.

53. J. Li, B. Liu, Y. Zhou, Z. Chen, L. Jiang, W. Yuan, L. Liang, PLoS One 2017, 12, e0172043.

54. S. P. Davis, M. R. Prausnitz, M. G. Allen, 12th Int. Conf. Solid-State Sens. Actuators Microsyst. 2003, 2, 1435–1438.

55. K. Ita, Biomed. Pharmacother. 2017, 93, 1116–1127.

56. H. J. G. E. Gardeniers, R. Luttge, E. J. W. Berenschot, M. J. de Boer, S. Y. Yeshurun, M. Hefetz, R. van-t Oever, A. van den Berg, J. Microelectromech. Syst. 2003, 12, 855.

57. R. F. Donnelly, T. R. Raj Singh, D. I. Morrow, A. D. Woolfson, Wiley, 2012, Ch.2, 20–56.

58. H. Kathuria, J. S. Kochhar, M. H. M. Fong, M. Hashimoto, C. Iliescu, H. Yu, L. Kang, J. Vis. Exp. 2015, 105, 52914.

59. A. Rodriguez, D. Molinero, E. Valera, T. Trifonov, L. F. Marsal, J. Pallarès, R. Alcubilla, Sens. Actuators, B, 2005, 109, 135.

60. B. Ma, S. Liu, Z. Gan, G. Liu, X. Cai, H. Zhang, Z. Yang, Microfluid. Nanofluid. 2006, 2, 417.

61. E. Larrañeta, R. E. M. Lutton, A. D. Woolfson, R. F. Donnelly, Mater. Sci. Eng., R 2016, 104, 1.

62. S. D. Gittard, A. Ovsianikov, N. A. Monteiro-Riviere, J. Lusk, P. Morel, P. Minghetti, C. Lenardi, B. N. Chichkov, R. J. Narayan, J. Diabetes Sci. Technol. 2009, 3, 304.

63. S. Bystrova, R. Luttge, M. Eng. 2011, 88, 1681.

64. C. Balletti, M. Ballarin, F. Guerra, J. Cult. Herit. 2017, 26, 172–182.

65. J. Wang, Y. Zhang, N. H. Aghda, A. R. Pillai, R. Thakkar, A. Nokhodchi, M. Maniruzzaman, Adv. Drug Deliv. Rev. 2021, 174, 294–316.

66. S. Wickramasinghe, T. Do, P. Tran, Polymers 2020, 2, 1529.

67. J. Huang, Q. Qin, J. Wang, Processes 2020, 8, 1138.

68. D. K. Patel, A. H. Sakhaei, M. Layani, B. Zhang, Q. Ge, S. Magdassi, Adv. Mater. 2017, 29, 1606000.

69. H. S. Gill, D. D. Denson, B. A. Burris, M. R. Prausnitz, Clin. J. Pain 2008, 24, 585.

70. M. Kirkby, A. R. Hutton, R. F. Donnelly, Pharm. Res. 2020, 37, 1–18.

71. P. Aggarwal, C. R. Johnston, Sens. Actuators B Chem. 2004,102, 226–234.

72. M. N. Abser, M. Gaffar, M. S. Islam, ICECE 2010, 222–225.

73. B. Ahn, Int. J. Control Autom. Syst. 2020, 18, 143–149.

74. S. Pahal, K. Badnikar, V. Ghate, U. Bhutani, M. M. Nayak, D. N. Subramanyam, P. K. Vemula, Eur. J. Pharm. Biopharm. 2021, 159, 151–169.

75. R. B. Shah, M. Patel, D. M. Maahs, V. N. Shah, Int. J. Pharm. Investig. 2016, 6, 1.

76. L. C. Ng, M. Gupta, Asian J. Pharm. Sci. 2020, 15, 13–25.

77. L. M. Prisant, B. Bottini, J. T. DiPiro, A. A. Carr, Am. J. Med. 1992, 93, S45–S55.

78. J. R. Hsu, H. Mir, M. K. Wally, R. B. Seymour, J. Orthop. Trauma 2019, 33, e158.

79. T. Schreiner, U. F. Schaefer, H. Loth, J. Pharm. Sci. 2005, 94, 120–133.

80. A. D. Permana, A. J. Paredes, F. Volpe-Zanutto, Q. K. Anjani, E. Utomo, R. F Donnelly, Eur. J. Pharm. Biopharm. 2020, 154, 50–61.

81. S. P. Sullivan, D. G. Koutsonanos, M. del Pilar Martin, J. W. Lee, V. Zarnitsyn, S. O. Choi, M. Niren, W. C. Richard, S. Ioanna, M. R. Prausnitz, Nat. Med. 2010, 16, 915–920.

82. Y. C. Kim, J. H. Park, M. R. Prausnitz, Adv. Drug Deliv. Rev. 2012, 64, 1547–1568.

83. K. Lee, C. Y. Lee, H. Jung, Biomaterials 2011, 32, 3134–3140.

84. D. I. D. Cho, H. J. Yoo, J. Microelectromechanical Syst. 2014, 24, 10–18.

85. W. Li, R. N. Terry, J. Tang, M. R. Feng, S. P. Schwendeman, M. R. Prausnitz, Nat. Biomed. Eng. 2019, 3, 220–229.

86. M. C. Chen, M. H. Ling, K. Y. Lai, E. Pramudityo, Biomacromolecules 2012, 13, 4022–4031.

87. P. C. DeMuth, W. F. Garcia-Beltran, M. L. Ai-Ling, P. T. Hammond, D. J. Irvine, Adv. Funct. Mater. 2013, 23, 161–172.

88. J. M. Mazzara, L. J. Ochyl, J. K. Hong, J. J. Moon, M. R. Prausnitz, S. P. Schwendeman, Bioeng. Transl. Med. 2019, 4, 116–128.

89. M. Battisti, R. Vecchione, C. Casale, F. A. Pennacchio, V. Lettera, R. Jamaledin, M. Profeta, C. Di Natale, G. Imparato, F. Urciuolo, P. A. Netti, Front. Bioeng. Biotechnol. 2019, 7, 296.

90. M. Zaric, O. Lyubomska, C. Poux, M. L. Hanna, M. T. McCrudden, B. Malissen, R. J. Ingram, U. F. Power, C. J. Scott, R. F. Donnelly, A. Kissenpfennig, J. Invest. Dermatol. 2015, 135, 425–434.

Chapter 2. Use of Microneedles as Active Delivery Platforms

2.1 Active Microneedles: Towards Enhanced Drug Delivery

2.1.1 Introduction

Current efforts and recent innovations on drug delivery platforms have the potential to enhance therapeutic efficacy. Although existing therapy modalities (e.g., oral delivery, needles) have addressed a variety of therapeutic delivery requirements, there are urgent needs to develop efficient local delivery platforms that can overcome the pain and fear from hypodermic injections,[1-3] and address the limited absorption associated with systemic pill-based delivery,[4,5] while maintaining cost-efficacy, convenience, and comfort. One promising route relies on the use of microneedles towards painless and localized delivery of drugs across the skin.[6-8] For example, microneedles have been approved by the FDA in clinical setting[9] for delivery of vaccines and pharmaceutical through the epidermis.[10-12] Furthermore, this route offers autonomy and ease of use, as the therapeutic payload is released autonomously over prolonged periods, based on the material properties or by the inclusion of encapsulated smart drug-loaded particles.[13,14] Nevertheless, microneedles commonly rely on passive diffusion, which limits the penetration depth and distribution of the therapeutic payloads. To address this challenge, different external stimuli have been employed to enhance the drug permeation through the epidermis. These external triggers include electroporation,[15,16] ultrasound,[17,18] light,[19-21] and temperature.[22,23] However, the requirement of external (often costly and bulky) equipment limits the widespread use of such triggered delivery to specialized centralized lab settings and restricts their use in field settings and remote locations. Future efforts are

thus required to combine the advantages of both autonomous and active delivery into a single microneedle delivery platform, while reducing the time and costs necessary for achieving high therapeutic efficiency.

Here, we present an engineered a degradable active microneedle delivery platform, capable of generating autonomously vigorous convective fluid flows, for a greatly enhanced payload permeation. Our patch delivery system consists of a degradable polymeric microneedle array loaded with the therapeutic payload along with active motor- Magnesium (Mg) microparticles. Upon skin insertion, the microneedle polymeric matrix starts to dissolve, exposing the embedded Mg particles to react instantaneously with the surrounding interstitial biofluid, resulting in a rapid generation of hydrogen bubbles.[24] Such microbubble formation induces distinct vortex flow fields that lead to a powerful and autonomous 'pumping-like' action and locally applied force, that results in a dynamic and extremely efficient transport of and permeation of the embedded therapeutic payload.[25,26] The drug release kinetics of our active microneedle model was tested *in vitro* by measuring the amount of therapeutic payload that passed through tissue-mimicking phantom gel and pigskin barriers, demonstrating a greatly enhanced permeation and distribution when compared to common passive microneedles. The versatility of our approach is also demonstrated by integrating spatially resolved active and passive microneedle zones in the same patch, towards combinatorial (fast and sustained) release delivery. Overall, the active microneedles delivery presented here offers an autonomous, biocompatible, and highly efficient alternative for faster release kinetics of payloads through the skin, hence obviating the need of external activation (and

related triggering equipment), potentially reducing the time necessary to achieve high therapeutic efficiency.

2.1.2 Experimental Methods

PDMS microneedle mold fabrication

The master microneedle mold was placed in a clean Petri Dish, Crystal Clear Borosillicate Glass with a double-sided tape to attach the mold properly. A mix ratio of 10:2 base/curing agent PDMS (SYLGARD® 184, Sigma Aldrich) solution was later casted onto the microneedle patch and placed in vacuum within a desiccator for 5 min at 23 in of Hg. Bubbles were removed from the surface and PDMS was cured in an oven at 75C for 30 min. Later sample was removed from the oven and cured PDMS was separated from petri dish gently to obtain the negative mold. PDMS mold was adjusted to desired size with the use of a blade cut. The microneedle molds were washed with hand soap and rinsed with water twice, with further ultrasonication bath for 15 min. Later, the mold was dried with air gun and cleaned by adding 0.25 mL of 2-propanol to each mold for 10 min. Molds were placed in the oven (75C for 15 min) and not used until they reached room temperature.

Microneedle patch fabrication

A volume of 0.25 mL of a 10% w/v polymer (Polyvinylpyrrolidone (PVP) average Mw~360,000, Sigma Aldrich) aqueous solution of pH 10.5 was added onto the PDMS microneedles mold and further placed in a closed desiccator in vacuum for 5-10 min (23 in Hg). Molds were removed from desiccator with the further removal of bubbles

generated at interface between microneedles pores and solution with the use of plastic 1mL disposable transfer pipettes or the use of a tweezer. Later, bubbles in the surface of the solution were removed, or popped with the use of a pipette or needle tip. Furthermore, a second addition of 0.25 mL of polymer was carried out, turning on vacuum again. This process was performed until polymer solution was 1 mL. The payload solution: 50 μg of IgG-HRP(HRP-Goat anti-human IgG Antibody peroxidase from Vector Laboratories), 50 μg of IgG-AlexaFluor555 (Abcam), 20 μg of Rh6G (Sigma Aldrich), 20 μg of FITC(Sigma Aldrich), was added to the mold and let it to dry for 24-72 hours. Once microneedle patches were ready, a 1 cm^2 scotch tape was applied on top of the needles and peeled off from the PDMS mold. Microneedle patches were stored at room temperature prior to use. Active microneedles were fabricated by employing the same procedure but before casting the polymer onto the mold, 50μL of a 5mg/mL stock Mg microparticle (catalog #FMW40, from TangShanWeiHao Magnesium Powder Co., Ltd China) in isopropanol suspension was casted and infiltrated within the negative microneedles features of the PDMS mold. A PVP solution of pH 10.5 was used to prevent Mg particles to react, ensuring a proper microneedle patch fabrication.

Phantom skin mimicking gel fabrication

2% Agarose (Sigma Aldrich) was weighted in a 20mL Crystal Clear Borosillicate vial in DI water. Solution was heated a 175 C until solution turned transparent. Later, the temperature was lowered to 120C and casted onto 1.5mm, 3.0mm or 4.5mm Eco-Flex

negative molds. Solution was let it dry for 2 min and further removed form mold with help of tweezers. Phantom skin mimicking gel were soaked in PBS pH 7.4 prior use.

Microneedle characterization

Bright field, fluorescent and merged images of the microneedles were obtained with an EVOS FL microscope coupled with 4× and 20× objectives with a fluorescence filter for a green and red-light excitation. The scanning electron microscopy (SEM) images were captured with the use of a FEI Quanta 250 ESEM instrument (Hillsboro, Oregon, USA), using an acceleration voltage of 2-5 kV. The array was previously sputtered with an Iridium coating. The Energy-Dispersive X-Ray Spectroscopy (EDX) mapping analysis was carried out with an Oxford EDS detector attached to an SEM instrument and controlled by a Pathfinder software. Mg particles from microneedles were tested in the presence of tracer particles (0.9μm Nile red fluorescent particles from Sphero Tech) to study the mean square displacement of the activity of the Mg microparticles at different pH. Stack of images were analyzed by Image J Software, Flow trace plug in (1s particle trajectory image stacking).

Mechanical testing

A mechanical test was performed to all microneedles by applying a constant load to a single tip. The mechanical strength of microneedles was measured by visualizing the displacement of the plate when intimate contact with the microneedle tip structure compared to the relative height of the cone. The fracture point was determined when a

dramatic drop in force was experienced. The applied force was done with the use of a Force Gauge Model M4-20 system Mark0-10 Series 4.

In vitro release kinetics

Microneedles were subjected to a test of piercing and further dissolved into a 3mm thickness 2% Phantom Tissue Skin with a PBS pH 7.4 reservoir below. Both passive and active microneedles (n=5) were loaded with 50 μg of Rhodamine 6G or IgG-HRP. After piercing for different set times, the supernatant was collected and analyzed by using a UV-2450 Shimadzu spectrophotometer from 300 to 700nm. For the electrochemical measurement of IgG-HRP, a reservoir with TMB+H_2O_2 was placed below the phantom tissue and repetitive runs of amperometry at a fixed potential of +0.1V for 50 s were employed to analyze the current change behavior of both microneedle controls.

Skin penetration and diffusion studies

A 1.5mm thickness porcine skin area of 2x2cm was pierced by microneedles for both diffusion and active control studies. The microneedle patches were placed for different interval times, 5, 10, and 20 min and further cross sectioned for analysis at room temperature.

Stereolithography 3D printed microneedle devices

The prototyping of solid microneedles is currently supported by paid or free commercial software (SolidWorks, Fusion360). The 3D microneedle STL models were transferred to a slicing software (AnyCubic Photon slicer64), which sliced the 3d model

into thousands of micron layers in a 30M file, later connected to the printer via USB. The file was uploaded to an AnyCubic Photon UV LCD 3D printer for the prototyping and printing. Microneedles were fabricated within a 115 x 65mm build plate, by using exposure times of 8s and step size of 20um. This instrument projected a 25W UV light source that sits inside a stainless-steel snoot, through a photocurable material (AnyCubic colored resin). The 3D printer has a 2K LCD masking screen, masking LCD provides very fine printing details down to few micrometers. After the fabrication, the build plate containing microneedle devices was gently removed from the printer, and microneedle devices were detached. Supports printed to build the microneedle devices were removed, microneedles were rinsed in IPA and placed under an ultrasonic bath for the removal excess of uncured material. Microneedle devices were subsequently placed in a UV nail machine to post cure for 30 min.

2.1.3 Experimental Results

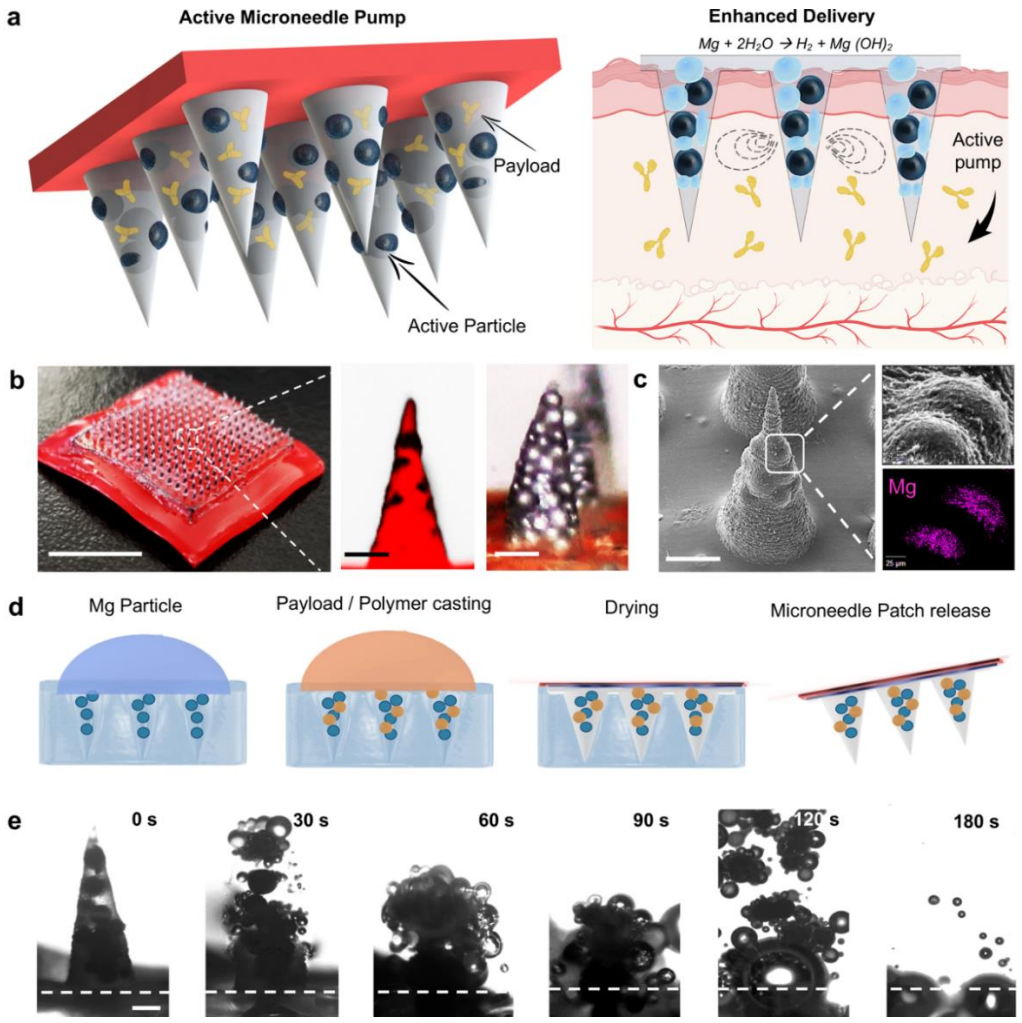

Figure 2.1.1 Active microneedle for enhanced drug delivery. a) Active microneedle patch composition, and built-in Mg particle activation as pumps when in contact with bodily fluids, leading to an enhanced drug release. b) Digital photograph showing a patch of 15x15 microneedle array and optical/fluorescent microscopy images of an active microneedle tip loaded with Mg particles, scale bars, 6 mm and 200µm respectively. c) Scanning electron micrograph of single active microneedle tip and EDX analysis for Mg. Scale bar, 300µm, respectively. d) Fabrication steps of the microneedle patch: PDMS micromolding over master microneedle, PDMS negative microneedle mold released, Mg particle loading, polymer and payload inclusion, polymer drying, adhesive application and peel off. e) Microscopy time-frame images taken from a single active microneedle tip clearly showing polymer dissolution in PBS pH 6.0 and particle activation (30 sec intervals), scale bar, 200µm.

Figure 2.1.1a illustrates a schematic illustration of the active payload delivery microneedle patch. The active microneedle structure contains both the therapeutic payload and spherical Mg microparticles (50-100μm) within a Polyvinylpyrrolidone (PVP) polymer matrix (Figure 2.1.1a left part); once the microneedle patch pierces the skin, the polymer microneedle tip starts to dissolve, exposing the Mg particle surface to the surrounding biological fluid. PVP was chosen as the polymer due to its hydrophilic, and biocompatible properties,[27] being used in a wide variety of biomedical applications, presenting low cytotoxicity and biodegradability.[28] The Mg particles thus start to react with the interstitial fluid, resulting in their dissolution and rapid production of H_2 bubbles. The generated bubbles induce distinct vortex flow fields at the localized application site, which results in greatly enhanced permeation and active transport of the loaded payload Figure 2.1.1a right part. Figure 2.1.1b shows a 15x15 microneedle array, illustrating the efficient loading of multiple microneedles (400μm diameter base and 850μm height) that preserve a robust hard structure and a sharp stiff tip (less than 5μm). The ability to load both active microparticles and therapeutic payload in a single needle is illustrated by the fluorescence and digital microscopy photographs shown in Figure 2.1.1b (zoom in), where the microneedles are loaded with Rh6G (red color) and Mg particles (black dots). A scanning electron micrograph image of a single active microneedle tip loaded with Mg particles is illustrated in Figure 2.1.1c, as well as an Energy Dispersive X-Ray (EDX) analysis of the entrapped Mg particles, clearly showing the embedded microparticles within the needle, protected by the polymeric matrix. The

magnification of a single microneedle shows the close packing of the magnesium particles within the microneedle structure.

Active microneedles were fabricated by a micromolding technique (Figure 2.1.1d), [29,30] briefly, the Mg microparticles were first infiltrated into the microneedle negative PDMS mold, following by the addition of the therapeutic payload and the PVP polymer matrix (pH 10.5); the latter was allowed to dry overnight. The final patch was transferred to an adhesive base and stored at room temperature (25°C). The active microneedle reacts quickly after getting in contact with fluids, as shown by the time-lapse microscopy images shown in Figure 2.1.1e (at 30-sec intervals).

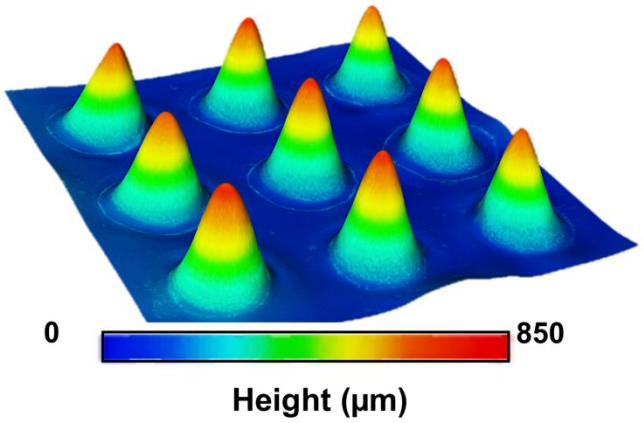

Figure 2.1.2 3D height microscopy profile image of a 3x3 microneedle array.

These images illustrate the rapid dissolution and vigorous hydrogen generation of a single active microneedle tip, which leads to an explosive-like behavior and a fast dissolution within less than 60 sec. The consistency in the dimensions of the individual

tips of the microneedle array is further supported by the microneedle height profile, shown in Figure 2.1.2

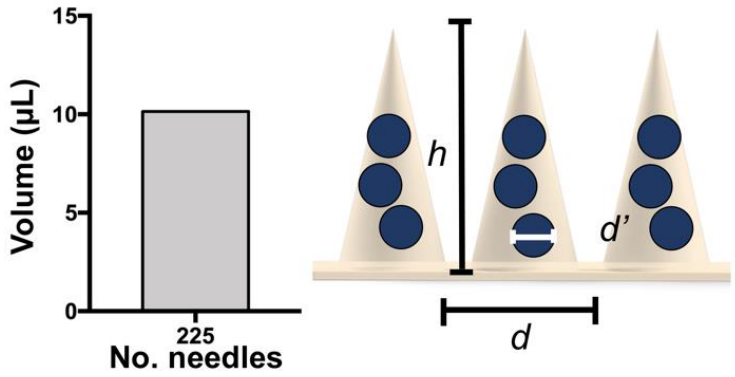

Figure 2.1.3 Theoretical loading of a characteristic microneedle patch containing 225 conical microneedle tips

The active microneedle can load diverse cargo combinations. The loading capacity of the patch was calculated based on 66% of the volume of conical structures that can be loaded with spherical particles.[31] We estimate that our microneedle array, comprising a total of 225 microneedle tips, can load a total volume of ~10.13 µL in their tips, and include additional cargo in the microneedle array base, thus providing tunable loading of different doses (Figure 2.1.3).

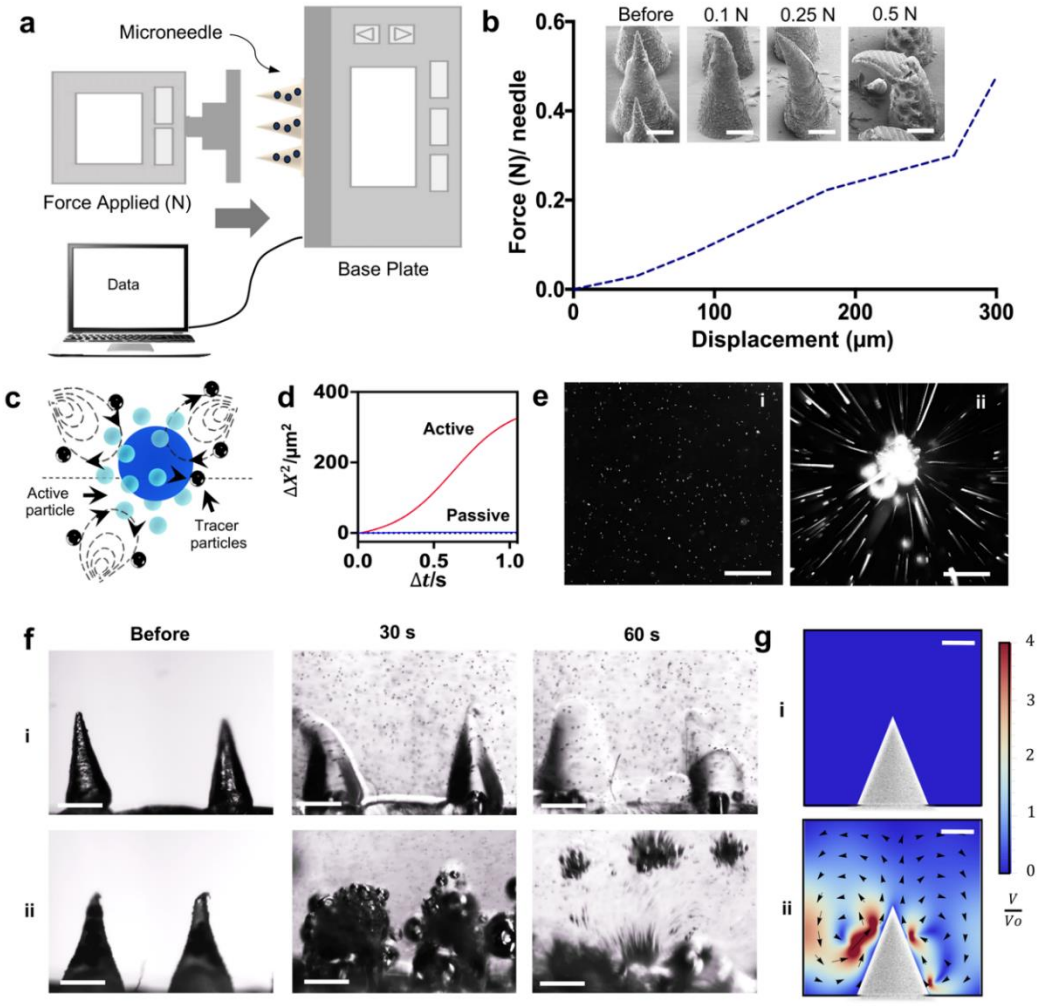

Figure 2.1.4 Mechanical testing of the microneedle patch and active fluid transport (localized streaming) based on Mg particles embedded in dissolvable microneedles. a) Schematic illustration of the mechanical setup used. b) Mechanical analysis of a single microneedle tip under different loads and SEM images of microneedle tips before and after application of each load. Scale bar, 200 μm. c) Schematic of the fluid transport of active Mg particles in the presence of tracer particles. d) Mean Square Displacement of tracer particles using Brownian motion as control or in the presence of the active Mg particles at pH 6.0. Scale bar, 100 μm. e) Flow trace images of the trajectory (over 1s) of 0.9 μm polystyrene tracer particles at pH 6.0 without (*i*) the presence of active particles (Brownian motion), and with active particles (*ii*) at pH 6.0. Scale bar, 100 μm. f) Time-lapse images of two microneedle tips without active particles, showing the dissolution in PBS pH 6.0 of the transient polymer by diffusion (i) and with the Mg particles accelerating the dissolution of the transient polymer due to their fast activation (ii). Scale bar, 400 μm. g) COMSOL Multiphysics simulation of the flow generated by the absence (a) and presence (b) of Mg particles within the microneedle structure.

Measurement of the mechanical strength of the active microneedle under tensile compression (using the set-up of Figure 2.1.4a) displayed a fracture point of 500 mN per needle, corroborating its potential ability to pierce skin and scalability for *in vivo* applications (Figure 2.1.4b). Previous reports indicate that the minimum force required to pierce skin efficiently is 45 mN. A safety factor calculation was determined as a result of the ratio of the failure force to the stablished minimum force for microneedle insertion. Our active microneedles have a safety factor number of 11, considerably higher than the minimum safety factor number of 2, which is considered adequate.[32] Microneedle tips were also visualized by SEM before and after the application of different loads (0.1, 0.25 and 0.5 N), where Mg particles can be seen inside the microneedle structure after fracturing.

The reaction of the embedded Mg microparticles substantially increases the displacement of tracer microparticles through efficient localized fluid convection and mixing resulting from their hydrogen microbubbles production (Figure 2.1.4c). We measured the Mean Square Displacement (MSD) of fluorescent bead tracers (0.9 μm) by following their trajectories under the flow field generated by the Mg active particles and under Brownian motion (Figure 2.1.4d). The active particles present significantly higher mixing and hence greatly enhance the mass transport when compared to their static counterparts. Figure 2.1.4e, overlaps a stack of fluorescent microscopy images, visualizing the negligible flow generated in the absence of Mg particles (Brownian motion) as a control Figure 2.1.4e(i), and the flow lines generated with Mg particles Figure 2.1.4e(ii) (*active*).

The combined effect of faster microneedle dissolution and fluid mixing is shown in the time-lapse images of two microneedle tips without and with Mg particles (Figure 2.1.4f). It is clearly depicted that the vigorous localized mixing due to the embedded particles greatly accelerates the dissolution of the polymer due to their fast activation, but more notorious is the accelerated collision of the tracer particles in solution compared to passive microneedles. In addition, active microneedles were loaded with Rh6G, the resulting accelerated dissolution and Mg particle activity are shown in Figure 2.1.1.

The accelerated and enhanced localized particle induced mixing was corroborated by a COMSOL Multiphysics simulation of the flow generated without and with particles, Figure 2.1.4g (i and ii), respectively, for the early stages of microneedle dissolution and activation. Upon reaction of Mg particles with the solution, gas bubbles nucleate and move upward due to buoyancy force. To obtain a simple picture and capture the essential physics of the problem, we approximated the effect of bubble motion by point forces $\boldsymbol{F}_i$ at the location of the *i*th bubble. (Equation 2.1 and 2.2) While a rough approximation, the results provide a qualitative picture, consistent with experimental observations. The fluid field $\boldsymbol{u}$ obeys the Stokes equation where the summation is over the bubbles present in the fluid.

$$-\nabla \mathrm{p} + \nabla^2 u = \sum_i F_i \qquad \text{Equation 2.1}$$

$$\nabla \cdot u = 0 \qquad \text{Equation 2.2}$$

As shown in Figure 2.1.4g (b) the effect of bubble motions, modeled by point-forces, leads to pumping effect in the fluid. Due to the confined geometry, the fluid follows a

circular pattern, and results in enhanced mixing. A similar pattern is observed in the experimental set up with tracer particles. Upon the motion of the bubbles, the tracer particles near the substrate move toward the active Mg particle while near the top of the liquid surface, the particles move away from the center.

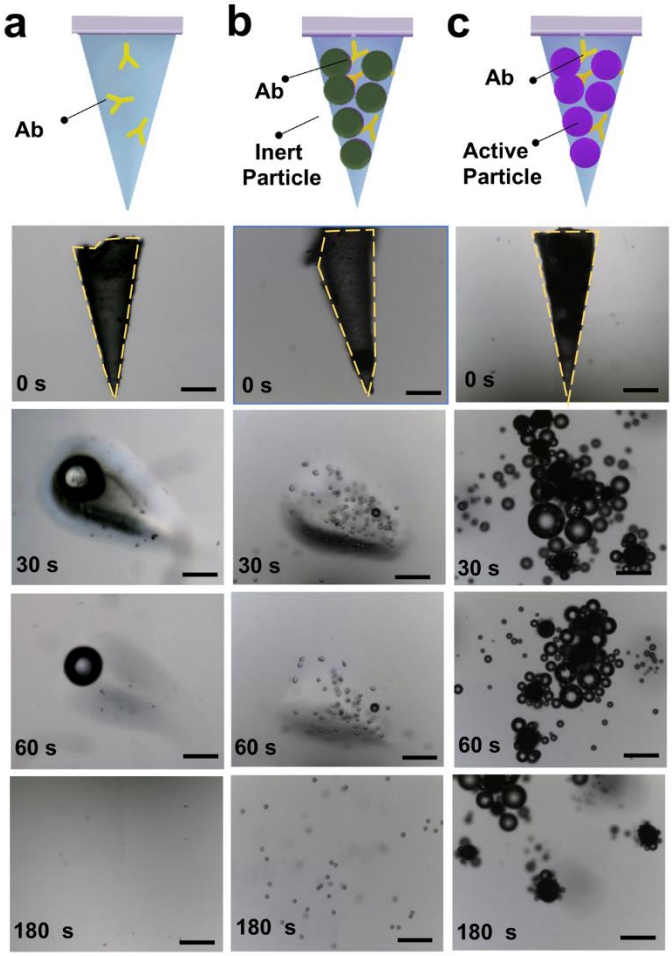

Figure 2.1.5 Schematic and time lapse images of the dissolution rate and fluid mixing of PVP microneedle under different experimental conditions: a) PVP Microneedle b) PS inert particle PVP loaded microneedle and c) Mg PVP loaded active microneedle in PBS buffer pH 6. Scale bar, 200 µm

We studied the dissolution of microneedles containing different cargoes, including active particles, inert particles, and polymer only. (Figure 2.1.5) The microneedle

dissolution rate changes significantly upon incorporating the active particles due to the H_2 bubble generation when compared to static particles and bare polymer microneedles.

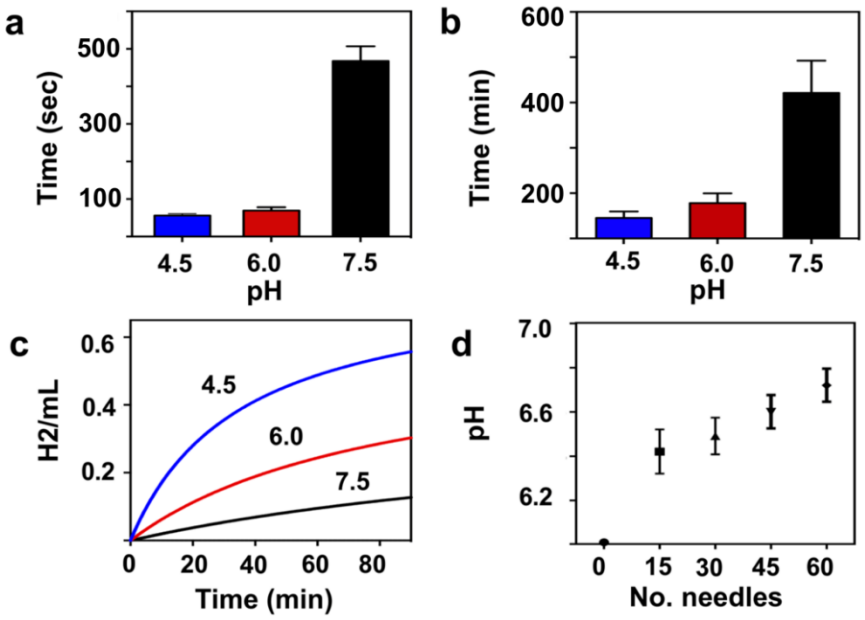

Figure 2.1.6 Active particle microneedle performance, activation, and lifetime. a) Time necessary for Mg particles to start reacting *n=5).* b) Degradation time of Mg particles (*n=5).* c) H_2 generation rate in the presence of different pH environments. d) pH solution variation of active needles after its complete dissolution (15 min).

The Mg reaction is primarily influenced by the pH of the biofluid solution and capable of increasing the local pH after the microneedle dissolution; therefore, the hydrogen generation is directly related to the dissolution of Mg (Figure 2.1.6). Low pH solutions (4 and 6) induced faster activation time and shorter life-time of single Mg particles, compared to neutral pH, which leads to slower activation of the particles and a longer lifetime.

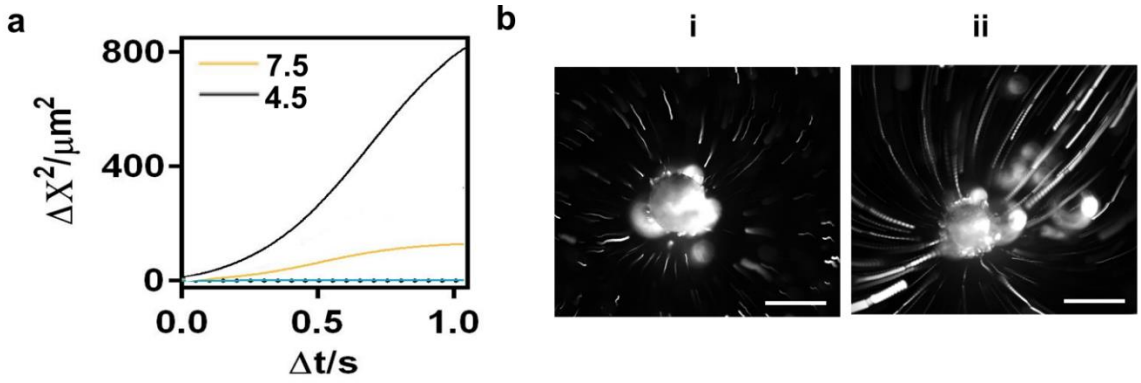

Figure 2.1.7 a) Mean Square Displacement of tracer particles in the presence of Mg particles at pH 4.5, and 7.5. b) Time-lapse images of the flow trace of 0.9 μm fluorescent beads used as tracer particles. i) pH 4.5, and ii) 7.5. Scale bar 100 μm.

The pH of the biofluid has a direct effect on the mixing capabilities, with higher pH presenting faster hydrogen generation thus better mixing (Figure 2.1.7). The pH range was selected on the basis of simulating transdermal pH. Commonly, normal tissue has an intracellular (pH_i) from ~6.7-7.2 and extracellular (pH_e) of ~7.3-7.4; as a universal characteristic of tumor microenvironment, solid tumors have demonstrated to have higher pH_i (7.1-7.6) and lower pH_e (6.2-6.9).[33]

The hydrogen generation can be finally tuned by the addition of an enteric coating on the surface of the particles to delay their activation. As this methacrylate-based polymer (Eudragit S100) starts dissolving at a pH above 7.0 and covers more than half of the structure of the Mg microparticles, the delay over the reaction of Mg in PBS pH 6.0 is directly reflected in the degradation time. This experiment is represented in Figure 2.1.8.

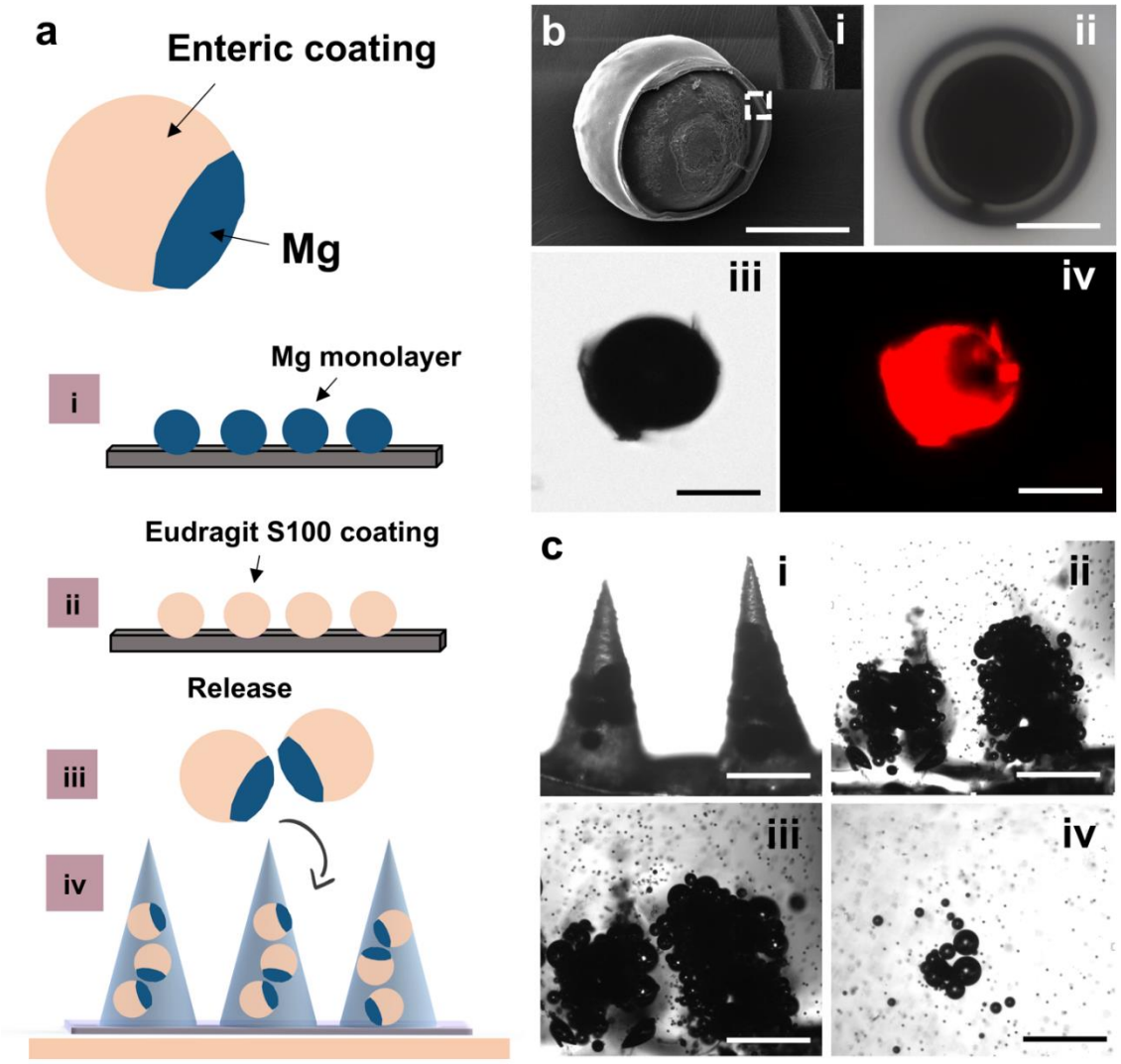

Figure 2.1.8 Tuning the capabilities of Mg particles to control a delayed activation. a) Enteric coating of an Eudragit S100 polymer (solubility >pH 7.0) made over mg particles. Mg monolayer (i), Eudragit s100 coating (ii), release (iii), and loading into microneedles (iv). b) Scanning Electron Micrograph (i) optical microscopy image (ii and iii) and fluorescent image (iv) of Rh6G@Eudragit S100 coated mg particles. Scale bar, 50 µm. c) Time-lapse images of two microneedle tips loaded with enteric coated Mg particles accelerating the dissolution of the transient polymer but with less reactivity compared to uncoated ones (i) before, (ii) 30 sec, (iii) 60 sec and (iv) at 180 sec. Coating provides directionality to the microparticles, thus reducing reactivity but extending degradation time (d). Scale bars, 400 µm.

The inclusion of smaller Mg particles (< 15 µm) within the microneedle structure was explored in Figure 2.1.9. The reactivity of Mg within the microneedle structure ended up being slower (as there is less Mg present) and the degradation time much faster once immersed in PBS pH 6.0. Even though the optimal size of Mg microparticles remains within 30-100µm, such tunable actuation could result in tailored therapies and therapeutic modalities.

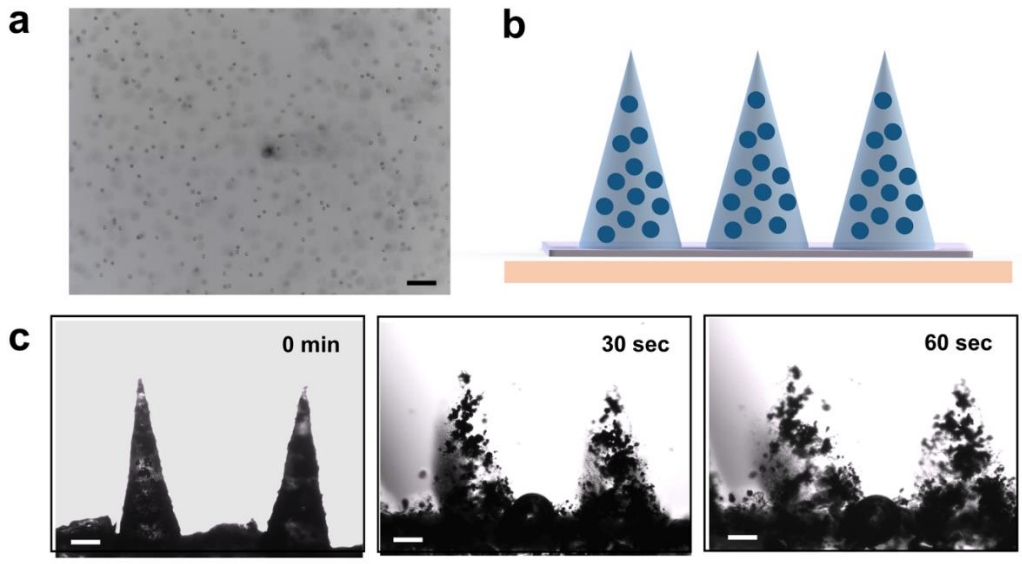

Figure 2.1.9 Microneedles loaded with 20 µm Mg particles. a) Flow trace of Mg particle with tracer 20 µm PS particles. Scale bar, 200 µm. b) Schematic of microneedles loaded with 20 µm Mg particles. c) Time-lapse images of two microneedle tips loaded with 20 µm Mg at different time intervals: (a) 0 min, (b) 30 sec, (c) 60 sec. Scale bars, 200 µm.

This section evaluates the *in vitro* payload release and the potential use of active-particle microneedle towards enhanced and accelerated permeation. The active microneedle release kinetics were evaluated by employing 3 different techniques: electrochemical, spectrophotometric, and fluorescence. Briefly, for the electrochemical

measurements of the payload, the active microneedles were loaded with 50 µg of a tagged IgG-HRP; the IgG Ab was used as a model payload model while its HRP tag facilitates the electrochemical detection that compared the release kinetics of diverse approaches. A schematic illustration of the electrochemical set up used for detecting the released payload is represented in Figure 2.1.10a, consisting on a phantom mimicking tissue (1.5mm of thickness), a reservoir of PBS buffered solution pH 6, and a screen-printed carbon electrode. For the electrochemical detection of the Ab, an amperometric *i-t* curve technique was performed for this measurement as repetitive runs for a fixed period. The microneedle patch was placed over the 1.5mm in thickness phantom mimicking tissue and further pierced; below the phantom tissue, a reservoir of 3,3′,5,5′-Tetramethylbenzidine (TMB) + H_2O_2 solution was placed for the detection of current changes over electrode (HRP coupled to the Ab). The release of Ab from active or passive diffusion microneedles that went through phantom tissue can be seen in Figure 2.1.10b. The results in Figure 2.1.10c clearly depict an average 15-time fold advantage at the 15 min mark where passive diffusion presents a release percentage of 3.8±1.8%, while the active delivery results in 58.5±15.1% release.

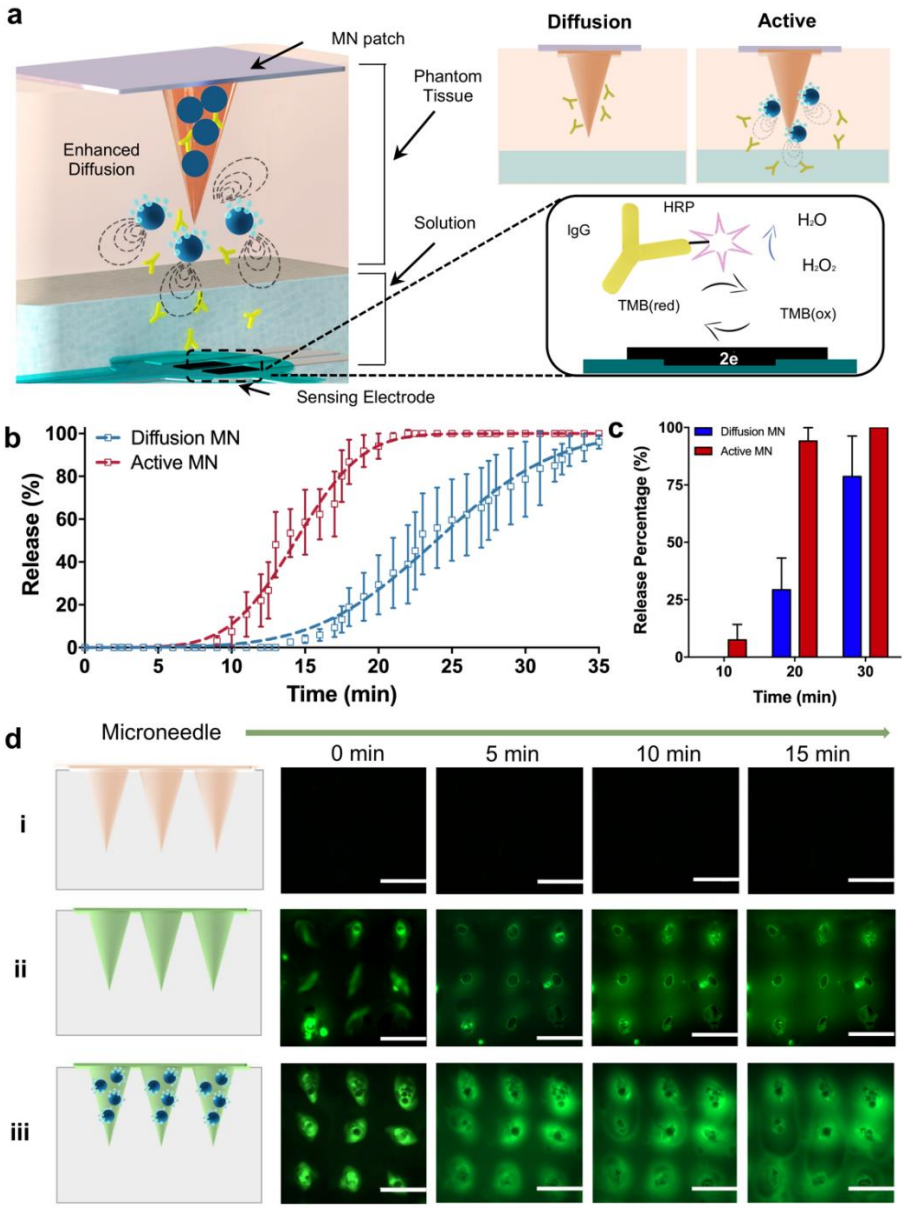

Figure 2.1.10 Evaluation of the *in vitro* payload release performance of common passive and active microneedles by fluorescence, electrochemical and spectrophotometric techniques. a) Schematic illustrating the electrochemical set up of the Ab-based amperometric detection. b) Release kinetics of corresponding Ab delivery of both passive and active microneedles at pH 6.0. Passive microneedles (PVP and IgG-HRP) and active microneedles (PVP, IgG-HRP and Mg particles); *n=5*. c) Corresponding release percentage of Ab at different time points; *n=5*. d) Time-lapse fluorescent images (top view) of microneedles placed on top of a 1.5 mm phantom tissue, obtained at different time points (0-15 min). Blank unloaded microneedles (i), FITC-loaded microneedles (ii), and FITC-loaded active microneedles (iii). Scale bar, 1 mm.

Similarly, the active microneedles resulted in a 3-fold increased delivery at 20 min, with 29.3±13.8% bare vs. 94.1±5.8% active. Active microneedles were loaded with IgG Alexa Fluor-555 in order to corroborate the enhanced payload distribution and permeation into phantom-mimicking tissue when compared to those of passive (diffusion-based) microneedle. Similar to the electrochemical measurements, the setup consisted of a phantom-mimicking tissue of a 1.5 mm thickness and pierced with a microneedle array.

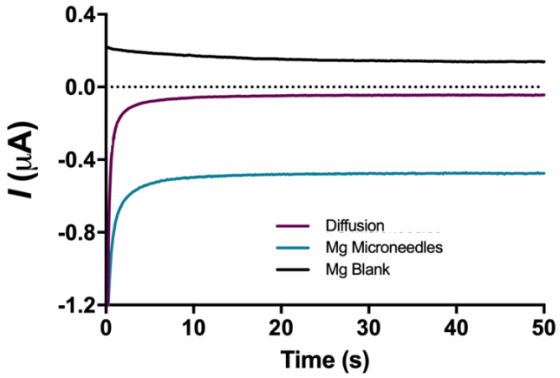

Figure 2.1.11 Amperometric curves of IgG-HRP from 3 release kinetics microneedle controls at the mark of 30 min (antibody that passed through the phantom tissue).

In addition, the lateral diffusion of a FITC (Fluorescein isothiocyanate) loaded microneedle was evaluated by measuring the permeation of the fluorescent molecule through the transparent 1.5 mm thick phantom tissue (visualized via top view fluorescence, Figure 2.1.10d). It should be noted that there was no significant background fluorescence signal from polymer microneedles without FITC in the control in Figure 2.1.10d(i).

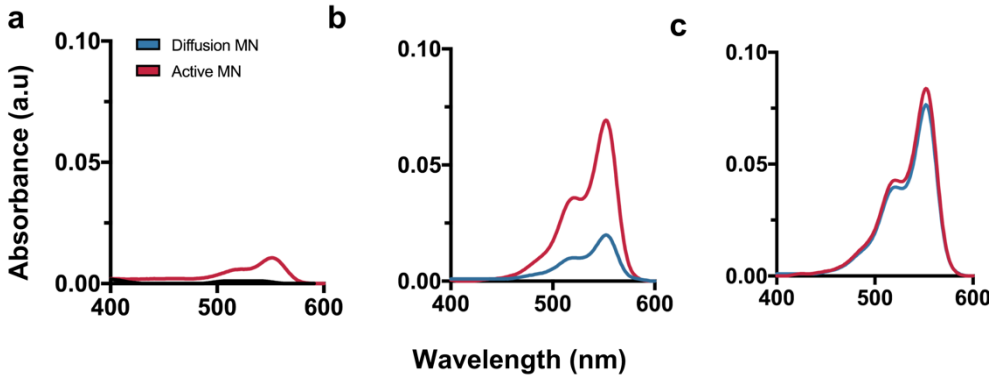

Figure 2.1.12 UV-vis spectrum of released Ab (Igg-AlexaFluor-555) from diffusion and active microneedles at different time points, a) 10 min, b) 20 min, and c) 30 min. Ab content was measured from PBS buffer reservoir located below a 1.5 mm of thickness phantom tissue.

Moreover, FITC-loaded active microneedles were compared against passive microneedles, where top view images taken at different time intervals (0, 5, 10 and 15 min) corroborate the accelerated diffusion of FITC significantly at the mark of 10 min, showing a larger radius of diffusion of the loaded dye due to Mg reactivity. The corresponding amperometry curves at 30 min are shown in Figure 2.1.11. Additionally, Figure 2.1.12 shows the corresponding absorbance spectra of IgG-Alexa Fluor-555 that passed through the phantom-mimicking tissue and measured at different time intervals (10, 20 and 30 min) using bare and active microneedles.

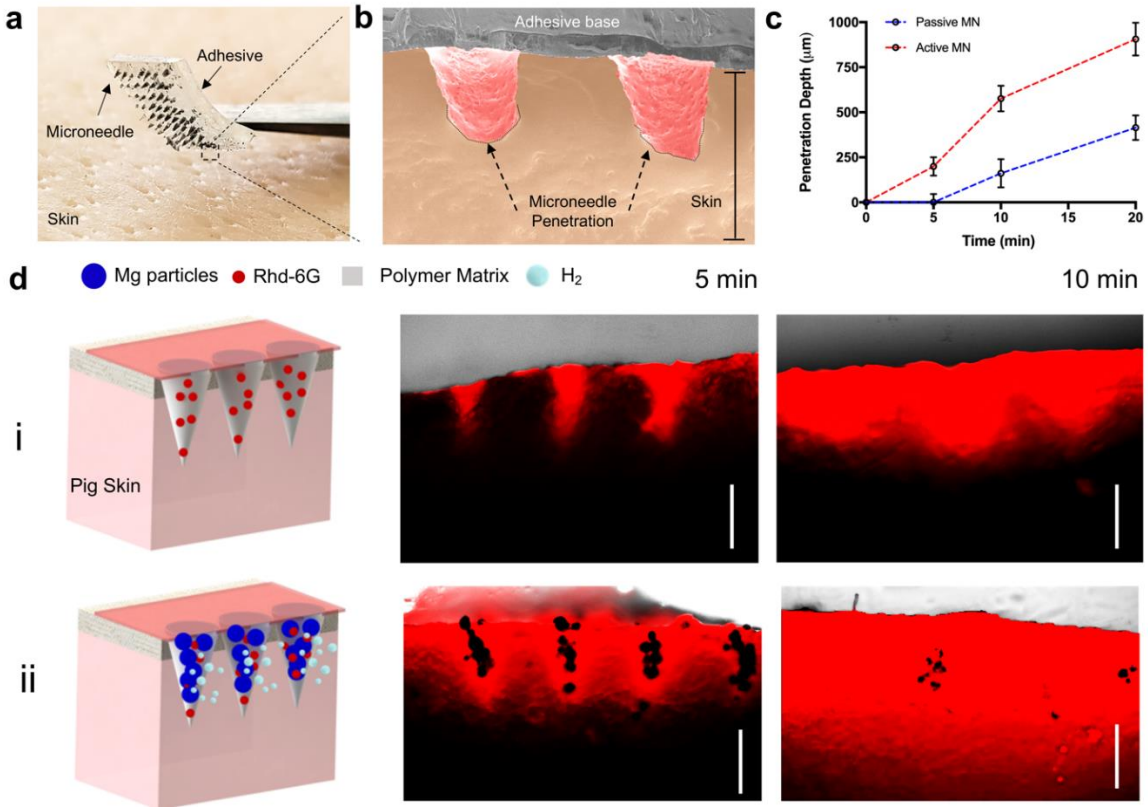

Figure 2.1.13 Evaluation of *ex vivo* dye release performance of passive and active microneedles. a) Digital photograph of an active microneedle patch (7x7 array) loaded with Rh6G before piercing porcine skin. b) Colored Scanning Electron Micrograph of 2 active microneedles piercing porcine skin. c) Corresponding penetration depth of Rh6G by microneedles at different time points, *n=3*. d) Schematic illustrating the experimental set up of both passive and active microneedles penetrating into porcine skin. Passive (i) and active (ii) microneedle arrays are shown, along with fluorescence microscopy cross-section images at different times. Scale bars, 500 μm.

Furthermore, an evaluation of the dye release performance of both passive and active microneedles was performed *ex vivo* using porcine skin. Figure 2.1.13a illustrates a digital photograph of an active microneedle array consisting of 49 microneedles loaded with the dye Rh6G, before piercing the porcine skin. The porcine skin was pretreated with glutaraldehyde before piercing with microneedles in order to characterize the

piercing capabilities. A colored scanning electron micrograph, shown in Figure 2.1.13b, clearly illustrate the successful penetration of two tips into deep tissue. The depth penetration results by piercing porcine skin with both passive and active microneedles were plotted and presented in Figure 2.1.13c. The penetration depth was plotted as a function of time, where the dye diffused across the skin from the microneedle structure. A schematic illustration of both passive and active microneedles piercing into porcine skin is illustrated in Figure 2.1.13d (left). The microneedle arrays were placed into a porcine skin rectangular area of 2 cm^2 and further examined at several time points (5, 10 and 20 min). Fluorescence cross section time-lapse images, illustrating the microneedle distribution inside the pork skin models are shown in Figure 2.1.13d (right). It should be noted that microneedles needed to be left in skin for at least 5 min to fully dissolve and deliver the payload. These data indicate that the entrapped Mg particles greatly enhanced the delivery of the model dye Rh6G payload by lateral and vertical routes, *vs.* the delayed delivery by passive microneedles, which starts at the 5 min mark. Such improved permeation and hence delivery is dramatically more pronounced at 10 min, where passive microneedles lead to an average value of 111±79 μm vs. the 526±71 μm value observed with the active microneedles.

Finally, we illustrate how to integrate the active and combinatorial delivery platforms as a complement to existing microneedle designs that are commonly based on passive delivery by creating spatially resolved active and passive microneedle zones onto a single patch towards fast/deep and slow sustained delivery, respectively.

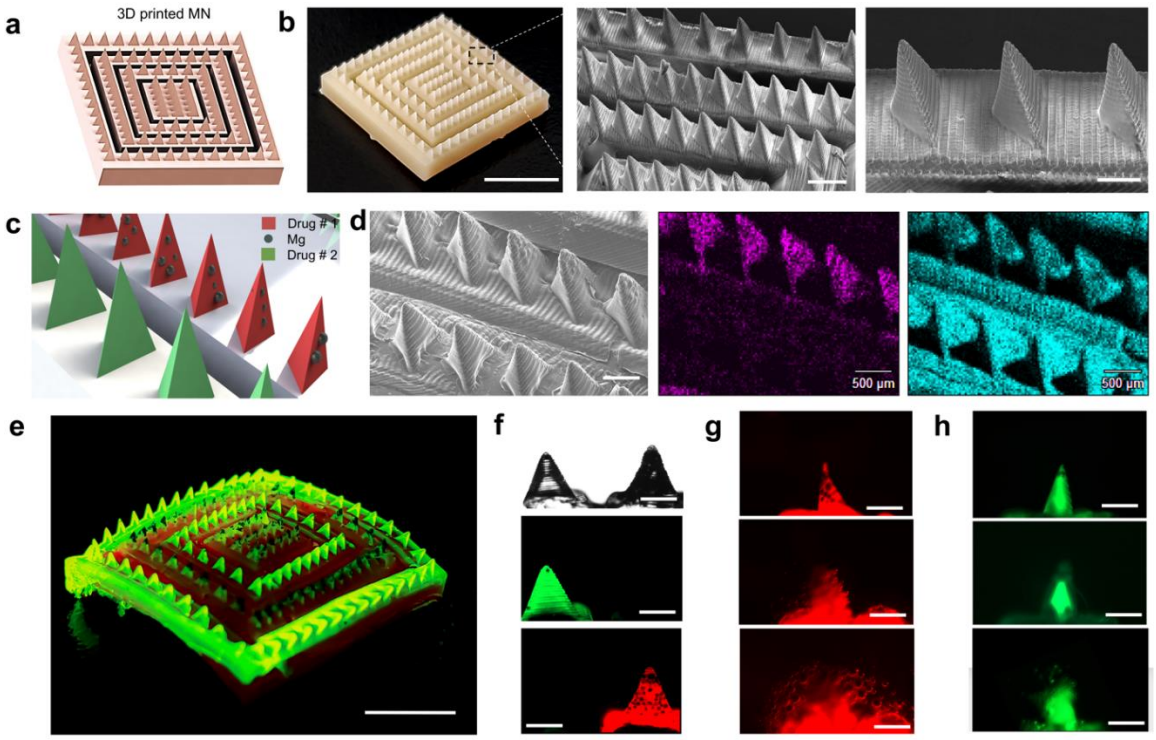

Figure 2.1.14 Combinatorial drug microneedle patch for the simultaneous dual delivery of different payloads. a) Schematic of square microneedle arrays as different active and passive compartments. b) Digital photograph of a 3D printed microneedle array by stereolithography and SEM images of needle rows with equal spacing. Scale bars, 5 mm, 1 mm and 500 µm respectively. c) Schematic of a combinatorial dissolvable microneedle patch with 2 different microneedle compartments (active and passive). d) Side- by-side SEM image of active and passive microneedles along with the corresponding EDX images illustrating the Mg in magenta, and C in cyan. Scale bars, 500 µm. e) Digital photograph of a combinatorial dissolvable microneedle patch loaded with FITC (passive delivery compartment) and Rh6G + Mg particles (active delivery compartment). Scale bar, 5 mm. f) Side-by-side optical and fluorescence microscopy images showing active and passive microneedles. Scale bar, 500 µm. g) Fluorescence time-lapse images show the dissolution of an active microneedle tip at 10 sec intervals. Scale bars, 500 µm. h) Fluorescence time-lapse images showing the dissolution of a passive microneedle tip. Scale bars, 500 µm.

The patch was fabricated by using a stereolithography 3D printer to generate a positive microneedle mold in which we engineered topological barriers (walls) to spatially separate the active and passive microneedle groups into different sections, thus

allowing to combine different materials and cargoes in the same patch design (Figure 2.1.14a). A digital photograph and scanning electron micrographs of the positive micromold (Figure 2.1.14b) clearly show in detail the distinct grooves that separate the microneedles into different sub-sections. SEM images illustrate in more detail the uniform spacing between such sections, and reproducible tip sharpness. Next, PDMS negative microneedle molds were fabricated and used to fabricate the combinatorial patch following the micromolding method described earlier but with the added capability of casting different polymers and cargo in each of the microneedle compartments Figure 2.1.14c.

A scanning electron micrograph of the polymeric combinatorial microneedle patch is shown in Figure 2.1.14d, where both passive and active microneedle rows are side by side. The corresponding EDX analysis clearly indicates that the Mg particles are present only in the active compartment. For better visualization, we loaded each compartment with model fluorescent dye payloads. The passive microneedle compartment was loaded with FITC and the active compartment with Rh6G. Such combinatorial loading of both dyes in a single microneedle patch is further illustrated in Figure 2.1.14e, which shows a digital photograph of the dual compartment under UV light illumination. The dual microneedle patch was characterized by fluorescence microscopy, where a side-by-side image shows the spatially resolved microneedles loaded with the different (dye) cargo (Figure 2.1.14f). To visualize the different activity of the microneedle tips, Figure 2.1.14g and h illustrate fluorescence time-lapse images, showing the dissolution of passive and active microneedles, where the active microneedle compartment dissolves and releases

Rh6G with the burst activation of Mg particles, and passive microneedles release the second cargo (FITC) at a slower rate of delivery. Details of the fabrication process are given in Figure 2.1.15.

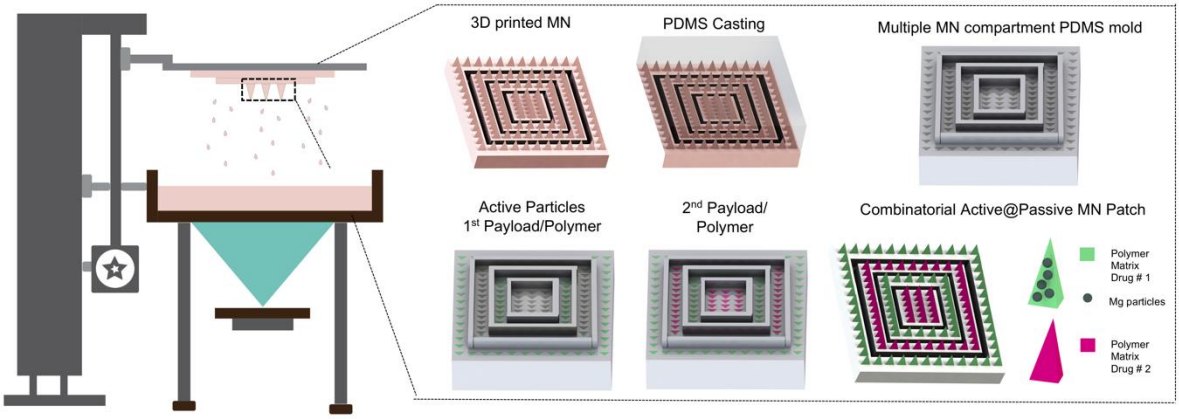

Figure 2.1.15 3D printing and fabrication steps of polymeric combinatorial microneedle patch with spatially resolved active and passive microneedle zones.

Our combinatorial approach can overcome the challenge of loading and delivering fast and slow multiple cargos as a single treatment administration with a microneedle dissolvable patch. The different microneedles in such combinatorial array can thus be tailored to present different release kinetics based on the materials used in fabrication, were ideally a burst-sustained release profile could help to enhance the low efficiency of current passive transdermal treatments.

2.1.4 Conclusions

We have demonstrated an effective microneedle delivery route that offers active payload delivery, without the use of external stimuli, towards improved therapeutic outcome vs commonly used passive diffusive microneedle transport. Such active,

degradable, and autonomous microneedle delivery has been realized through the incorporation of reactive Mg microparticles within the microneedle patch. The dissolution of these Mg particles (upon contact with the interstitial fluid) produces a remarkably high localized fluidic flow that results in a significantly faster and deeper intradermal local payload delivery. Such autonomous built-in mixing effect obviates the need for expensive and bulky external systems commonly used for triggering active microneedle delivery. Our methodology allowed the fabrication of a microneedle patch as well for combinatorial delivery using spatially resolved active and passive microneedle zones, for fast/deep and slow sustained release, respectively.

Moreover, the active microneedle delivery system is not limited to specific polymeric materials or microneedle geometry or dimensions The new ‘built-in’ active delivery strategy holds considerable promise for diverse practical biomedical applications for transdermal delivery, including drug delivery, immunotherapy, or cosmetic treatment, offering an attractive efficient delivery route compared to traditional passive microneedle patches, as well as being an ideal candidate to particularly benefit applications, such as pain killing and cardiac treatment, that require fast and deep payload delivery.

2.1.5 References

1. J. K. Hickling, K. R. Jones, M. Friede, D. Zehrung, D. Chen, D. Kristensen, Bull. World Health Organ. 2011, 89, 221.

2. E. Drucker, P. G. Alcabes, P. A. Marx, Lancet. 2001, 358, 1989.

3. A. Taddio, M. Ipp, S. Thivakaran, A. Jamal, C. Parikh, S. Smart, J. Sovran, D. Stephens, J. Katz, Vaccine 2012, 30, 4807.

4. K. Park, I. C. Kwon, K. Park, React. Funct. Polym. 2011, 71, 280.

5. K. Thanki, R. P. Gangwal, A. T. Sangamwar, S. Jain, J. Control. Release 2013, 170, 15.

6. A. GhavamiNejad, J. Li, B. Lu, L. Zhou, L. Lam, A. Giacca, X. Y. Wu, Adv. Mater. 2019, 1901051.

7. Y. C. Kim, J. H. Park, M. R. Prausnitz, Adv. Drug Deliv. Rev. 2012, 64, 1547.

8. J. Wang, Z. Wang, J. Yu, A. R. Kahkoska, J. B. Buse, Z. Gu, Adv. Mater. 2019, 1902004.

9. S. Bhatnagar, K. Dave, V. V. K. Venuganti, J. Control. Release 2017, 260, 164.

10. S. P. Sullivan, D. G. Koutsonanos, M. del Pilar Martin, J. W. Lee, V. Zarnitsyn, S.O. Choi, N. Murthy, R. W. Compans, I. Skountzou, M. R. Prausnitz, Nat. Med. 2010, 16, 915.

11. P. C. DeMuth, Y. Min, B. Huang, J. A. Kramer, A. D. Miller, D. H. Barouch, P. T. Hammond, D. J. Irvine, Nat. Mater. 2013, 12, 367

12. P. C. DeMuth, J. J. Moon, H. Suh, P. T. Hammond, D. J. Irvine, ACS nano 2012, 6, 8041.

13. J. Yu, Y. Zhang, Y. Ye, R. DiSanto, W. Sun, D. Ranson, F. S. Ligler, J. B. Buse, Z. Gu, PNAS 2015, 112, 8260.

14. Y. Ye, J. Yu, C. Wang, N. Y. Nguyen, G. M. Walker, J. B. Buse, Z. Gu, Adv. Mater. 2016, 28, 3115.

15. A. R. Denet, R. Vanbever, V. Préat, Adv. Drug Deliv. Rev. 2004, 56, 659.

16. S. O. Choi, Y. C. Kim, J. H. Park, J. Hutcheson, H. S. Gill, Y. K. Yoon, M. R. Prausnitz, M. G. Allen, Biomed. Microdevices 2010, 12, 263.

17. S. Mitragotri, D. Blankschtein, R. Langer, Science 1995, 269, 850.

18. F. Soto, I. Jeerapan, C. Silva-López, M. A. Lopez-Ramirez, I. Chai, L. Xiaolong, J. Lv, J. F. Kurniawan, I. Martin, K. Chakravarthy, J. Wang, Small 2018, 14, 1803266.

19. M. C. Chen, Z. W. Lin, M. H. Ling, ACS nano 2015, 10, 93.

20. L. Dong, Y. Li, Z. Li, N. Xu, P. Liu, H. Du, Y. Zhang, Y. Huang, J. Zhu, G. Ren, J. Xie, ACS Appl. Mater. Interfaces 2018, 10, 9247.

21. X. Xie, C. Pascual, C. Lieu, S. Oh, J. Wang, B. Zou, J. Xie, Z. Li, J. Xie, D. C. Yeomans, M.X. Wu, ACS nano 2016, 11, 395.

22. H. Lee, T. K. Choi, Y. B. Lee, H. R. Cho, R. Ghaffari, L. Wang, H. J. Choi, T. D. Chung, N. Lu, T. Hyeon, S. H. Choi, Nat. Nanotechnol. 2016, 11, 566.

23. H. Lee, C. Song, Y. S. Hong, M. S. Kim, H. R. Cho, T. Kang, K. Shin, S. H. Choi, T. Hyeon, D. H. Kim, Sci. Adv. 2017, 3, e1601314.

24. B. E. F. de Ávila, P. Angsantikul, J. Li, M. A. Lopez-Ramirez, D. E. Ramírez-Herrera, S. Thamphiwatana, C. Chen, J. Delezuk, R. Samakapiruk, V. Ramez, M. Obonyo, L. Zhang, J. Wang, Nat. Commun. 2017, 8, 272.

25. J. Orozco, G. Cheng, D. Vilela, S. Sattayasamitsathit, R. Vazquez-Duhalt, G. Valdes-Ramírez, O. S. Pak, A. Escarpa, C. Kan, J. Wang, Angew. Chem. Int. Ed. 2013, 52, 13276.

26. Z. Wu, J. Li, B. E.-F. de Avila, T. Li, W. Gao, Q. He, L. Zhang, J. Wang, Adv. Funct. Mater. 2015, 25, 7497.

27. S. R. Montezuma, J. Loewenstein, C. Scholz, J. F. I. Rizzo, Invest. Ophthalmol. Vis. Sci. 2006, 47, 3514.

28. H. Abd El-Mohdy, S. Ghanem, J. Polym. Res. 2009, 16, 1.

29. W. Li, R. N. Terry, J. Tang, M. R. Feng, S. P. Schwendeman, M. R. Prausnitz, Nat. Biomed. Eng. 2019, 3, 220.

30. S. F. Lahiji, Y. Kim, G. Kang, S. Kim, S. Lee, and H. Jung, Sci. Rep. 2019, 9, 7886.

31. S. Li, J. Zhao, P. Lu, Y. Xie, Sci. Bull. 2010, 55, 114.

32. J. H. Park, M. G. Allen, M. R. Prausnitz, Pharm. Res. 2006, 23, 1008.

33. Wang, L., Fan, Z., Zhang, J., Changyi, Y., Huang, C., Gu, Y., Xu, Z., Tang, Z., Lu, W., Wei, X. and Li, C. Int. J. Cancer. 2015. 136, E107.

2.2 Immune Checkpoint Inhibitor Melanoma Treatment by Active Microneedles

2.2.1 Introduction

Melanoma is considered one of the most threatening and contentious cancers over the past decade,[1] displaying high incidence numbers, lack of prognosis, poor or inadequate diagnosis and treatment. Among the current treatment alternatives surgery is considered the primary option, by the direct excision of the metastatic tumor.[2-4] In addition to surgery, priming the immune system by the delivery of immune checkpoint inhibitors has been a promising alternative by demonstrating good prognosis in more than 60% of the patients with advanced melanoma; unfortunately, a broad portion of them relapse.[5-8] Recent developments in the past years regarding cancer immunotherapy have overcome challenges and demonstrated the great importance of immunoregulatory techniques in the treatment of diverse types of cancer. Monoclonal antibodies that specifically target the programmed cell death protein (PD1) are being developed due to its ability to boost the immune system and hence treat cancer. Among all types of cancer, skin cancers have become the most common ones in humans. Estimates are that one in five Americans will develop skin cancer in their lifetime.[9] Therefore, the development of improved, practical, and efficient delivery methods is urgently needed.[10]

Here, we present an engineered active bio dissolvable and degradable microneedle delivery platform made of polyvinylpyrrolidone (PVP) loaded with an immune checkpoint inhibitor (anti-CTLA-4). The microneedle structure is comprised of a water-soluble polymeric matrix (PVP) with enclosed Mg microparticles (30-100μm) mixed along anti-CTLA-4. We chose to test the active *vs.* passive delivery of checkpoint

blockade antibody anti-CTLA-4 (Clone: 9H10, BioXcel). Anti-CTLA4 checkpoint blockade is an immunotherapy that has been FDA-approved for the treatment of melanoma in 2011, is in clinical trials targeting other solid tumors[11,12] and it has been recognized to be a susceptible therapy in B16F10 melanoma model.[13]

The distinct delivery and therapeutic advantages of the active autonomous microneedle platform are demonstrated in a B16F10 mouse melanoma model where the active treatment led to a dramatically improved animal survival. The enhanced therapeutic index may be explained by the enhanced permeation of the therapeutic antibodies through the tumor (as demonstrated in an ex vivo model) therefore improving its distribution as well as changes (increase) in the tumor pH environment due to the hydrogen depletion of Mg particles.

2.2.2 Experimental Methods

Microneedle patch fabrication

A volume of 250 μL of a 10% w/v polymer (Polyvinylpyrrolidone (PVP) average Mw~360,000, Sigma Aldrich) aqueous solution of pH 7 was added onto the PDMS microneedle mold and further placed in a closed desiccator in vacuum for 5-10 min (23 in Hg). Molds were removed from desiccator with the further removal of bubbles generated at interface between microneedle pores and solution with the use of plastic 1mL disposable transfer pipettes or the use of a tweezer. Later, bubbles in the surface of the solution were removed, or popped with the use of a pipette or needle tip and 100ug of anti-CTLA-4 (100 μg, Clone, 9H10, BioXcell) was added to the mold and let it to dry for

24-72 hours. Repetitive additions of the polymer were made until reaching 1 mL. Once microneedle patches were ready, a 1 cm^2 scotch tape was applied on top of the needles and peeled off from the PDMS mold. Microneedle patches were stored at room temperature prior to use. Active microneedles were fabricated by employing the same procedure but before casting the polymer onto the mold, 50µL of a 5mg/mL stock Mg microparticle (catalog #FMW40, from TangShanWeiHao Magnesium Powder Co., Ltd China) in isopropanol suspension was casted and infiltrated within the negative microneedle features of the PDMS mold. A PVP solution of pH 10.5 was used to prevent Mg particles to react, ensuring a proper microneedle patch fabrication.

Cell line

The B16F10 cell line was acquired from American Type Culture Collection (ATCC). B16F10 cells were cultured in Dulbecco's Modified Eagle's Medium (DMEM, Life Technologies), supplemented with 10% (v/v) fetal bovine serum (FBS, Atlanta Biologicals) and 1% (v/v) penicillin-streptomycin (Life Technologies). Cells were maintained at 37°C, 5% CO2. The cell cultures were maintained below a 50% confluence and early passage culture were utilized for the experiments.

In vivo efficacy study in mice

All experiments were conducted in accordance with UCSD's Institutional Animal Care and Use Committee (IACUC). 6- to 8-week-old female C57BL/6 mice (The Jackson Laboratory) were used. 25,000 B16F10 cells were suspended in 50 µL PBS and were injected intradermally into the right flank of C57BL/6 mice on day 0. PBS or anti-

CTLA4 antibody (100 μg, Clone, 9H10, BioXcell) was administrated into mice by intratumoral injection (30 μL) or by microneedle on day 10 and day 17. Tumor volumes were measured using a digital caliper. The tumor volume (mm^3) was calculated as (long diameter short diameter^2)/^{2}. Animals were sacrificed when tumor volume reached 1500 mm^3. For the blank active microneedle control, a single patch was administered on day 10.

Histology

Haematoxylin and eosin (H&E) staining of kidneys, livers, lungs, and spleens sections of the mice treated with active microneedle were evaluated at 60 days after tumor inoculation by histology analysis. Organs from PBS treated mice were evaluated when tumor volume reached 1500 mm^3.

2.2.3 Experimental Results

The *in vivo* therapeutic efficacy of the active transport method was evaluated using a syngeneic and orthotopic mouse model of melanoma; specifically, B16F10 cells were grown dermally using C57Bl6 mice. On days 10 and 17 post tumor challenge, various treatment groups were administered intratumorally; PBS control *vs.* free anti-CTLA4 *vs.* passive microneedle *vs.* active microneedle (Figure 2.2.1a). For both microneedle experiments, the patches were applied manually into the mice right flank for 15 min. The efficacy was assessed by measuring the tumor growth rate and survival. As expected, free anti-CTLA-4 Ab treatment delayed tumor growth compared to untreated animals (PBS control group). However, both the passive microneedle and active microneedle showed

significantly enhanced antitumoral effects, achieving substantial tumor suppression (Figure 2.2.1b and c, respectively).

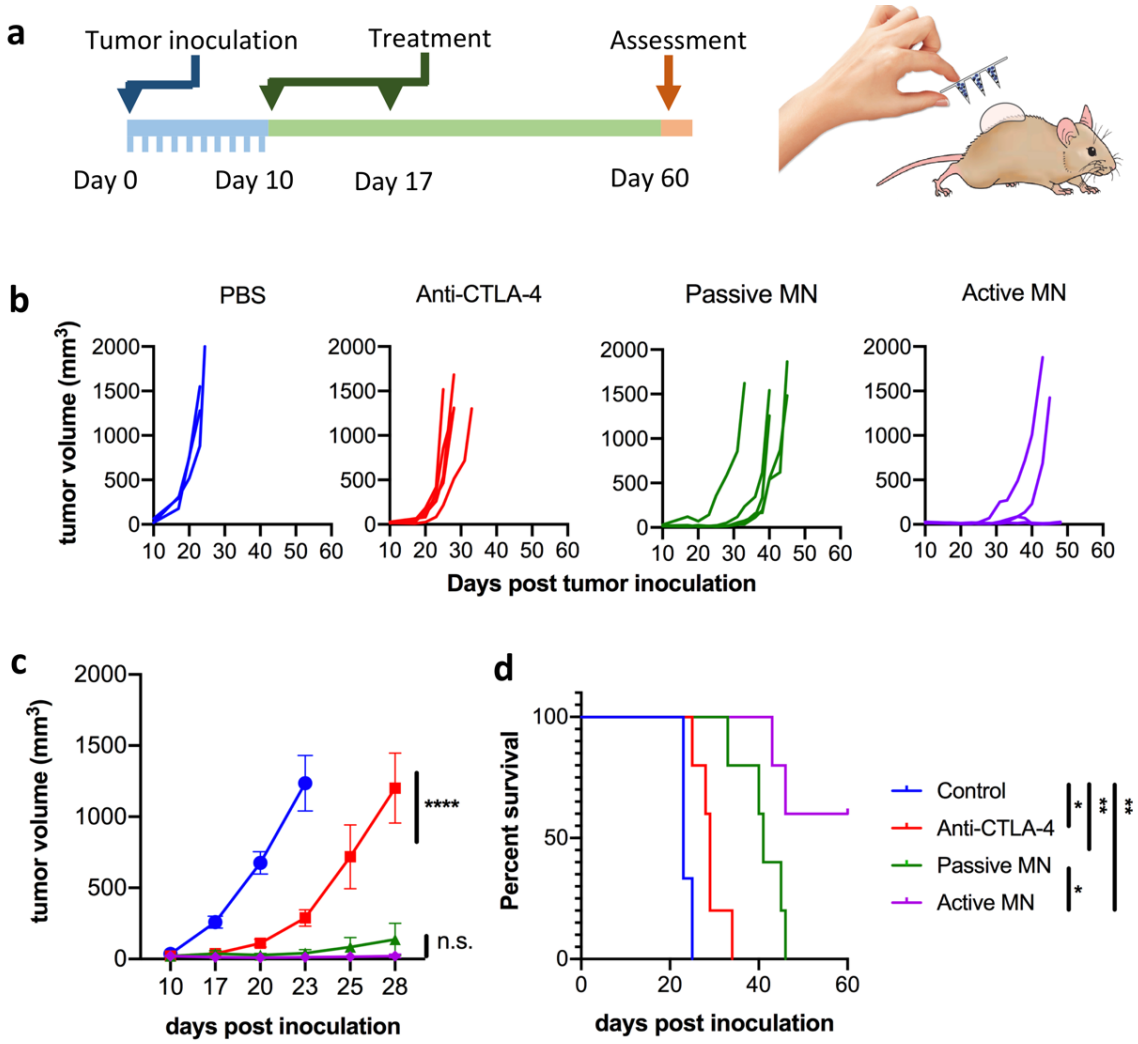

Figure 2.2.1 *In vivo* melanoma tumor eradication by active microneedles a) *In vivo* skin cancer treatment using anti-CTLA-4 antibodies delivered by active vs. passive microneedles and intratumoral injection in B16F10 dermal melanoma model. b) Tumor volumes growth curve of individual mice and averaged tumor volumes of mice receiving PBS (blue), free anti-CTLA-4 (red), anti-CTLA-4 passive microneedle (green), and anti-CLTA-4 active microneedle (purple). Data are means ± SEM (n=3-5). c) Tumor growth over time was compared by two-way ANOVA with Tukey's test: ****$p<0.0001$, n.s. no significant difference. d) Survival rates. Statistical significance was calculated using Log-rank (Mantel-Cox) test: *$p<0.05$, **$p<0.01$.

Passive microneedle delivering the therapeutic anti-CTLA-4 Ab significantly delayed tumor growth; nevertheless, by day 46 all animals in this group had to be sacrificed due to tumor burden exceeding 1500 mm^3. In stark contrast, 60% of the animals treated using the active delivery microneedle platform showed a complete response and were tumor-free and survived past day 60 (Figure 2.2.1d). Corresponding blank active microneedle control it is shown in Figure 2.2.2.

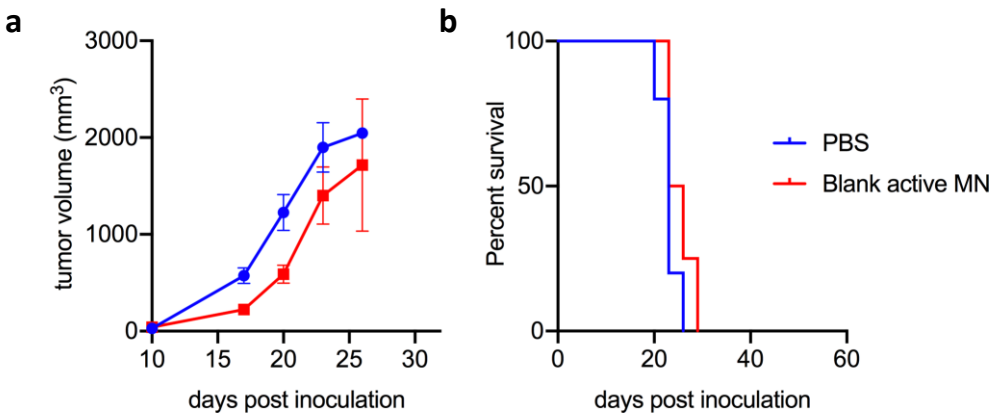

Figure 2.2.2 a) Tumor volumes growth curve of averaged tumor volumes of mice receiving PBS (blue, n=5), blank active microneedle (red, n=4). b) Survival rates of PBS and blank active microneedle treated groups.

We hypothesize that the dramatically improved efficacy is due to the active delivery mechanism. Based on the aforementioned *ex vivo* data, we hypothesize that the burst "fast" release mechanism of action, with built-in pumping action associated with the embedded Mg motors can be helpful in enhancing the permeation of anti-CTLA through the tumor, therefore improving its distribution as achieved in previous ex vivo model. Furthermore we hypothesize that changes (i.e. increase) in the tumor pH environment by

the hydrogen depletion of Mg particles is also expected to contribute to enhancing the therapeutic effect, as it has been reported by the delivery of immune checkpoint inhibitors and alkalization agents.[14,15] Additionally, the active delivery mechanism is a promising therapy modality with a synergistic effect to work as a pump to enhance the permeation of the payload and the intratumoral production of localized microbubbles (hydrogen therapy), that lead to antitumoral effects,[16,17] We evaluated the safety of the materials used in the active microneedle (Mg and PVP) and their subsequent by products (magnesium hydroxide), by performing toxicity studies in mice. Analysis of kidney, liver, lung and spleen indicated that no apparent systemic toxicities associated with the active or passive microneedle treatment (Figure 2.2.3).

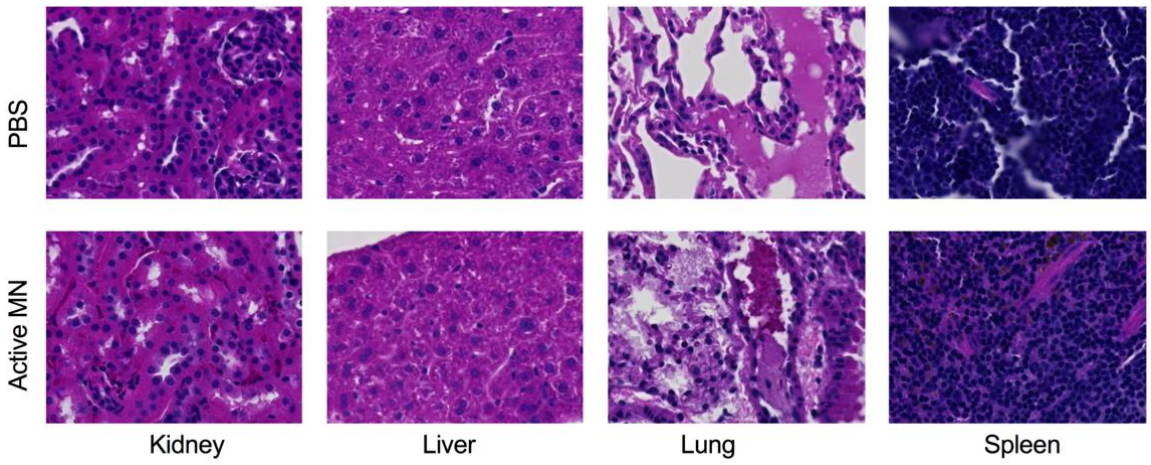

Figure 2.2.3 Histological assessment of the kidney, liver, lung, and spleen in PBS-treated and active microneedle treated mice.

2.2.4 Conclusions

The therapeutic advantages of such active transport were demonstrated from the greatly enhanced *in vivo* efficacy observed using a syngeneic and orthotopic mouse model of melanoma. *In vivo* experiments using a B16F10 mouse melanoma model demonstrate that the active delivery of anti-CTLA-4 (a checkpoint inhibitor drug) results in greatly enhanced immune response and significantly longer survival. In future work we plan to further study the immunological profile to fully delineate the mechanism of this therapy modality.

2.2.5 References

1. V. Gray-Schopfer, C. Wellbrock, R. Marais, Melanoma biology and new targeted therapy. Nature 2007, 445, 851.

2. R. Essner, J. H. Lee, L. A. Wanek, H. Itakura, and D. L. Morton. Arch. Surg. 139, 2004, 961–967.

3. P. J. Allen, D. G. Coit, Ann. Surg. Oncol. 2002, 9,762–770.

4. A. M. Leung, D. M. Hari, D. L. Morton, Cancer journal, 2012, 18, 176.

5. C. Imbert, A. Montfort, M. Fraisse, E. Marcheteau, J. Gilhodes, E. Martin, F. Bertrand, M. Marcellin, O. Burlet-Schiltz, A. G. de Peredo, V. Garcia, Nat. Commun. 2020, 11, 1–14.

6. J. Larkin, V. Chiarion-Sileni, R. Gonzalez, J. J. Grob, C. L. Cowey, C. D. Lao, D. Schadendorf, R. Dummer, M. Smylie, P. Rutkowski, P. F. Ferrucci, N. Engl. J. Med. 2015, 373, 23–34.

7. M. K. Callahan, H. Kluger, M. A. Postow, N. H. Segal, A. Lesokhin, M. B. Atkins, J. M. Kirkwood, S. Krishnan, R. Bhore, C. Horak, J. D. Wolchok, J. Clin. Oncol. 2018, 36, 391.

8. C. Robert, J. Schachter, G. V. Long, A. Arance, J. J. Grob, L. Mortier, A. Daud, M. S. Carlino, C. McNeil, M. Lotem, J. N. Engl. J. Med. 2015, 372, 2521–2532.

9. Stern R. S. Arch Dermatol. 2010, 146, 279-82.

10. E. Drucker, P. G. Alcabes, P. A. Marx, Lancet 2001, 358, 1989–1992.

11. E. J. Lipson, C. G. Drake, Clin. Cancer Res. 2011, 17, 6958.

12. P. Kvistborg, D. Philips, S. Kelderman, L. Hageman, C. Ottensmeier, D. Joseph-Pietras, M. J. Welters, S. van der Burg, E. Kapiteijn, O. Michielin, E. Romano, Sci. Transl. Med. 2014, 6, 254ra128.

13. M. A. Curran, W. Montalvo, H. Yagita, J. P. Allison, PNAS. 2010, 107, 4275

14. S. Pilon-Thomas, K. N. Kodumudi, A. E. El-Kenawi, S. Russell, A. M. Weber, K. Luddy, M. Damaghi, J. W. Wojtkowiak, J. J. Mulé, A. Ibrahim-Hashim, R. J. Gillies, Cancer Res. 2016, 76, 1381.

15. J. Li, P. Angsantikul, W. Liu, B. E-F. de Ávila, S. Thamphiwatana, M. Xu, E. Sandraz, X. Wang, J. Delezuk, W. Gao, L. Zhang, J. Wang, Angew. Chem. Int. Ed. 2017, 56, 2156.

16. Y. Wu, M. Yuan, J. Song, X. Chen, H. Yang, ACS nano 2019, 13, 8505.

17. A. Zandi, M. A. Khayamian, M. Saghafi, S. Shalileh, P. Katebi, S. Assadi, A. Gilani, M. S. Parizi, S. Vanaei, M. R. Esmailinejad, F. Abbasvandi, Adv. Healthcare Mater. 2019, 8, 1900613.

2.3 Active Microneedle Administration of Plant Virus Nanoparticles for Cancer in situ Vaccination

2.3.1 Introduction

Transdermal microneedle patch administration has the potential to improve delivery of therapeutics for a multitude of applications. Compared to traditional needle-based injection, microneedles enhance the intradermal drug penetration, distribution, and therapeutic efficacy through sustained/controlled, and often slowed, release of a payload therapeutic agent, based primarily on passive diffusion. Additionally, the minimal training required from medical personnel and absence of sharp biohazardous waste make microneedle attractive for remote location operation. Preclinical studies have demonstrated potent efficacy of this approach, and the technology is poised to make a clinical impact. This method of administration has been successfully employed for delivery of cytotoxic chemotherapy and immunotherapy.[1–4] Studies of microneedle administration for cancer immunotherapy have focused primarily on intradermal delivery of nucleic acid- and antigen-based vaccines[5–8] as well as intratumoral (IT) delivery of immune checkpoint inhibitors[9,10] for the treatment of cutaneous tumors, including melanoma. For example, a transdermal microneedle patch used for IT administration of anti-PD1 antibodies showed increased efficacy compared to needle injection. This efficacy was related to increased distribution and prolonged retention of the anti-PD1 antibody within the tumor.[9]

While gradual, sustained release of some therapeutics may improve the efficacy of microneedle, different clinical circumstances may benefit from a rapid, forceful payload

release, IT drug administration with conventional needle injections can be challenging. The high interstitial fluid pressure (IFP) within solid tumors tends to form gradients directed away from the center of the tumor. IFP and heterogeneous tumor architecture contribute to nonuniform penetration and distribution of drugs within tumors. IFP also may limit the safe injectable volume and promote post-injection leakage of drug.[11,12] Transdermal microneedles allow delivery of equivalent doses in smaller volumes, distributed more evenly over the tumor surface, but passive diffusion of drugs from the microneedle may still exhibit limited permeation within the tumor. For immunotherapeutic agents that are larger than 10 nm antibodies[13], tissue penetration based solely on diffusion-based methods may also be more restricted.

Active drug delivery platforms can improve efficiency of transport and permeation of therapeutic payload compared to methods based on passive diffusion. Active drug delivery, however, often requires external energy triggers, such as electricity,[14,15] light,[1,2] temperature,[16,17] or ultrasound,[18,19] which limit their accessibility and convenience. Self-contained, synthetic nano/micromotors[20,21] may be enclosed within dissolvable microneedle patches to create an autonomous active delivery platform, referred to as an active microneedle patch, thus, obviating the need for external triggers. Recently, we demonstrated that magnesium (Mg) micromotor-loaded active microneedles enhanced therapeutic efficacy compared to diffusion-based passive microneedles (dissolvable microneedles lacking active components), for the IT delivery of an immune checkpoint inhibitor in a murine model of melanoma.[22] The built-in active microneedle improved response is attributed to the Mg microparticle performance with the weakly acidic TME,

rapidly generating hydrogen gas bubbles and exerting a propulsive force onto the payload antibody molecules driving them into tissue.[22] The active microneedle delivery platform provides significant force for delivering drug payloads, which may overcome physical impedances to passive diffusion within the TME.

Transdermal microneedle technology holds great potential to facilitate direct, active IT delivery of therapies for treatment of cutaneous tumors. Thus, it is well-suited for another compelling approach to cancer immunotherapy, *in situ* vaccination. *In situ* vaccination involves the direct application of immunostimulatory molecules, or immunoadjuvants, into a tumor. Unlike traditional vaccination, *in situ* vaccination utilizes the tumor as a source of intrinsic tumor-associated antigens (TAAs) to induce targeted antitumor adaptive immune responses. We have previously shown that needle-injection administered *in situ* vaccination with cowpea mosaic virus nanoparticles (CPMV) is effective in treating a variety of murine tumor models[23–30] and canine melanoma.[31] CPMV *in situ* treatment vigorously activates the innate immune system, shifting the profile of cytokines and innate immune cells within the immunosuppressive tumor microenvironment (TME) toward an immunostimulatory state.[26–28] CPMV *in situ* vaccination also promotes tumor infiltration and activation of APCs[25–28] to engage in cross presentation of TAAs, to activate effector T cells with specificity against the tumor.[26] This primes a systemic, targeted, durable antitumor adaptive immune response, resulting in a personalized and selective therapy.

Melanoma exhibits high levels of IT heterogeneity, with clonal populations arising due to a variety of selection pressures.[32,33] For *in situ* vaccination, it is critical to

distribute CPMV evenly throughout the tumor tissue to attract APCs to sample and present TAAs from all clonal populations within a single tumor. Microneedle patches distribute the therapeutic payload over an array of microneedles; and thus, offer more uniform delivery throughout the tumor volume. This reduces the reliance on the nonuniform techniques and abilities of administering physicians to distribute the therapeutic throughout the tumor. In addition, CPMV is a larger molecule (30 nm) than most immunotherapeutic agents that have been successfully administered via passive, diffusion-based microneedles; thus, active delivery-based administration may promote greater tissue penetration than passive microneedles.

We hypothesize that greater tumor tissue penetration using an active transdermal microneedle delivery system could further enhance the efficacy of CPMV *in situ* vaccination for mouse model of cutaneous melanoma. However, the critical determining factors of the efficacy and dynamics of the immune responses with CPMV *in situ* vaccination in the context of active microneedle administration are not well understood. To explore this, we have engineered an autonomous and biocompatible novel delivery platform incorporating immunostimulatory CPMV nanoparticles and Mg-based active microneedle delivery into dissolvable biodegradable microneedle patches. In the following sections we characterize such active microneedle delivery patch, the corresponding spatiotemporal distribution of the payload CPMV and immune response and demonstrate the enhanced therapeutic efficacy of such rapid microneedle CPMV release for improved *in situ* vaccination against the B16F10 model of melanoma.

2.3.2 Experimental Methods

PDMS microneedle mold fabrication

The fabrication of the PDMS negative microneedle molds was performed by casting a PDMS 8.6/1.4 (base/curing agent) solution (SYLGARD® 184) over a conical master microneedle mold made of acrylate resin (black-colored AnyCubic photon). Subsequently, PDMS was degassed for 15 minutes by placing the mold within a sealed desiccator connected to a vacuum pump running at 23 in Hg. Furthermore, the mold was left for 1 h at room temperature and later placed in an oven at 85 ^{o}C for 30 minutes. After the curing process, the negative mold was demolded from the master microneedle mold and resized with a blade cut. Prior use, each PDMS microneedle mold was cleaned/washed by triplicate with soap, ultrasonicated, temperature treated (80^{o}C), and stored in a sealed container.

Fabrication of the active microneedle patch

The active microneedle vaccination patches were fabricated by a micromolding technique with the use of negative PDMS microneedle molds. Briefly, 50 µL of a Mg microparticle (catalog #FMW40, from TangShanWeiHao Magnesium Powder Co., Ltd China) 2-propanol solution (50 mg/mL) was added to the negative microneedle mold to pack the cavities. Furthermore, a volume of 250 µL of a 10% w/v polyvinylpyrrolidone (PVP, MW = 360 K, Sigma Aldrich) aqueous solution (pH 10.5 and pH 7.4) was casted over the negative molds in a closed desiccator at 23 in Hg for a total time of 10 minutes. Afterwards, bubbles were removed from the mold needle interface and repetitive

additions of PVP solution were added to reach a total volume of 750 µL. The corresponding payload (100 µg of CPMV, Cy3-CPMV or Cy5-CPMV) was incorporated onto the mold and allowed to dry for 48 hours at room temperature in a sealed container. Upon drying, a circular 1.2 mm adhesive (3M scotch tape) was applied to the backing of the microneedle patches and demolded. Passive microneedles were formulated by following identical preparation steps, however, the inclusion of Mg microparticles was not performed, respectively. Both active microneedle and passive microneedle patches were stored at room temperature in a sealed container prior to use. For larger or more bulky tumors, microneedle patches were cut into 4 or 9 pieces to facilitate application.

microneedle patch imaging characterization and dissolution experiments

The fluorescent microscopy images of the active microneedle platform were performed by the use of an EVOS FL microscope (2x and 4x objectives and RFP fluorescent filter) for the Cy3-CPMV imaging. Furthermore, the SEM images were obtained with the use of a FEI Quanta 250 ESEM instrument (Hillsboro, Oregon, USA). Samples were sputtered with Iridium (Emitech K575X Sputter Coater) to provide a fine grain metal deposition and imaged with acceleration voltages between 3-5 keV. For the dissolution experiments, arrays of only 3 conical active microneedles were attached horizontally to a clear glass slide. To capture the dissolution in real time, PBS pH 6.5 was added to the microneedle array and images were taken with the use of an inverted optical microscope (Nikon Eclipse Instrument Inc. Ti-S/L100) coupled with a 4x microscope objective, a Hamamatsu digital camera C11440, and a NIS Elements AR 3.2 software.

Release Kinetics Experiments

After the microneedle patch fabrication, passive microneedle and active microneedle patches were used to pierce a phantom tissue. The synthetic phantom tissues were formulated with a 2% (w/v) Agarose (Sigma Aldrich) aqueous solution and further molded in custom made negative EcoFlex molds (1.5 mm diameter, 3 mm thickness). Phantom tissues were stored submerged in PBS (pH 6.5) and completely sealed prior to use. For testing, the passive microneedle and active microneedle patches loaded with Cy3-CPMV penetrated the phantom tissues for different durations: 1, 3, 5, 10, 20 and 30 minutes at 37.5 °C. Following application, the patches were removed from the tissue and dissolved in 800 µL of PBS pH 6.5. The use of a UV-2450 Shimadzu spectrophotometer was used for the absorbance measurements from a 400-700 nm spectrum window and the release from patches was plotted vs time. Data was analyzed and charts were generated using Prism 7 (GraphPad software).

Active microneedle compression test

The mechanical compression test was performed by the use of a Force Gauge Model M4-20 system Mark0-10 Series 4. In brief, an active microneedle array was set under a constant load, and the displacement of the base plate in reference to each needle height was monitored and plotted. The fracture (failure) force was determined by a notorious drop in force.

Cell line

The B16F10 cell line was acquired from American Type Culture Collection (ATCC). B16F10 cells were cultured in Dulbecco's Modified Eagle's Medium (DMEM, Life Technologies), supplemented with 10% (v/v) fetal bovine serum (FBS, Atlanta Biologicals) and 1% (v/v) penicillin-streptomycin (Life Technologies). Cells were maintained at 37 °C, 5% CO_2. The cell cultures were maintained below a 50% confluence and early passage culture were utilized for the experiments.

Expression and purification of CPMV nanoparticles

CPMV was propagated in California Blackeye No. 5 cowpea plants and purified as previously described.[34]

Bioconjugation of Cy3 and Cy5 fluorophores to CPMV external lysine residues

The CPMV protein capsid consists of 180 coat proteins upon which 300 surface-exposed lysine side chains are displayed.[35] CPMV nanoparticles were labeled with sulfo-Cy5-NHS (Abcam) using N-hydroxysuccinimide-activated esters that target the surface lysine residues. The reactions were carried out with a 1,200-fold CPMV molar excess of sulfo-Cy5-NHS in a 0.1 M KP buffer (pH 7.0) at room temperature overnight, with agitation. This yielded approximately 30 Cy5 fluorophores conjugated to each CPMV. For Cy3 the reactions were carried out with a 3,000-fold CPMV molar excess of sulfo-Cy3-NHS, which yielded approximately 50-70 Cy3 fluorophores per CPMV. Fluorophore-conjugated CPMV was characterized by UV-visual spectral analysis,

transmission electron microscopy, gel (SDS-PAGE and 1.2% (w/v) agarose) analysis as previously described.[36,37]

In vivo efficacy study in mice

All experiments were conducted in accordance with UCSD's Institutional Animal Care and Use Committee. 6- to 8-week-old female C57BL/6 mice (The Jackson Laboratory) were used. For larger tumors, 250,000 B16F10 cells were suspended in 30 μL PBS and were injected intradermally into the right flank of each C57BL/6 mouse on day 0. PBS (30 μL) or CPMV (100 μg in 30 μL) were administered by IT injection into the base of the tumor or by microneedle patch on day 7. Microneedles were applied on the tumors for 5-10 minutes until the needles completely dissolved. A PBS solution of pH 5.1 was applied to the skin of the treated region, immediately following application of the active microneedle patch. For smaller tumors, 25,000 B16F10 cells were suspended in 50 μL PBS and were injected intradermally into the right flank of each C57BL/6 mouse on day 0. PBS (30 μL) or CPMV (100 μg in 30 μL) were administered into mice by IT injection or by microneedle on day 10. Tumor volumes were measured using a digital caliper. The tumor volume (mm^3) was calculated as (long diameter×short $diameter^2$)/2. Animals were sacrificed when tumor volume reached ≥ 1500 mm^3.

Tumor immunofluorescence imaging

250,000 B16F10 cells were injected intradermally into the left flank of each C57BL/6 mice on day 0 as described previously. When tumors reached a volume of 60-100 mm^3, IT PBS (30 μL) injection, Cy5-CPMV (100 μg in 30 μL) injection, passive microneedle,

or active microneedle patch Cy5-CPMV (100 μg) were administered. 24 h post treatment, tumors excised en bloc from flank with 2-3 mm margin of normal surrounding skin. Tissue was flash frozen in OCT media with isopentane (cooled by dry ice to -78.5℃). Tumors were cryo-sectioned into 5 μm transverse sections (orthogonal to the longest axis).Tumor sections were fixed with cooled 100% acetone (-20℃), then washed with PBS and blocked (1X PBS / 5% (v/v) normal goat serum (Cell Signaling Technology, 5425S)/0.3% (v/v) Triton X-100) for 1 h at room temperature. Primary antibody staining was subsequently performed overnight at 4℃ with rabbit anti-mouse CD31/PECAM1 polyclonal antibody (Abcam, ab28364) at 1:50 dilution and rat anti-mouse CD45 (Cell Signaling Technology, clone 30-F11) at 1:800 dilution. Sections were then washed in PBS and stained with secondary antibodies (anti-rabbit Alexa Fluor 568 (Abcam, ab175471) at 1:1000 and anti-rat Alexa Fluor 488 (Cell Signaling Technology, 4416S) at 1:500) at room temperature for 2 h. After washing with PBS and drying, sections were counterstained and cover slipped with Prolong® Gold Antifade Reagent with DAPI (Cell Signaling Technology, 8961S). Sections were visualized on Keyence BZ-X710 all-in-one microscope (Keyence Corporation) with filter set (DAPI, TRITC, FITC, and Cy-5) and accompanying imaging analysis software.

Tumor *in vivo* fluorescence imaging

The IVIS *in vivo* imaging system (IVIS Xenogen 200, Perkin Elmer) was used for non-invasive visualization and analysis of cutaneous distribution and retention of Cy5-CPMV administered via IT conventional injection, passive microneedle, and active microneedle *in vivo*. Mice were fed an alfalfa-free diet (PicoLab High Energy Mouse

Diet, 5LJ5) starting at least 1week prior to imaging. 250,000 B16F10 cells were injected intradermally into the left flank of each C57BL/6 mouse on day 0 as described previously. When tumors reached a volume of 60-100 mm^3, IT PBS injection, Cy5-CPMV injection, passive microneedle, or active microneedle patch Cy5-CPMV were administered, with doses as described previously. Mice were imaged with the Cy5.5 filter (excitation range 615-665 nm and emission range 695-770 nm, 0.5 s exposure) under anesthesia, before treatment (baseline or 'BL'), and after treatment at specified timepoints (0 h, 4 h, 8 h, 12 h, 24 h, 36 h, 48 h, 72 h, and 96 h). Living Image Software (version 4.3.1, Perkin Elmer) was used to analyze all fluorescence data in this study. A region of interest (ROI) was drawn around each tumor and the measured fluorescence (in radiant efficiency, $(p/sec/cm^2/sr)/(\mu W/cm^2)$) was calculated and normalized to the baseline ROI fluorescence for each tumor.

Flow cytometry

For tumor immunoprofiling and splenocyte interferon release assays, fresh, single-cell suspensions were made from excised B16F10 melanomas and spleens, respectively. Cells were washed in cold PBS containing 1 mM EDTA, and then resuspended in staining buffer (PBS containing 2% (v/v) FBS, 1 mM EDTA, 0.1% (w/v) sodium azide). Fc receptors were blocked using anti-mouse CD16/CD32 (BioLegend) for 15 min and then tested with the following fluorescence-labeled antibodies (BioLegend) for 30 min at 4°C: CD45 (30-F11), CD11b (M1/70), CD86 (GL-1), major histocompatibility complex class II (MHCII, M5/114.15.2), Ly6G (1A8), CD11c (N418 A), F4/80 (BM8), Ly6C (HK1.4), NK1.1 (PK136), CD4 (GK1.5), CD3ε (145-2V11 A), CD8α (53-6.7), CD44

(IM7), CD62L (MEL-14), and isotype controls. For intracellular cytokine staining, splenocytes (10^6 cells/mL) were co-cultured with freeze-thawed B16F10 melanoma cell lysate (10^6 cells/mL) or CPMV (0.1 mg/mL) for 48 h and treated with brefeldin A (10 mg/mL) for the last 5 h at 37 °C. Following staining for surface antibodies as described above, the cells were fixed in 3% (w/v) paraformaldehyde, permeabilized with 0.1% (w/v) saponin, then incubated with anti-IFN-γ (XMG1.2, BioLegend) for 30 min in 0.1% (w/v) saponin. Cells were washed twice and resuspended in staining buffer for data acquisition. Flow cytometry was carried out using a BD LSRII cytometer (BD Biosciences), and the data were analyzed using FlowJo software (Tree Star). OneComp eBeads (eBiosciences) were used as compensation controls.

Statistics

Data was analyzed and statistical testing performed using Prism 7 (GraphPad software).

2.3.3 Experimental Results

The active microneedle delivery system was incorporated with a patch design to facilitate application in treatment of a murine dermal melanoma model. The materials of which the microneedles were composed, the size of the microneedles, and the size of the patch serving as the platform from which the microneedles extend, are all important factors. The active microneedle patch is comprised of a water-soluble polymer matrix made of a high molecular weight Polyvinylpyrrolidone (PVP), which serves as an

enclosure for the active Mg microparticles (30-100 μm in diameter) and the therapeutic payload of CPMV nanoparticles, both loaded within the structure (Figure 2.3.1a and b).

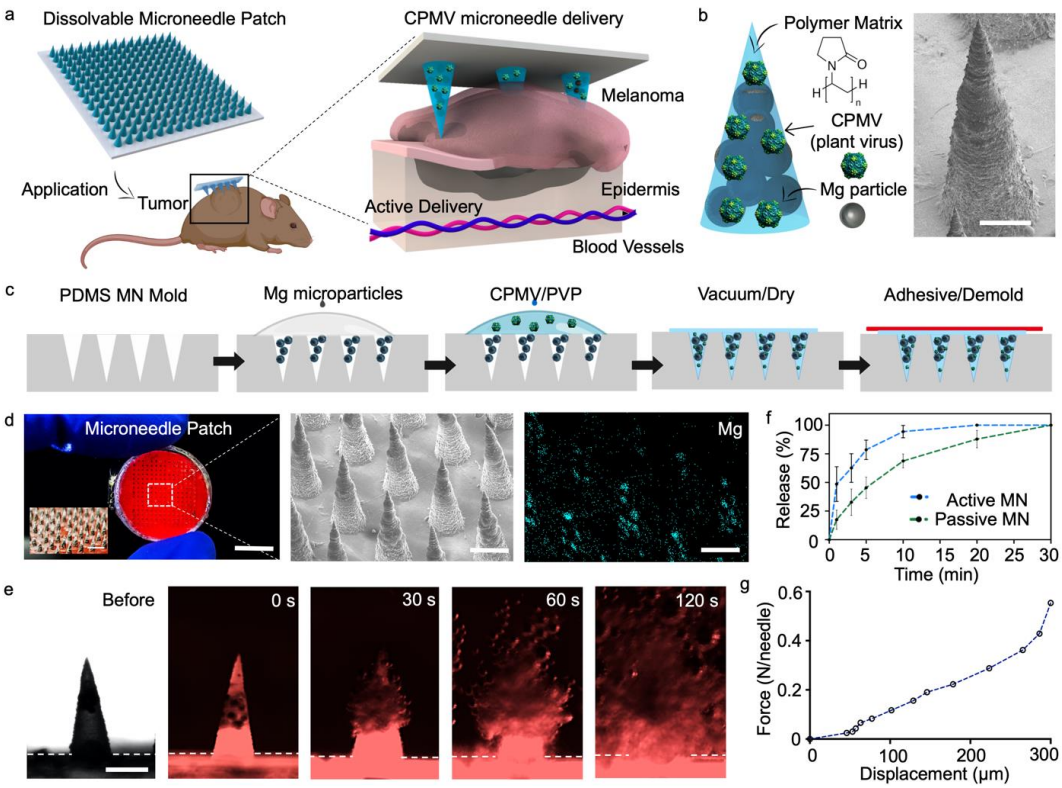

Figure 2.3.1 Formulation of a dissolvable active microneedle patch and corresponding characterization. (a) Schematic illustration of *in situ* vaccination with an autonomous dissolvable active microneedle patch for the treatment of B16F10 melanoma by the release and delivery of plant virus nanoparticles (cowpea mosaic virus, CPMV). (b) Microneedle tip composition and corresponding scanning electron micrograph (SEM). Scale bar, 200 μm. (c) Schematics of fabrication steps for the dissolvable active microneedle array: infiltration of Magnesium (Mg) microparticles onto the negative microneedle features of PDMS mold, polymer and CPMV loading, drying, and demolding. (d) Digital photograph of a dissolvable active microneedle patch comprised of 225 microneedle tips, corresponding SEM image, and Energy Dispersive X-Ray (EDX) elemental analysis of Mg within the active microneedle tips. Scale bars, 5 mm, and 400 μm respectively. (e) Fluorescent microscopy time-frame images of the dissolution of an active microneedle tip, displaying the rapid polymer matrix dissolution and Mg microparticle hydrogen reaction (0, 30, 60 and 120 s intervals). Scale bars, 400 μm. (f) Release kinetics of the delivery of Cy3-conjugated CPMV (Cy3-CPMV) from active and passive microneedles. (g) Mechanical strength analysis of a dissolvable active microneedle array.

PVP has been shown to be extremely biocompatible and highly dissolvable with broad use in a variety of biomedical applications.[38,39]

In brief, the active microneedle patches were fabricated by a micromolding process,[10,22] involving negative polydimethylsiloxane (PDMS) microneedle molds as reusable templates (Figure 2.3.1c). The conical cavities of the negative PDMS molds were infiltrated with Mg microparticles followed by a polymeric blend of PVP and CPMV nanoparticles, thus obtaining the final patch by air drying the molds at room temperature. Once dried, the active microneedle patches were demolded by transferring them to a medical adhesive base and stored at room temperature prior to application. Passive (control) microneedle patches were produced in the same manner, except that the Mg loading step was omitted. microneedle patches were produced under room temperature conditions and without harsh organic solvents to avoid inactivation or modification of the CPMV (detailed fabrication in supporting information). The end-product was a circular patch, a thin polymeric base of ~100 μm in thickness and ~12 mm in diameter, attached to the 15x15 microneedle array (10 mm x 10 mm). The microneedle array size was designed to accommodate the size of the dermal melanomas on the day of treatment. The active microneedle array consisted of 225 conical-shaped CPMV- and Mg-loaded tips, measuring 400 μm in diameter at the base and 850 μm in length, as shown in a digital photograph in Figure 2.3.1d (left panel). Characterization of microneedle array structure included scanning electron microscopy (SEM) and Energy Dispersive X-Ray (EDX) elemental analysis to visualize the structure of the microneedles and the Mg microparticles contained within them.

Prior evaluating the release of CPMV nanoparticles from microneedles *in vitro*, we produced active microneedle patches loaded with Cyanine3 dye (Cy3) conjugated-CPMV (Cy3-CPMV). The Cy3-CPMV was distributed within the microneedle structure and along the base (thin polymeric film ~100 μm in thickness). The Mg microparticles were confined and concentrated within each microneedle tip. We then captured serial brightfield (Nikon Eclipse Instrument Inc. Ti-S/L100) and fluorescence microscopy images (EVOS FL microscope, RFP fluorescent filter) with immersion in phosphate buffered saline (PBS, pH 6.5). Rapid dissolution of the active microneedle tips when immersed in solution with vigorous and spontaneous H_2 bubble generation and Cy3-CPMV release was observed (Figure 2.3.1e). We evaluated and compared the release kinetics and the permeation of Cyanine5 dye (Cy5) conjugated-CPMV (Cy5-CPMV) released by active microneedles to that of passive microneedles. Active microneedle and passive microneedle patches were applied to a phantom tissue model (~3 mm thickness) for different durations and Cy5-CPMV release measured by UV-Visual spectrophotometric technique. The release curve results from the active microneedles (48.6±15.2%) showed an average 3-fold advantage over the passive microneedles (17.4±8.3%) with application for 1 minute. After 5 minutes, the active microneedles (78.5±8.4%) showed a 1.5-time fold enhanced release when compared to passive microneedle (45.3±9.3%).

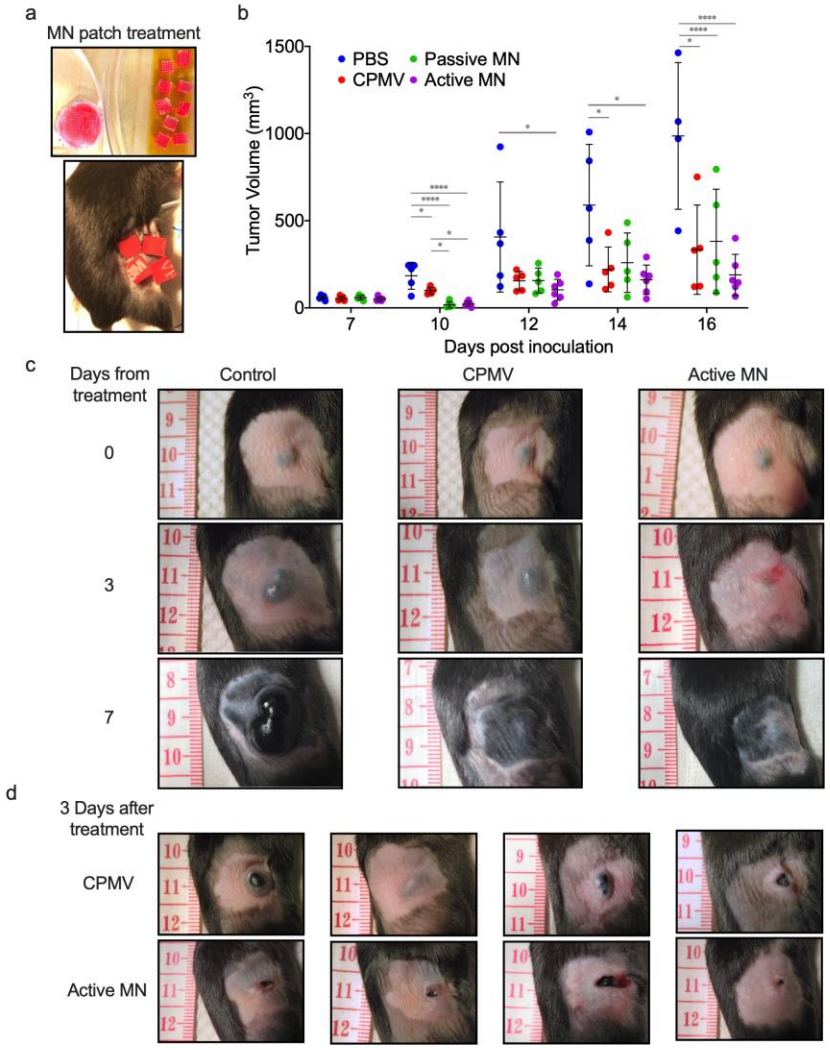

Figure 2.3.2 CPMV *in situ* vaccination administered by active microneedle patches, passive microneedle patches or intratumoral injection in B16F10 dermal melanoma model. (a) Microneedle patches were cut into smaller pieces (total of 4 or 9 pieces equaling full 100 μg CPMV dose) to cover tumor area. (b) Tumor volumes of mice receiving 30 μL PBS injection (PBS, blue), 100 μg in 30 μL CPMV injection (CPMV, red), CPMV passive microneedle (green), and CPMV active microneedle (purple) after treatment administration (on day 7 after intradermal B16F10 melanoma cell inoculation). Data are mean ± standard deviation (SD) (n=5 for all treatment groups except for active microneedle group, n=6). Tumor growth was compared on different time points by one-way ANOVA with Tukey's test: *P<0.05, **P<0.01, ***P<0.001. (c) Clinical appearance of representative PBS-, CPMV injection-, and active microneedle-treated tumors 3 and 7 days after treatment. (d) At day 3 post treatment, CPMV injection-treated tumors vary between exophytic and involuted appearance. Active microneedle treated-tumors more consistently have an involuted appearance.

Finally, the active microneedles delivered the full dose 10 minutes after application while the passive microneedles had released only a partial dose (68.7±6.0%). (Figure 2.3.1f). The active microneedles enhanced and accelerated delivery of Cy5-CPMV relative to that of the passive diffusion-based microneedle patch *in vitro*. Furthermore, microneedles must meet mechanical stability and the strength requirements to breach dermal barriers *in vivo*. An axial mechanical compression test on each microneedle was performed to evaluate its failure force. The mechanical strength results yielded a fracture force of 550 mN per microneedle tip (Figure 2.3.1g), demonstrating that the active microneedles are sufficiently robust to withstand the force necessary for application of the patch to skin.[39]

We first sought to investigate differences in IT delivery of CPMV via conventional needle injection and passive and active transdermal microneedles *in vivo*. Adequate IT distribution and permeation of an immunoadjuvant in large or irregularly shaped tumors with conventional injection can be challenging. In previous reports of CPMV *in situ* vaccination using conventional IT injection for melanoma, multiple injections (2 to 4 injections administered weekly) were needed to induce a durable antitumor response and therapeutic efficacy.[23,27] Dermal melanomas were produced by intradermal injection of B16F10 tumor cells in the right flank of C57BL/6 mice. When tumors reached approximately 40-80 mm^3 in volume, 100 μg CPMV-loaded passive or active microneedles were applied to the cutaneous surface of tumors until the needles completely dissolved (typically for 5-10 minutes). To facilitate patch placement on exophytic or irregular shaped larger tumors, the patches were cut to smaller pieces (4-9

pieces) such that a full dose was administered over the contours of the mass with greater coverage of the tumor (Figure 2.3.2a). Control mice were intratumorally injected with either PBS (30 μL) or CPMV (100 μg/30 μL PBS). All animals received a single treatment administration.

CPMV showed potency when administered intratumorally via injection or microneedle patches. Greater tumor regression was observed in the passive and active microneedle -treated groups compared to injected CPMV-treated groups within the first three days post treatment. Injected CPMV did not lead to tumor regression in this time period, but rather appeared to slow progression relative to the PBS injection. Over the next 7 days, tumor progression was delayed the most in the active microneedle group, and progression was observed earlier in the CPMV and passive microneedle groups (Figure 2.3.2b and c). Furthermore, treatment with active microneedle patches appears to result in a more consistent clinical appearance of tumors. Physical examination of tumors 3 days after treatment, demonstrated that all melanomas treated with active microneedle patches had an involuted appearance and were flattened on palpation. In contrast, the appearance of tumors treated with CPMV injection varied from involuted to exophytic and on palpation varied from firm, rounded masses to a flattened center encircled by rim of firm tissue (Figure 2.3.2d). These tumor changes observed within 7 days of treatment have previously been related to changes in the TME and infiltrating innate immune cells responding directly to the presence of CPMV within the tumor.[23,25-27] Hence, these findings suggest more uniformity in the delivery of CPMV with the active microneedle

patches than with conventional injection, leading to consistent innate immune system-mediated antitumor effects.

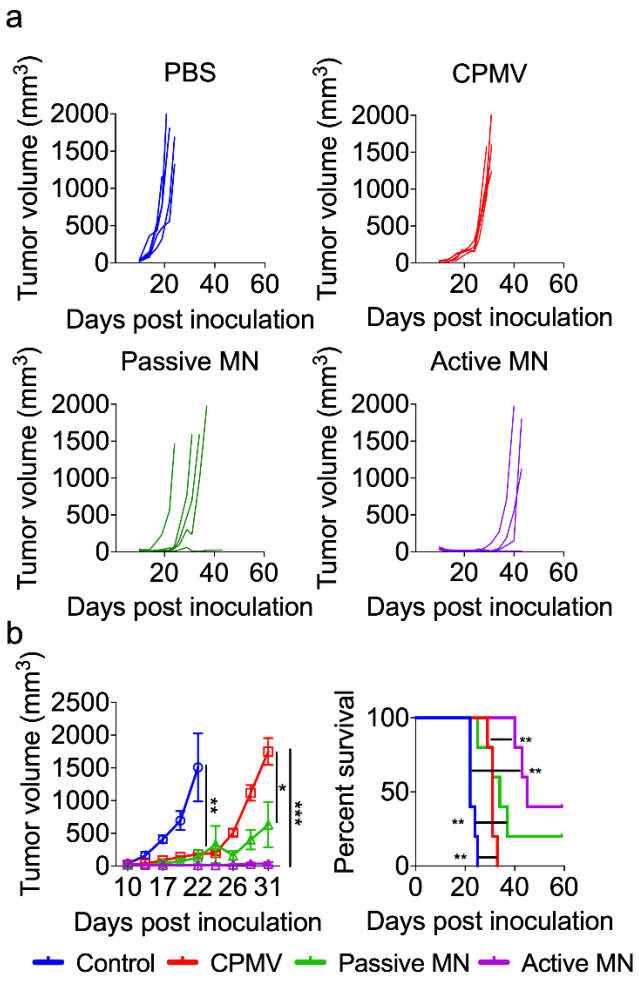

Figure 2.3.3 Tumor growth suppression and survival with CPMV *in situ* vaccination administered by active microneedle, passive microneedle, and intratumoral injection in B16F10 dermal melanoma model. Tumor volumes growth curve of individual mice (a) and averaged tumor volumes of mice (b, *left panel*) receiving PBS (blue), CPMV injection (red), CPMV passive microneedle (green), and CPMV active microneedle (purple). Data are means ± SEM (n=5). Tumor growth was compared on different time points by one-way ANOVA with Tukey's test: *P<0.05, **P<0.01, ***P<0.001. (b, *right panel*) Survival rates. Statistical significance was calculated using Log-rank (Mantel-Cox) test: **P<0.01.

While we observed that the process of administering treatment with active microneedles led to greater and more reliable tumor regression, we also observed improvement in overall efficacy with a single treatment. When B16F10 melanomas reached approximately 25-30 mm^3 in volume, 100 μg CPMV-loaded passive or active microneedle patches were applied to the tumors. Control mice were intratumorally injected with either PBS (30 μL) or CPMV (100 μg/30 μL PBS). The tumors were small and flat, permitting treatment without cutting the microneedle patches.

The growth rate of the tumors was measured over time (Figure 2.3.3a). As shown in the left panel of Figure 2.3.3b, IT injection of CPMV delayed tumor growth compared to PBS treated animals (median tumor volumes in mm^3 (interquartile range), PBS: 1315 (623.3-2582), CPMV: 180.9 (160.6-201.6), $p<0.01$ on day 22)). However, all mice treated with CPMV injection had appreciable tumor growth after day 26 and were euthanized by day 31. CPMV-loaded passive microneedle patches caused further delay in tumor progression compared to injected CPMV (Passive microneedle: 464.4 (68.5-1364), CPMV: 1826 (1328-2095), $p<0.05$ on day 31). Mice treated with CPMV-loaded active microneedle patches had substantial suppression of tumor growth relative to those treated with CPMV injection (Active microneedle: 14.5 (9.1-68.6), $p<0.001$ on day 31, Figure 2.3.3b, left panel). With respect to survival, passive microneedle patches slightly improved the overall survival of mice, without a significant difference in median survival compared to CPMV injection (injected CPMV: 31 days vs passive microneedle: 34 days). Moreover, 40% of the active microneedle -treated mice demonstrated durable survival with complete tumor rejection and prolongation of median survival to 45 days (Figure

2.3.3b, right panel). Administration of CPMV in active microneedle patches led to enhanced early tumor regression, delayed tumor progression, and increased overall survival after a single administration. This level of efficacy has been observed for CPMV administered via injection, however, it requires multiple treatments.[23,27]

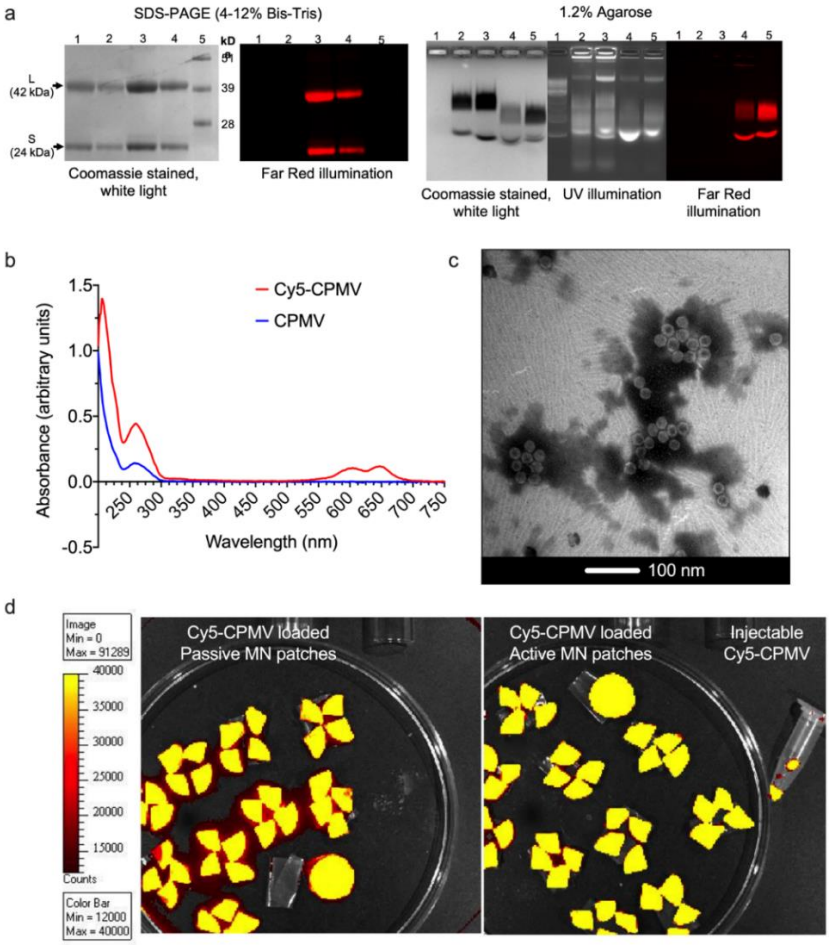

Figure 2.3.4 Cy5-CPMV loaded active and passive microneedle characterization. (a) Gel analysis of CPMV and Cy5-CPMV. Denaturing (SDS-PAGE, *left*) gel: 1: CPMV (10 μg), 2: CPMV (5 μg), 3: Cy5-CPMV (10 μg), 4: Cy5-CPMV (5 μg), Lane 5: ladder. Native (1.2% agarose, *right*) gel: 1: 1kb DNA ladder, 2: CPMV (5 μg), 3: CPMV (10 μg), 4: Cy5-CPMV (5 μg), 5: Cy5-CPMV (10 μg). (b) UV-visual spectral analysis of CPMV and Cy5-CPMV, with absorbance peak at 647 nm in Cy5-CPMV. (c) Transmission electron microscopy of Cy5-CPMV (0.1 mg/ml). (d) Fluorescence imaging of Cy5-CPMV loaded active microneedle, passive microneedle, and injectate.

We next sought to examine whether differences in distribution of CPMV released *in vivo* from active and passive microneedles compared to IT injection may underlie differences in efficacy. Cy5-CPMV was employed to allow fluorescence imaging of CPMV nanoparticles (Figure 2.3.4).

As previously described, mice were B16F10 melanoma isografts were inoculated and Cy5-CPMV was administered to the resulting tumors (at volumes 60-100 mm3). For *in vivo* imaging, mice received 100 µg of intratumorally injected Cy5-CPMV, 100 µg of passive microneedle patch-administered Cy5-CPMV, or 100 µg of active microneedle patch-administered Cy5-CPMV. Tumors were imaged (IVIS Xenogen 200, Cy5.5 filter with excitation/emission range 615-665 nm/695-770 nm) serially to monitor CPMV release and retention at treatment site over time.

Injection of CPMV resulted in high levels of fluorescence at the tumor site that gradually decayed over time. As demonstrated in representative images (Figure 2.3.5a), the fluorescence signal was not evenly distributed throughout the tumor, but rather with peaks of fluorescence within regions of the tumor. This suggested that CPMV was accumulating in various regions of the tumor, consistent with the heterogeneous structure of tumors and physical barriers with in the TME. Densely packed tumor cells and extracellular matrix structures may slow the rate of, or even impede passive diffusion of CPMV throughout the tumor. For the active- and passive- microneedle treated tumors, the overall fluorescent signal detected was low and not significantly different from each other, or the PBS group. The early tumor regression was still observed in these animals suggesting that the enclosed Cy5-CPMV was in fact released within these tumors.

Figure 2.3.5 *In vivo* and *ex vivo* imaging of Cy5-conjugated CPMV (Cy5-CPMV) *in situ* vaccination of B16F10 melanomas administered by active microneedle, passive microneedle, and intratumoral injection. (a) Representative time course of *in vivo* fluorescence imaging of B16F10 melanomas treated with PBS injection, Cy5-CPMV injection, Cy5-CPMV passive microneedle, or Cy5-CPMV active microneedle. Colors denote radiant efficiency ((p/sec/cm^2/sr)/(μW/cm^2)) of Cy5-CPMVfluorescence. (b) Quantification (average radiant efficiency) of Cy5-CPMV fluorescence in tumor ROI *in vivo* at different timepoints after treatment with PBS (blue circle, n=4), Cy5-CPMV injection (red square, n=5), Cy5-CPMV passive microneedle (green upward-pointing triangle, n=7), or Cy5-CPMV active microneedle (purple downward-pointing triangle, n=7). Data are medians ± interquartile range. No significant differences in radiant efficiency were observed in Active microneedle vs. Passive microneedle and CPMV vs. Passive microneedle at any timepoints. Tumor growth was compared on different time points by Kruskal-Wallis one-way ANOVA with Dunn's multiple comparisons correction: *P<0.05, **P<0.01, ***P<0.001. (c) Immunofluorescence of tumors 24 hours after treatment (blue: nucleus, pink: blood vessels, green: leukocytes, yellow: Cy5-CPMV, arrow: Cy5-CPMV, *: blood vessel, dashed circle: leukocyte). *Abbreviations: BL, baseline; p, photon; sr, steradian; W, watt)*

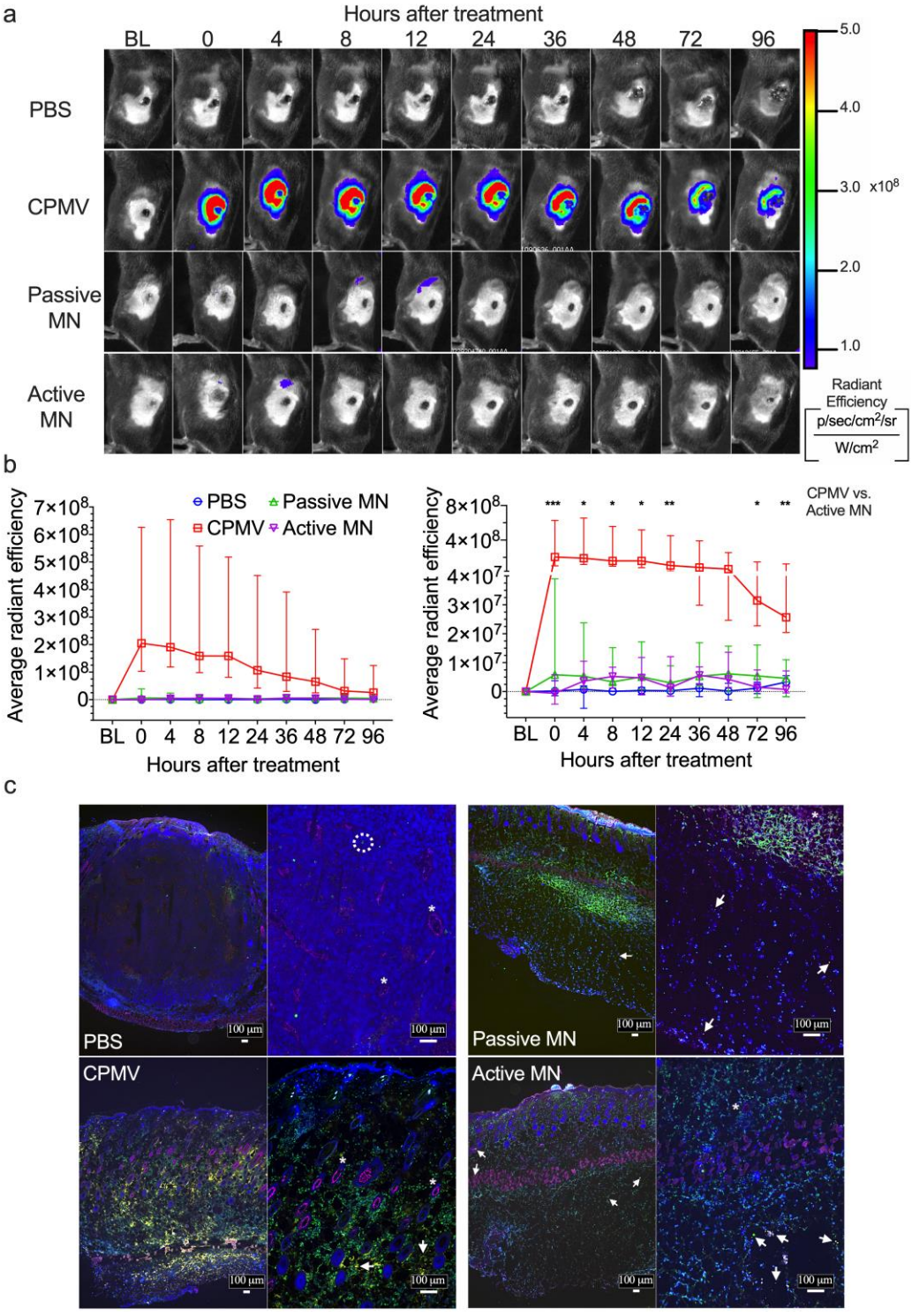
a
Hours after treatment
BL 0 4 8 12 24 36 48 72 96
PBS
CPMV
Passive MN
Active MN
5.0
4.0
3.0 x10^8
2.0
1.0
Radiant Efficiency
p/sec/cm2/sr
W/cm2
b
Average radiant efficiency
PBS
Passive MN
CPMV
Active MN
Hours after treatment
CPMV vs. Active MN
c
PBS
CPMV
Passive MN
Active MN
100 µm

Some animals showed transient increase in signal in regions just inferior to the tumors, related to the tissue under the tumor into which the microneedles were pressed/localized during applications (Figure 2.3.5a). The low fluorescence signal could result from the 100 μg Cy5-CPMV dose being spatially distributed over a larger area within the microneedles, and even further dispersed with the active microneedles. The Cy5-CPMV signal of the more thinly dispersed particles may have been below the detection limit of the imaging system.

To further visualize the IT distribution of Cy5-CPMV, we employed *ex vivo* immunohistofluorescence of *in vivo* treated tumors. B16F10 melanomas were generated and treated, as described above. Animals were euthanized and tumors resected en bloc and flash frozen in OCT at 24 h post treatment. Tumor sections were stained for blood vessels (CD31/PECAM-1), leukocytes (CD45), and cell nuclei (DAPI).

Immunofluorescence of PBS treated tumor showed a vascular tumor with rare leukocytes. The Cy5-CPMV injection-treated tumor demonstrated uneven distribution of CPMV, with areas of greater Cy5-CPMV clustering seen as bright yellow regions at low power and high power (4x and 10x magnification, respectively). For the active and passive microneedle-treated tumors, Cy5-CPMV was observed to be less clustered within the tissues, bright yellow regions are not visible at low power. While at high power, discrete yellow puncta of Cy5-CPMV were observed.

Table 2.3.1 Surface markers of each particular cell type

cell types	full name	Phenotype
CD45	Leukocytes	$CD45^+$
NOS monocytic cells	Not otherwise specified monocytic cells	$CD45^+CD11b^+$ $Ly6G^-$
NOS granulocytic cells	Not otherwise specified granulocytic cells	$CD45^+CD11b^+$ $Ly6G^+$
G-MDSCs	Granulocytic myeloid-derived suppressive cells	$CD45^+CD11b^+Ly6G^+$ $Ly6C^-MHCII^-CD86^-$
M-MDSCs	Monocytic myeloid-derived suppressive cells	$CD45^+CD11b^+Ly6G^-Ly6C^+MHCII^-$SSClow
TINs	Tumor-infiltrating neutrophils	$CD45^+CD11b^+Ly6G^+MHCII^+CD86^+$
QNs	Quiescent neutrophils	$CD45^+CD11b^-Ly6G^+$
Activated DCs	Activated dendritic cells	$CD45^+CD11b^+CD11c^+MHCII^+CD86^+$
Inactive DCs	Inactive dendritic cells	$CD45^+CD11b^+CD11c^+MHCII^-CD86^+$, $CD45^+CD11b^+CD11c^+MHCII^+CD86^-$, or $CD45^+CD11b^+CD11c^+MHCII^-CD86^-$
NK cells	Natural killer cells	$CD45^+CD11b^+NK1.1^+Ly6G^-Ly6C^-$ $F4/80^-$
M1 macrophages	Type 1 tumor-associated macrophages	$CD45^+CD11b^+F4/80^+Ly6G^-Ly6C^-MHCII^+CD86^+$
M2 macrophages	Type 2 tumor-associated macrophages	$CD45^+CD11b^+F4/80^+Ly6G^-Ly6C^-MHCII^-CD86^-$
NOS TAMs	Not otherwise specified tumor-associated macrophages	$CD45^+CD11b^+F4/80^+Ly6G^-Ly6C^-MHCII^+CD86^-$, or $CD45^+CD11b^+F4/80^+Ly6G^-Ly6C^-MHCII^-CD86^+$

Reduced clustering of Cy5-CPMV nanoparticles administered via microneedles, would be consistent with the low fluorescence signal detected in the *in vivo* fluorescence microscopy images. Interestingly, we observed widespread CD45 staining, indicating leukocyte infiltration of Cy5-CPMV treated tumors (Figure 2.3.5b). These early

infiltrating immune cells are critical mediators of *in situ* vaccination efficacy.[23,27] We next aimed to further characterize this early immune response.

To investigate the early cellular innate immune response within the TME and its kinetics after treatment, we analyzed the cellular immune infiltration of treated tumors by flow cytometry at 4 and 24 h after either IT injection, passive microneedle, or active microneedle patch application. Intradermal B16F10 melanoma tumors on the flank were treated when tumor volume reached 60 mm^3. At 4 h or 24 h after treatment, tumors were harvested and stained for flow cytometry analysis (markers listed in methods section, Table 2.3.1). At 4 h following treatment, B16F10 melanomas treated with CPMV regardless of delivery method demonstrated increases in the percentage of IT $CD45^+$ cells relative to that of PBS-treated tumors. The percent increase in tumors treated by CPMV injection was largest at 4 h, but only transient. By 24 h after treatment, the percentage of $CD45^+$ cells in the CPMV injection-treated tumors had decreased below that of active microneedle- and passive microneedle-treated tumors but was still significantly increased relative to the PBS-treated tumors. Active microneedle- and passive microneedle-treated tumors demonstrated a steady elevation in percentage of $CD45^+$ cells at 4 h and 24 h relative to PBS-treated tumors (Figure 2.3.6a).

Figure 2.3.6 Intratumoral innate immune cell profile following CPMV microneedle administration. C57BL/6 mice bearing dermal B16F10 tumors (60 mm^3) were treated with CPMV by intratumoral injection, passive microneedle, or active microneedle. Four hours and 24 hours following treatment, the tumors were harvested to quantify innate immune cell infiltration by flow cytometry. (a) Percentage of total cells analyzed that were $CD45^+$ at 4 hours (*left*) and 24 hours (*right*) after treatment. (b) Innate immune tumor infiltrate profiles (% of $CD45^+$ cells) at 4 hours (*left column*) and 24 hours (*right column*). Data are mean percent (n=3). (c-h) Percentages of intratumoral $CD45^+$ cells consisting of activated dendritic cells (DCs, c), type 1 tumor associated macrophages (M1 macrophages, d), type 2 tumor associated macrophages (M2 macrophages, e), granulocytic myeloid-derived suppressive cells (G-MDSCs, f), monocytic-myeloid derived suppressive cells (M-MDSCs, g), and natural killer cells (NK cells, h). Data are means ± SD (n=3). Statistical significance was calculated using two-way ANOVA (Treatment type vs. Time) with Sidak's multiple comparisons post-test: *P<0.05, **P<0.01, ***P<0.001, ****P<0.0001.

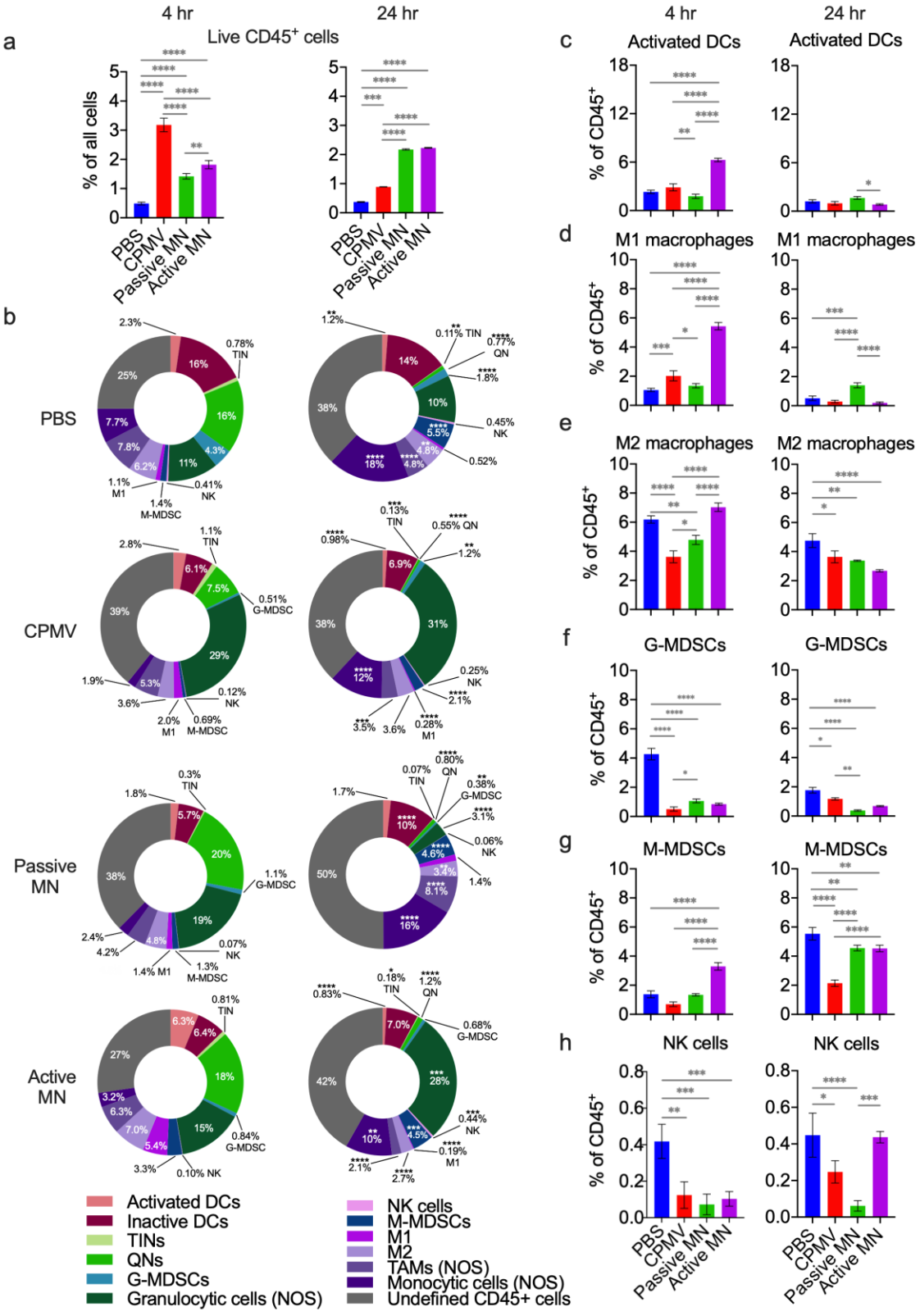
a
4 hr
24 hr
Live CD45+ cells
% of all cells
PBS
CPMV
Passive MN
Active MN
b
PBS
CPMV
Passive MN
Active MN
Activated DCs
Inactive DCs
TINs
QNs
G-MDSCs
Granulocytic cells (NOS)
NK cells
M-MDSCs
M1
M2
TAMs (NOS)
Monocytic cells (NOS)
Undefined CD45+ cells
c
Activated DCs
d
M1 macrophages
e
M2 macrophages
f
G-MDSCs
g
M-MDSCs
h
NK cells
% of CD45+

Examination of the subpopulations of $CD45^+$ cells demonstrated distinctive changes in the IT $CD45^+$ immune cell profile at 4 h and 24 h after treatment with different delivery systems (Figure 2.3.6b). Activated dendritic cells (DCs, $CD11b^+CD11c^+MHCII^+CD86^+$) comprised a greater percentage of the $CD45^+$ cell population in active microneedle-treated tumors than that of any other treatment group at 4 h. The passive microneedle patches and CPMV injection-treated tumors had similar percentages of activated DCs as the PBS injection-treated tumors (Figure 2.3.6c, left panel).

Notably, the percentage of activated DCs decreased more than 6-fold by 24 h after treatment in the active microneedle-treated tumors. Between 4 h and 24 h after treatment, the activated DC percentages decreased in the PBS-treated (1.9-fold) and CPMV injection-treated (2.9-fold) tumors (Figure 2.3.6c, right panel). Activated DCs play a critical role in transporting antigens towards draining lymph nodes and lymphoid organs, as well as responsible of performing antigen presentation to prime subsequent adaptive immune responses. The active microneedle-treated tumors appeared to have greater recruitment of activated DCs at 4 h after treatment. The decrease at 24 h could represent the migration of these DCs to draining lymph nodes to present collected TAAs. Studies of DC migration from skin have demonstrated migration occurring over 1-3 days following immunogenic stimulation of the skin.[40-42]

The monocytic component ($CD11b^+$ $Ly6G^-$) of the $CD45^+$ cell population exhibited complex, dynamic changes after the different methods of CPMV administration. The monocytic component included Type 1 tumor-associated macrophages (M1s,

$CD11b^+F4/80^+Ly6G^-Ly6C^-MHCII^+CD86^+$), Type 2 tumor-associated macrophages (M2s, $CD11b^+F4/80^+Ly6G^-Ly6C^-MHCII^-CD86^-$), tumor-associated macrophages not otherwise specified (TAMs NOS, $CD11b^+F4/80^+Ly6G^-Ly6C^-MHCII^+CD86^-$ and $MHCII^-CD86^+$), natural killer cells (NK cells, $CD11b^+NK1.1^+Ly6G^-Ly6C^-$ $F4/80^-$), monocytic-myeloid derived suppressive cells (M-MDSCs, $CD11b^+Ly6G^-Ly6C^+MHCII^-$SSClow), and monocytic cells, whose phenotype was not further specified (monocytic cells not otherwise specified (NOS, $CD11b^+$ $Ly6G^-$ that were not designated as M1, M2, TAMs NOS, NK, or M-MDSCs). The immune response observed in active microneedle-treated tumors maintained a similar level of the monocytic component ($CD11b^+$ $Ly6G^-$) of the $CD45^+$ cell population relative to the PBS-treated tumors at 4 h post-treatment, while the levels in CPMV-injected and passive microneedle-treated tumors were relatively suppressed. Interestingly, while PBS-treated tumors and active microneedle-treated tumors had similar percentages of monocytic cells comprising the $CD45^+$ population, within this component, the active microneedle-treated tumors had greater percentages of M1s and M-MDSCs than the PBS-treated tumors. The M1 percentage of active microneedle-treated tumors was also significantly greater than that of CPMV injection-treated or passive microneedle-treated tumors (Figure 2.3.6b, d, and g, left panels). The percentages of M2s were comparable between the PBS and active microneedle-treated tumors but were lower in the CPMV injection- and passive microneedle-treated tumors at 4 h (Figure 2.3.6e, left panel). The NK cell percentage was suppressed at similar levels in all CPMV-treated tumors at 4 h, relative to the PBS-treated tumors (Figure 2.3.6h, left panel). The early increase in the monocytic component of the immune response in the

active microneedle-treated tumors seems to be driven by increases in the percentages of M1s, M-MDSCs, and monocytic cells NOS.

By the 24 h timepoint, the percentage of the monocytic component in PBS-injected tumors continued to increase. The monocytic component in the active microneedle-treated tumors decreased and CPMV injected-tumors increased until both reached comparable levels. The percentage in the passive microneedle-treated tumors increased to a similar level as that of the PBS-treated tumors (Figure 2.3.6b, right panel). The M1 percentage decreased in all groups, except for the passive microneedle-treated group, which did not change from the 4 h level (Figure 2.3.6f, right panel). The M2 percentage decreased, relative to PBS-treated tumors, in all CPMV-treated groups at 24 h (Figure 2.3.6e, right panel). The percentage of M-MDSCs increased in all groups at 24 h after treatment, with the PBS-treated group having the largest percentage of M-MDSCs and the CPMV injection-treated group having the lowest M-MDSC percentage of all groups (Figure 2.3.6g, right panel). The tumors treated with active microneedles recovered the NK cell percentage to the level of the PBS-treated tumors at 24 h, while this level remained suppressed among the CPMV injection- and passive microneedle-treated tumors (Figure 5h, right panel).

The monocytic component consists of a mix of cells, including macrophages, monocytes, and M-MDSCs. Macrophages can exist in different functional states depending upon their surrounding environment. M1 macrophages promote a pro-inflammatory state and have antitumor activity. M2 macrophages promote tumor growth and progression.[43] Several, sometimes conflicting, roles have been attributed to M-

MDSCs. They are immunosuppressive and support tumor progression. However, there is evidence that they can also differentiate into different types of macrophages and DCs. The fate of these cells is at least partially influenced by the state of the surrounding TME.[44-46] The early increase in M-MDSC percentage in the active microneedle-treated tumor could represent an increased pool of potential macrophages and DCs and would be consistent with the increased percentage of active DCs and M1s, as well as M2s. Although at 4 h, the PBS-treated tumors had similar levels of M2s as the active microneedle-treated tumors, they also contained a reduced percentage of M-MDSCs, so these could have arisen from a different source or developmental pathway in the PBS-treated mice. Further, the monocytic cells NOS component represents a heterogeneous mix of monocytic cells, which include monocytes that also can differentiate into M1s or M2s. Macrophages have long life spans and enhanced phagocytic capacity, especially compared to that of neutrophils. Macrophages have been implicated as critical mediators of tumor regression through direct tumoricidal activity.[47-49] The increased percentages of differentiated M1s, potential macrophage progenitors, and greater recovery of NK cells in active microneedle-treated tumors suggest a greater portion of the $CD45^+$ infiltrate may be comprised of cells with pronounced ability to destroy tumor cells. This could underlie the augmented tumor regression observed in the tumors treated with active microneedles. Passive microneedle-treated tumors appeared to have a delayed expansion of the monocytic cells NOS and M-MDSCs, but not M1 macrophages, at the 24 h timepoint. CPMV injection-treated tumors exhibited a more modest increase in its M1 percentage

and NK cell recovery. Both CPMV injection and passive microneedle administration demonstrated inferior suppression of tumor growth (Figure 2.3.2b-d).

With respect to granulocytic cell ($CD11b^+$ $Ly6G^+$) and quiescent neutrophil (QN, $CD45^+CD11b^-Ly6G^+$) components of the $CD45^+$ infiltrate, dynamic changes in these subsets were also observed. The percentage of broadly granulocytic cells within CPMV injection-treated tumors expanded, compared to that of the PBS-treated tumors, and remained consistent at 4 h and 24 h after treatment (Figure 2.3.6b).

These cells included tumor infiltrating neutrophils (TINs, $CD11b^+Ly6G^+MHCII^+CD86^+$), granulocytic myeloid-derived suppressive cells (G-MDSCs, $CD11b^+Ly6G^+Ly6C^-MHCII^-CD86$), and those whose phenotype was not further specified (granulocytic cells not otherwise specified (NOS), $CD11b^+$ $Ly6G^+$ cells that were not designated as TINs or G-MDSCs). The TIN percentage did not differ from PBS-treated tumor levels in any groups at 4 h and 24 h after treatment (Figure 2.3.7b). Additionally, the quiescent neutrophil (QN, $CD45^+CD11b^-Ly6G^+$) percentage was suppressed in CPMV injection-treated tumors relative to PBS, passive microneedle- and active microneedle-treated tumors at 4 h (Figure 2.3.7c, left panel).

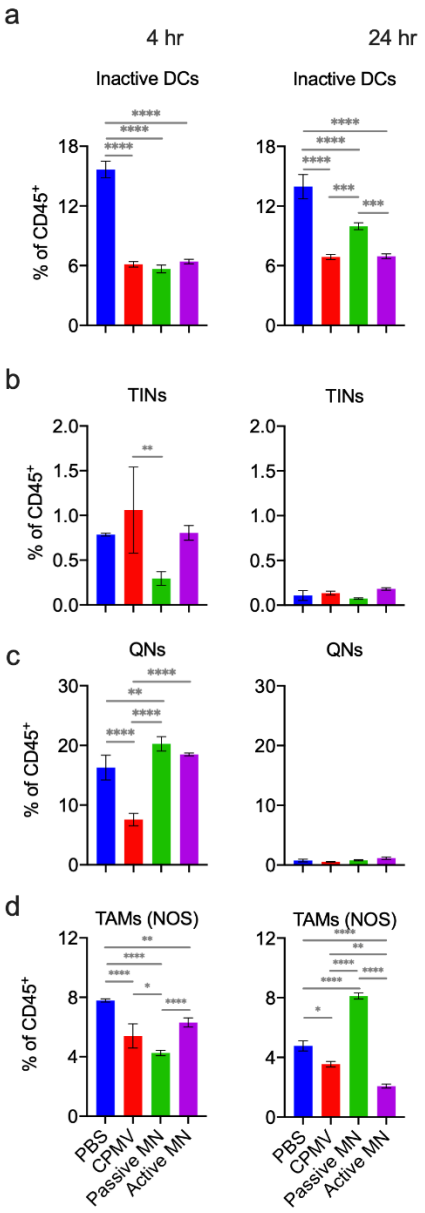

Figure 2.3.7 Intratumoral innate immune cell profile following CPMV microneedle administration. (a-d) Percentages of intratumoral $CD45^+$ cells consisting of inactive dendritic cells (DCs, a), tumor-infiltrated neutrophils (TINs, b), quiescent neutrophils (QNs, c), and tumor-associated macrophages not otherwise specified (TAMs NOS, d) within the $CD45^+$ leukocytes from samples harvested 4 h after treatment (*left)* and from samples harvested 24 h after treatment (*right)*. Data are means ± SD (n=3). Statistical significance was calculated using two-way ANOVA (Treatment type vs. Time) with Sidak's multiple comparisons post-test: *P<0.05, **P<0.01, ***P<0.001, ****P<0.0001.

The granulocytic cell percentage in active microneedle-treated tumors increased to a level comparable to that in the CPMV injection-treated tumors by 24 h, while the granulocytic component decreased in the passive microneedle-treated tumors (Figure 2.3.6b, right panel). This overall increase within the active microneedle-treated tumors was related to the higher percentage of granulocytic cells NOS within the tumors, while the G-MDSC percentage was decreased in all CPMV-treated tumors, relative to PBS-treated tumors at 4 h and 24 h after treatment (Figure 2.3.6b and f). The percentage of quiescent neutrophils decreased to a similar level in all groups by 24 h (Figure 2.3.6b and Figure 2.3.7c, right panels). CPMV injection-treated tumors exhibited a more pronounced increase of the granulocytic cell NOS component. Granulocytic cells NOS is also a heterogenous mix of cell types, including activated neutrophils. Previous studies have demonstrated that injection of CPMV for *in situ* vaccination led to increases in the percentages of activated neutrophils and TINs, with suppression of QNs within the first 24 h of treatment.[23-27] Thus, the observed increase in the CPMV injection-treated tumors is consistent with previous reports. The slower increase in the granulocytic component of the immune cell response over 24 h, with a greater percentage of monocytic cells, notably NK cells and M1s, which possess well-known tumoricidal functionality, following active microneedle treatment represents a difference from injection.

The heightened efficacy and immune responses using the active microneedle-based CPMV administration may be related to differences in the kinetics of CPMV delivery. Another possibility to consider is the potential actions of the Mg micromotors themselves. Mg^{2+} is an important second messenger and has been implicated in T cell

stimulation in response to antigens,[50,51] macrophage development,[52] M1/M2 polarization,[53] and DC migration.[52] These *in vitro* studies examined substantially higher extracellular Mg^{2+} concentrations (approximately 6 times greater) than the maximum possible concentration of Mg released from the active microneedle patch into the smallest volume (25 mm^3) tumor in this study. While Mg^{2+} at higher concentrations plays an important role in T cell activation, it is unlikely that Mg^{2+} would reach distant lymphoid structures at concentrations relevant to $CD8^+$ T cell activation *in vivo*. The relatively low Mg^{2+} concentration within the tumor and washout over time, would likely limit Mg^{2+}contribution to the overall enhancement of immune responses beyond small, short-lived effects. Moreover, in our previous report, active microneedle patches devoid of any payload therapeutic (blank microneedles) did not demonstrate antitumor efficacy, as durable tumor growth suppression and overall survival in blank microneedle-treated mice did not differ significantly from those treated with PBS injection.[22]

Overall, these results demonstrated that CPMV *in situ* vaccination via active microneedles promoted enhanced IT recruitment and activation of APCs, including DCs and macrophages. The enhanced infiltration of macrophages is also consistent with the pronounced early tumor regression. Passive microneedles, however, seemed to lack enhancement of activated DCs and M1s, with a delayed infiltration of other monocytic cells. We next sought to determine whether early enhancement of APC tumor infiltration could also lead to an enhanced antitumor adaptive immune response.

In situ vaccination optimally results in induction of a systemic antitumor response mediated by the adaptive immune system. Local innate immune activation is critical for

priming these adaptive immune responses. To determine whether the remodeling of the TME and rapid infiltration of APCs by active microneedle treatment could effectively launch and improve the systemic antitumor response of $CD8^+$ T cells, an interferon-γ (IFN-γ) release assay with splenocytes from treated mice was performed. $CD8^+$ T cells producing IFN-γ indicates activation of the cells in response to recognition of their target antigen.[54,55] B16F10 melanomas were treated when volumes reached 60 mm^3. Splenocytes were isolated 10 days after treatment with PBS, CPMV injection, passive microneedle, or active microneedle as described above. The splenocytes were incubated with B16F10 melanoma cell lysate, CPMV, or culture media only in a suspension culture for 48 h. After this period, IFN-γ-producing effector $CD8^+$ T cells ($CD44^{hi}IFN\text{-}\gamma^+CD8^+$) frequency was evaluated using flow cytometry.

As shown in Figure 2.3.8, co-incubation of B16F10 melanoma cell lysate with splenocytes from mice treated with CPMV injection, passive microneedle, and active microneedle exhibited increased antigen-specific CTL activity. The active microneedle treatment group showed the greatest percentage increase of IFN-γ-producing effector $CD8^+$ T cell ($p<0.0001$ vs. other treatment groups) after B16F10 melanoma cell lysate exposure. Incubation of splenocytes from mice treated with CPMV via passive and active microneedles with CPMV increased the frequency of activated effector $CD8^+$ T cells by 2.11-fold (vs. PBS, $p<0.0001$) and 2.57-fold (vs. PBS, $p<0.0001$), respectively compared to CPMV injection-treated mice. Splenocytes from mice treated with CPMV injection incubated in media alone demonstrated no change in $CD8^+$ T cell population compared to

PBS-treated group. In contrast, a 1.5-fold increase of effector $CD8^+$ T cell population was shown in both passive microneedle- and active microneedle-treated mice.

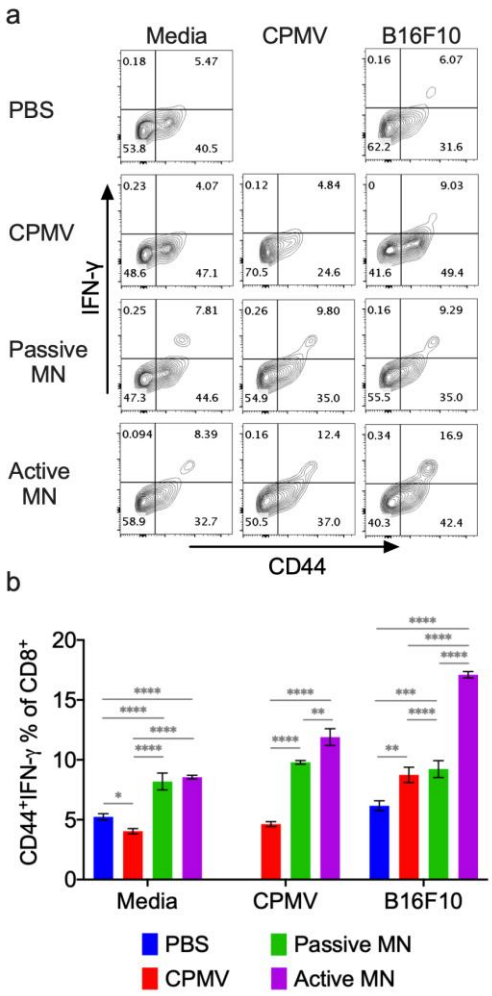

Figure 2.3.8 Systemic anti-tumor immune response following CPMV microneedle administration. C57BL/6 mice bearing dermal B16F10 tumors (60 mm^3) were treated with CPMV by intratumoral injection, passive microneedle, or active microneedle 10 days after B16F10 cell inoculation. 10 days following the treatment, spleens were harvested and co-cultured with media, 10 μg CPMV, or B16F10 tumor cell lysate for 48 h. Intracellular IFN-γ was measured in $CD8^+$ T cells by flow cytometry. (a) Representative flow cytometry plots of $CD44^{hi}IFN\text{-}\gamma^+CD8^+$ T cells in each re-stimulation group. . (b) The percentage of $CD44^{hi}IFN\text{-}\gamma^+CD8^+$ T cells after gating $CD8^+$ T cells. Data are means ± SD (n=3). Statistical significance was calculated using one-way ANOVA with Tukey's multiple comparisons post-test: **P<0.05, **P<0.01, ***P<0.001, ****P<0.0001.

Larger percentage of $CD8^+$ T cells producing IFN-γ is associated with enhanced antigen priming and presentation by APCs[56,57], as well as greater suppression of tumor growth in other cancer vaccination strategies.[26,57,58] CPMV treatment with active microneedles promotes activation of a larger percentage of the $CD8^+$ splenocyte population by CPMV or the targeted tumor. Increased APC cross presentation of CPMV antigens and TAAs with active microneedle treatment may mediate the heightened $CD8^+$ T cell activation. Broader distribution of CPMV within the heterogenous tumor, with active microneedle administration, may also lead to APC collection and cross presentation of a more diverse array of TAAs in the lymphoid organs. In turn, this may induce activation of a broader subset of antitumor $CD8^+$ T cells This finding supports the previous hypothesis that rapid, augmented APC infiltration into the TME with active microneedle-mediated CPMV delivery (Figure 2.3.2c and d), could lead to a more potent systemic antitumor response than that following CPMV injection. We also find that treatment with active or passive microneedles led to an expansion in the percentage of activated $CD8^+$ splenocytes, even in the absence of B16F10 cell or CPMV exposure. These cells could represent enrichment in the $CD8^+$ T cell population recognizing antigens within the culture conditions alone. This suggests that the process of *in situ* vaccination with microneedles may generally enhance $CD8^+$ T cell activation.

2.3.4 Conclusions

Cancer immunotherapy aims to enable the host immune system to eliminate tumors. Establishing a broad tumor-targeting T cell repertoire, which can recognize and destroy

heterogeneous tumor cell populations, is among the primary objectives of this treatment strategy. *In situ* vaccination uses the diverse collection of TAAs within the tumor to prime an enhanced, durable, and selective adaptive immune response. *In situ* vaccination also induces reprogramming of the TME toward an immunostimulatory state. However, conventional needle injection-based *in situ* vaccination requires direct IT application of immunoadjuvants within solid cutaneous tumors. Injection of solid tumors presents obstacles to optimizing treatment efficacy, such as the elevated tumor IFP.[11,12,59] To overcome these challenges, transdermal delivery platforms are being widely investigated. Most current transdermal patches release payload drugs in a passive, diffusion-based manner.[60,61] These type of microneedle transdermal patches have been explored for the delivery of nucleic acid- or antigen-based vaccines within the dermis,[5-8] IT immune checkpoint inhibitors,[9,10] and IT chemotherapy.[1-4] Previously, the autonomous active microneedle patch application improved payload penetration and distribution within tissues. When loaded with an immune checkpoint inhibitor, anti-CTLA-4 antibody, active microneedle administration led to improved antitumor efficacy against B16F10 melanoma compared to IT injection.[22]

In this study, microneedles containing Mg microparticles were used to actively deliver nanoparticles, specifically the plant viral nanoparticles, CPMV, for *in situ* vaccination against the B16F10 model of melanoma. We observed a rapid release of CPMV from the active microneedle platform *in vitro*. Administration of CPMV with active microneedles demonstrated enhanced and more consistent early tumor regression compared to conventional injection. This suggests less variability in the process of

administering the treatment with active microneedles relative to injection, as well as obviating the need of application by medical practitioners. Further, the active microneedle offered greatly improved overall survival and tumor growth suppression compared to passive microneedle and injection. Fluorescence examination of CPMV released by active microneedles, passive microneedles, and injection methods *in vivo* indicated broad dispersion with reduced clustering of CPMV nanoparticles within the tumor with microneedle-facilitated administration. Immunohistofluorescence also showed tumor infiltration of leukocytes 24 h after all CPMV treatments, regardless of modality.

The infiltrating innate immune cell profile and dynamics differed between treatment administration modalities. Active microneedle-treated tumors had enrichment of activated DCs, M1s, and NK cells in this infiltrate relative to that of CPMV injection-treated tumors, which is consistent with the greater tumor regression after active microneedle treatment that was observed. Additionally, passive microneedle-treated tumors seemed to have delayed or only modest changes in its immune profile. Finally, evaluation of $CD8^+$ splenocytes, critical mediators of a systemic adaptive antitumor response[23,26,27], revealed enhancement of activated $CD8^+$ T cells that recognize CPMV and B16F10 cell lysate in mice treated by microneedles. The active microneedle-treated mice had greater enhancement than the passive microneedle-treated mice. This is also consistent with the improved survival of mice treated with active microneedles over those treated with passive microneedles and injection.

We show here that this process of active microneedle delivery not only facilitates and enhance distribution and permeation of the CPMV, but also augments and accelerates the early IT innate immune response. This change in the innate immune response also appears to be followed by enhancement of $CD8^+$ T cell activation within distant lymphoid tissue, such as the spleen. This augmentation in immune responses with active microneedle patch indicates a benefit beyond improved drug delivery that is complementary to the mechanisms of action of CPMV *in situ* vaccination. While outside of the scope of this present study, future studies should investigate the mechanisms of these accelerated and augmented immune responses.

This active transdermal delivery system is appealing for *in situ* vaccination of solid cutaneous tumors due to its excellent biocompatibility, versatility, and facilitation of rapid and deep payload drug penetration. We envision that this drug delivery platform will increase the feasibility and accessibility of *in situ* vaccination for cutaneous tumors, potentially allowing for self-administration of therapy. In addition, this strategy of active, controlled CPMV delivery may be extended further to improve treatment of deeper, less accessible solid tumors. While CPMV *in situ* vaccination has been efficacious with direct IT injection in some of these types of tumors, the aforementioned limitations of conventional injection remain. Injection of CPMV contained within an autonomous carrier containing active micromotors could similarly overcome limitations of CPMV injection in these conditions and facilitate minimally invasive treatment of wide range of solid tumors.

Chapter 2.1 is based, in part, on the material as it appears in Advanced Materials, 2020, by Miguel Angel Lopez Ramirez, Fernando Soto, Chao Wang, Ricardo Rueda, Sourabh Shukla, Cristian Silva Lopez, Daniel Kupor, David A. McBride, Jonathan K. Pokorski, Amir Nourhani, Nicole F. Steinmetz, Nisarg J. Shah, Joseph Wang. The dissertation author was the primary investigator and author of this paper.

Chapter 2.2 is based, in part, on the material as appears in Advanced Materials, 2020, by Miguel Angel Lopez Ramirez, Fernando Soto, Chao Wang, Ricardo Rueda, Sourabh Shukla, Cristian Silva Lopez, Daniel Kupor, David A. McBride, Jonathan K. Pokorski, Amir Nourhani, Nicole F. Steinmetz, Nisarg J. Shah, Joseph Wang. The dissertation author was the primary investigator and author of this paper.

Chapter 2.3 is based, in part, on the material as appears in ACS Applied Nano Materials, 2020, by Christine E. Boone, Chao Wang, Miguel Angel Lopez Ramirez, Veronique Beiss, Sourabh Shukla, Paul L. Chariou, Daniel Kupor, Ricardo Rueda, Joseph Wang, Nicole F. Steinmetz. The dissertation author was a coauthor of this paper.

2.3.5 References

1. M. C. Chen, Z. W. Lin, M. H. Ling, ACS Nano 2016, 10, 93–101.

2. R. F. Donnelly, D. I. J. Morrow, P. A. McCarron, A. D. Woolfson, A. Morrissey, P. Juzenas, A. Juzeniene, V. Iani, H. O. McCarthy, J. Moan, J. Control Release 2008, 129, 154–162.

3. S. Bhatnagar, N. G. Bankar, M. V. Kulkarni, V. V. K. Venuganti, Int. J. Pharm. 2019, 556, 263–275.

4. A. F. Moreira, C. F. Rodrigues, T. A. Jacinto, S. P. Miguel, E. C. Costa, I. J. Correia, Pharmacol. Res. 2019, 148, 104438.

5. Y. Ye, C. Wang, X. Zhang, Q. Hu, Y. Zhang, Q. Liu, D. Wen, J. Milligan, A. Bellotti, L. Huang, G. Dotti, Z. Gu, Sci. Immunol. 2017, 2.

6. N. W. Kim, S. Y. Kim, J. E. Lee, Y. Yin, J. H. Lee, S. Y. Lim, E. S. Kim, H. T. T. Duong, H. K. Kim, S. Kim, J. E. Kim, D. S. Lee, J. Kim, M. S. Lee, Y. T. Lim, J. H. Jeong, ACS Nano 2018, 12, 9702–9713.

7. M. Zaric, O. Lyubomska, O. Touzelet, C. Poux, S. Al-Zahrani, F. Fay, L. Wallace, D. Terhorst, B. Malissen, S. Henri, U. F. Power, C. J. Scott, R. F. Donnelly, ACS Nano 2013, 7, 2042–2055.

8. S. A. Tawde, L. Chablani, A. Akalkotkar, M. J. D'Souza, J. Controlled Release 2016, 235, 147–154.

9. C. Wang, Y. Ye, G. M. Hochu, H. Sadeghifar, Z. Gu, Nano Lett. 2016, 16, 2334–2340.

10. Y. Ye, J. Wang, Q. Hu, G. M. Hochu, H. Xin, C. Wang, Z. Gu, ACS Nano 2016, 10, 8956–8963.

11. C. H. Heldin, K. Rubin, K. Pietras, A. Ostman, Nat. Rev. Cancer 2004, 4, 806–813.

12. B. Goins, W. T. Phillips, A. Bao, Expert Opin. Drug Deliv. 2016, 13, 873–889.

13. M. Reth, Nat. Immunol. 2013, 14, 765–767.

14. S. O. Choi, Y. C. Kim, J. H. Park, J. Hutcheson, H. S. Gill, Y. K. Yoon, M. R. Prausnitz, M. G. Allen, Biomed. Microdevices 2010, 12, 263–273.

15. A. R. Denet, R. Vanbever, V. Préat, Adv. Drug Deliv. Rev. 2004, 56, 659–674.

16. H. Lee, C. Song, Y. S. Hong, M. S. Kim, H. R. Cho, T. Kang, K. Shin, S. H. Choi, T. Hyeon, D.H. Kim, Sci. Adv. 2017, 3, e1601314.

17. H. Lee, T. K. Choi, Y. B. Lee, H. R. Cho, R. Ghaffari, L. Wang, H. J. Choi, T. D. Chung, N. Lu, T. Hyeon, S. H. Choi, D.H. Kim, Nat. Nanotechnol. 2016, 11, 566–572.

18. A. Zandi, M. A. Khayamian, M. Saghafi, S. Shalileh, P. Katebi, S. Assadi, A. Gilani, M. S. Parizi, S. Vanaei, M. R. Esmailinejad, F. Abbasvandi, P. Hoseinpour, M. Abdolahad, Adv. Healthc. Mater. 2019, 8, 1900613.

19. S. Mitragotri, D. Blankschtein, R. Langer, Ultrasound-Mediated Transdermal Protein Delivery. Science 1995, 269, 850–853.

20. J. Orozco, G. Cheng, D. Vilela, S. Sattayasamitsathit, R. Vazquez-Duhalt, Valdés- G. Ramírez, O. S. Pak, A. Escarpa, C. Kan, J. Wang, Angew. Chem. Int. Ed Engl. 2013, 52, 13276–13279.

21. Z. Wu, J. Li, Ávila, Esteban-Fernández de Ávila B. T. Li, W. Gao, Q. He, L. Zhang, J. Wang, Adv. Funct. Mater. 2015, 25, 7497–7501.

22. M. A. Lopez-Ramirez, F. Soto, C. Wang, R. Rueda, S. Shukla, C. Silva-Lopez, D. Kupor, D. A. McBride, J. K. Pokorski, A. Nourhani, N. F. Steinmetz, N. J. Shah, J. Wang, Adv. Mater. 2020, 32, 1905740.

23. P. H. Lizotte, A. M. Wen, M. R. Sheen, J. Fields, P. Rojanasopondist, N. F. Steinmetz, Fiering, S. Nat. Nanotechnol. 2016, 11, 295–303.

24. K. L. Lee, A. A. Murray, D. H. T. Le, M. R. Sheen, S. Shukla, U. Commandeur, S. Fiering, N. F. Steinmetz, Nano Lett. 2017, 17, 4019–4028.

25. A. Kerstetter-Fogle, S. Shukla, C. Wang, V. Beiss, P. L. R. Harris, A. E. Sloan, N. F. Steinmetz, Cancers 2019, 11, 515.

26. C. Wang, S. N. Fiering, N. F. Steinmetz, Adv. Ther. 2019, 2, 1900003.

27. A. A. Murray, C. Wang, S. Fiering, N. F. Steinmetz, Mol. Pharm. 2018, 15, 3700–3716.

28. H. Cai, C. Wang, S. Shukla, N. F. Steinmetz, Adv. Sci. 2019, 6, 1802281.

29. H. Cai, S. Shukla, C. Wang, H. Masarapu, N. F. J. Steinmetz, Am. Chem. Soc. 2019, 141, 6509–6518.

30. Z. Wang, V. H. Wu, M. M. Allevato, M. Gilardi, Y. He, J. L. Callejas-Valera, L. Vitale-Cross, D. Martin, P. Amornphimoltham, J. Mcdermott, B. Yung, S Y. Goto, A. A.

Molinolo, A. B. Sharabi, E. E. W. Cohen, Q. Chen, J. G. Lyons, L. B. Alexandrov, J. S. Gutkind, Nat. Commun, 2019, 10, 5546.

31. P. J. Hoopes, R. J. Wagner, K. Duval, K. Kang, D. J. Gladstone, K. L. Moodie, M. Crary-Burney, H. Ariaspulido, F. A. Veliz, N. F. Steinmetz, S. N. Fiering, Mol. Pharm. 2018, 15, 3717–3722.

32. G. Poste, J. Doll, I. J. Fidler, Proc. Natl. Acad. Sci. 1981, 78, 6226–6230.

33. T. M. Grzywa, W. Paskal, P. K. Włodarski, Transl. Oncol. 2017, 10, 956–975.

34. A. A. Murray, M. R. Sheen, F. A. Veliz, S. N. Fiering, N. F Steinmetz, 2019, 2000, 111–124.

35. Q. Wang, E. Kaltgrad, T. Lin, J. E. Johnson, M. G. Finn, Chem. Biol. 2002, 9, 805–811.

36. A. M. Wen, M. Infusino, A. De Luca, D. L. Kernan, A. E. Czapar, G. Strangi, N. F. Steinmetz, Bioconjug. Chem. 2015, 26, 51–62.

37. P. L. Chariou, A. B. Dogan, A. G. Welsh, G. M. Saidel, H. Baskaran, N. F. Steinmetz, Nat. Nanotechnol. 2019, 14, 712–718.

38. H. M. Aly, H. L. A. El-Mohdy, Arab. J. Sci. Eng. 2016, 41, 2199–2209.

39. S. P. Sullivan, D. G. Koutsonanos, M. Del Pilar Martin, J. W. Lee, V. Zarnitsyn, S.-O. Choi, N. Murthy, R. W. Compans, I. Skountzou, M. R. Prausnitz, Nat. Med. 2010, 16, 915–920.

40. G. J. Randolph, V. Angeli, M. A. Swartz, Nat. Rev. Immunol. 2005, 5, 617–628.

41. M. Tomura, A. Hata, S. Matsuoka, F. H. W. Shand, Y. Nakanishi, R. Ikebuchi, S. Ueha, H. Tsutsui, K. Inaba, K. Matsushima, A. Miyawaki, K. Kabashima, T. Watanabe, O. Kanagawa, Sci. Rep. 2014, 4, 1–11.

42. C. Ruedl, P. Koebel, M. Bachmann, M. Hess, K. J. Karjalainen, Immunol. 2000, 165, 4910–4916.

43. M. Najafi, N. H. Goradel, B. Farhood, E. Salehi, M. S. Nashtaei, N. Khanlarkhani, Z. Khezri, J. Majidpoor, M. Abouzaripour, M. Habibi, I. R. Kashani, K. J. Mortezaee, Cell. Biochem. 2019, 120, 2756–2765.

44. V. Kumar, S. Patel, E. Tcyganov, D. I. Gabrilovich, Trends Immunol. 2016, 37, 208–220.

45. D. Bayik, D. Tross, D. M. Klinman, Front. Immunol. 2018, 9, 608.

46. R. J. Tesi, Trends Pharmacol. Sci. 2019, 40, 4–7.

47. T. C. van der Sluis, M. Sluijter, S. van Duikeren, B. L. West, C. J. M. Melief, R. Arens, S. H. van der Burg, T. van Hall, Cancer Immunol. Res. 2015, 3, 1042–1051.

48. B. Bonnotte, N. Larmonier, N. Favre, A. Fromentin, M. Moutet, M. Martin, S. Gurbuxani, E. Solary, B. Chauffert, F. J. Martin, Immunol. 2001, 167, 5077–5083.

49. Nakagawa, R.; Serizawa, I.; Motoki, K.; Sato, M.; Ueno, H.; Iijima, R.; Nakamura, H.; Shimosaka, A.; Koezuka, Y. Oncol. Res. 2000, 12, 51–58.

50. R. Eil, S. K. Vodnala, D. Clever, C. A. Klebanoff, M. Sukumar, J. H. Pan, D. C. Palmer, A. Gros, T. N. Yamamoto, S. J. Patel, G. C. Guittard, Z. Yu, V. Carbonaro, K. Okkenhaug, D. S. Schrump, W. M. Linehan, R. Roychoudhuri, N. P. Restifo, Nature 2016, 537, 539–543.

51. F.Y. Li, B. Chaigne-Delalande, C. Kanellopoulou, J. C. Davis, H. F. Matthews, D. C. Douek, J. I. Cohen, G. Uzel, H. C. Su, M. J. Lenardo, Nature 2011, 475, 471–476.

52. K. Feser, M. Kietzmann, W. Bäumer, C. Krause, F. W. J. Bach, Biomater. Appl. 2011, 25, 685–697.

53. B. Li, H. Cao, Y. Zhao, M. Cheng, H. Qin, T. Cheng, Y. Hu, X. Zhang, X. Liu, Sci. Rep. 2017, 7, 1–12.

54. D. M. McKinney, R. Skvoretz, M. Qin, G. Ishioka, A. Sette, Immunization. J. Immunol. Methods 2000, 237, 105–117.

55. ELISPOT Assay: Detection of IFN-γ Secreting Splenocytes | Protocol https://www.jove.com/science-education/10497/elispot-assay-detection-of-ifn-secreting-splenocytes (accessed Apr 2, 2020).

56. A. W. Yewdall, S. B. Drutman, F. Jinwala, K. S. Bahjat, N. Bhardwaj, PLOS ONE 2010, 5, e11144.

57. R. Zhang, F. Yuan, Y. Shu, Y. Tian, B. Zhou, L. Yi, X. Zhang, Z. Ding, H. Xu, L. Yang, Cancer Immunol. Immunother. 2020, 69, 135–145.

58. S. Shukla, M. Jandzinski, C. Wang, X. Gong, K. W. Bonk, R. A. Keri, N. F. Steinmetz, Adv. Ther. 2019, 2, 1800139.

59. M. Amjadi, S. Sheykhansari, B. J. Nelson, M. Sitti, Adv. Mater. 2018, 30, 1704530.

60. Y. Ye, J. Yu, D. Wen, A. R. Kahkoska, Z. Gu, Adv. Drug Deliv. Rev. 2018, 127, 106–118.

61. Y. He, C. Hong, J. Li, M. T. Howard, Y. Li, M. E. Turvey, D. S. S. M. Uppu, J. R. Martin, K. Zhang, D. J. Irvine, P. T. Hammond, ACS Nano 2018, 12, 10272–10280.

Chapter 3. Combinatorial Microneedle System/Patch with Tunable Release Kinetics and Dual-Fast-Deep/Sustained Release Capabilities

3.1 Introduction

Advanced microfabrication methods have enabled the development of microneedle arrays as novel transdermal drug-delivery devices,[1,2] that are widely used for treating diverse disease conditions ranging from superficial dermatitis to diabetes and chronic pain.[3-8] Microneedles are microscale structures that allow the delivery of drugs within few microns of the skin and are considered minimally invasive with minimal patient-reported pain compared to traditional hypodermic needles,[9-12] requiring minimal training from medical practitioners,[13,14] avoiding the cold chain (refrigeration, storage) and are thus suitable for application in remote locations. Optimal design of microneedle balances various parameters that determine the drug delivery efficiency, mechanical strength, or manufacturability. Currently, microneedle patches play an essential role in a wide variety of biomedical research applications and are well tolerated in clinical trials,[15,16] leaving behind only biocompatible, dissolvable and hence safe soluble materials when compared to the conventional biohazardous waste left from the needle and syringe. Previous research with microneedle patches has involved the delivery of small molecules,[17,18] biomacromolecules,[19,20] and nanoparticles (NPs),[21,22] using either coated or non-coated dissolvable microneedles,[23,24] usually comprised of highly water-soluble polymer matrixes with narrow development in sustained release applications,[25-30] and limited development in hybrid/programmable microneedle patches.[31] For example, Nguyen's team recently described core-shell microneedles that can deliver cargoes in a pulsatile manner, mimicking release via repetitive bolus injections over long periods of time.[32]

Nevertheless, each disease has diverse needs and requires different delivery strategies, immediate (fast-acting), or sustained (prolonged) release. Our ultimate goal is to offer effective post-operative pain management via a fast-local anesthetic delivery for immediate pain relief along with co-delivery of a second anesthetic to address prolonged sustained effects. Consequently, the development of improved, practical and efficient microneedle patches with tunable dissolution and release kinetics, is necessary and urgently needed in a wide variety of medical applications, as they remain largely unexplored.[33]

Herein, we present a dual-action programmable combinatorial microneedle patch with tunable fast-acting and sustained release of different payloads. The novel dual-action patch was engineered and designed to have two spatially resolved microneedle compartments with different dissolution rates and a tunable payload release. The first compartment (active microneedles) made of carboxymethylcellulose (CMC) dissolvable polymer needles allowed a fast and forceful immediate payload release (within ~5 minutes) by incorporating biocompatible and degradable active Mg microparticles. Skin insertion of the fast acting microneedles enables instantaneous reaction of the embedded Mg particles with the surrounding interstitial fluid, resulting in the formation of gas (hydrogen) microbubbles, that induce localized vortex flow fields and a 'pumping-like' action within the application site. Simultaneously, the nearby second compartment (the sustained microneedle zone) is made of different concentrations of Eudragit®L100, to allow a controlled and constant sustained payload release over prolonged time periods, ranging from weeks to months. We have recently demonstrated the utility of active Mg-

based ballistic microneedle for effective *in vivo* melanoma tumor eradication.[34,35] Here we combine such ballistic payload delivery with sustained payload delivery using a single microneedle patch footprint that offers fast- and sustained co-delivery at two neighboring microneedle compartment zones.

We envision that this fast-acting/sustained release patch will set the foundation for future microneedle research towards next generation patches, able to treat diverse disease conditions per single application at low manufacturing cost. The ultimate goal of our collaborative research is to apply this unique delivery capability for the management of pain, considering the current limitations of existing pain-relieving patch technologies, such as general Mylan generic lidocaine patches,[36] and the lack of effective transdermal modalities for post-operative settings.[37] Such post-operative pain control will be realized using a single patch, providing fast and slow tunable delivery of the corresponding anesthetic drugs. Yet, the new delivery concept goes beyond pain management as it could greatly benefit broad medical scenarios. In the following sections we present the detailed characterization of the new combinatorial microneedle patch, including its design, fabrication, and performance *in vitro* and *ex vivo*.

3.2 Experimental Methods

Materials

Sodium carboxymethyl cellulose (CMC, 419303, average MW=250K), Fluorescein 5(6)-isothiocyanate (FITC, 46950; λex/λem, 492/518 nm), Rhodamine 6G (Rh6G, R4127; λex/λem, 526/555 nm, respectively), polyvinylpyrrolidone (PVP 360,

MW=360K), 2-propanol, ethanol, ethyl acetate and PLGA (50:50) were purchased from Sigma Aldrich. AnyCubic-black colored acrylate resin was purchased from Anycubic. A 60W Mercury Lamp was purchased from Moai–Peopoly. Polydimethylsiloxane SYLGARD® 184 solution was purchased from Ellsworth Adhesives. Mg microparticles (catalog #FMW40) were purchased from TangShanWeiHao Magnesium Powder Co., Ltd China. The adhesive was purchased from 3M. Porcine skin was bought at a local supermarket.

Microneedle CAD/CAM design

Drafting of the computer aided design (CAD) model of the printed part was custom designed in a modeling program (Solidworks version 2019-2020) and ran in an operated Microsoft system-based computer. Models were transferred to a free open-source SLA/DLP/LCD 3D printer software to adjust, prepare and edit the 3D model (Chitubox-Version 1.6.3) prior slicing and printing. Specifically, the developing of supports and lattices for each model with the corresponding dimensions and connections to prevent printing failure. Computer aided manufacturing (CAM) was developed by AnyCubic Photon Slicer Software with the parameters listed in Table 1 and 2.

3D lithographic microneedle printing

The direct light processing (DLP) fabrication of microneedles was developed with the use of an AnyCubic Photon UV LCD 3D Printer. The DLP 3D printer projected a 25W UV light source through a 2K LCD masking photocuring a liquid resin material (black colored acrylate resin). The 3D printed models were mass produced and cured in a layer by layer fashion (20-50μm layers). Printed models were removed from the 115 x 65mm metal build plate and supports trimmed. The microneedle models were tippled rinsed with 2-propanol and further placed within an ultrasonic bath to remove uncured resin material in excess.

Microneedle post processing

Post processing of the printed microneedle mold was performed by an additional post curing step under a 60W Mercury UV Curing Lamp for 30 min. Subsequently, microneedles in a metal plate (10cm x 10 cm; 2 mm thickness) were heat treated at a fixed temperature (120 ^{o}C) for different times (3-30 min) in a conventional oven. Detailed parameters of post processing are listed in Table S3, supporting information.

PDMS microneedle micromold fabrication

The PDMS micromolding process of 3D printed microneedles allowed the fabrication of reusable negative templates for the mass production of combinatorial polymeric microneedle arrays. The fabrication of silicone microneedle molds was done by the

following procedure: PDMS (12g, 86/14; base/curing agent) solution was casted over a combinatorial microneedle array attached to a crystal-clear borosilicate petri dish glass. Afterwards, PDMS was degassed in a sealed desiccator connected to a vacuum pump for 15 min at 23 in Hg. PDMS was set to cure (30 min at 85°C) in an oven and further demolded from the master combinatorial microneedle array, thus obtaining the final combinatorial negative mold. Negative molds were resized with the use of a stainless-steel blade cut and triple cleaned/washed with hand soap; subsequently allocated in an ultrasonic bath, temperature treated at 80^{o}C and stored in a sealed container prior use.

PLGA microparticle synthesis

The fabrication method of the Rh6G-loaded PLGA microparticles was based on an emulsion solvent evaporation technique. Briefly, PLGA (30mg) was dissolved in chloroform (1mL). Subsequently, Rh6G (5mg) was dispersed in the polymer solution, and further poured into a 2% PVA aqueous solution (10mL). Solution was emulsified with the use of a high-speed ultrasonic homogenizer (ultrasonics) by three 3s (100W) pulses. The organic phase was allowed to evaporate by continuous mixing (900 rpm) for 18h at ambient temperature. PLGA microparticles were collected by centrifugal force (10,000 rpm) for 7 min and tripled washed with deionized water. Microparticles were

suspended in deionized water and then used for microneedle patch fabrication and particle characterization.

Combinatorial polymeric microneedle micromolding

The fabrication of the combinatorial (active/sustained) polymeric microneedle patch was realized by a micromolding approach following the next procedure: briefly, the compartment designated for the active microneedles was primarily loaded and packed with Mg microparticles (0, 0.5, 1, 2, or 3 mg) by employing a 2-propanol Mg microparticle suspension (50 mg mL^{-1}), followed by casting a 3% (w/v) CMC (50 μL) aqueous polymer solution (pH 10.5 to prevent Mg microparticle reaction) supplemented with FITC (1mg). Molds were allocated under a sealed desiccator connected to a vacuum pump (23 in Hg) for 5 min. Bubbles were removed from the mold and the process was repeated by triplicate. Excess of solution was removed from the mold by swiping it with the use of a blade cut and saved for next fabrication. The active compartment was allowed to dry for 15 min at room temperature prior the following compartment fabrication. The procedure of the sustained release compartment fabrication was performed by loading it with a polymeric blend of a 4%, 8%, 16% and 24% (100μL, Ethanol/2-propanol; 50/50% *v/v*) solution of Eudragit®L100 supplemented with Rh6G (0.5mg). Similarly, excess of solution was removed from the mold by swiping it in circular motion with the use of a blade cut and saved for next mold fabrication. The sustained release compartment was further allowed to dry for 15 min at room temperature. The finished combinatorial microneedle mold was placed inside a

conventional oven for 2h at 70°C. For the release kinetics experiments a layer of PVP was added as a support base on top of the active or sustain release compartment by casting an ethanol based (50 µL) or water based (100µL) 10% (w/v) PVP solution respectively and let to dry overnight. Finally, the active/sustained combinatorial microneedle patch was obtained by a demolding procedure; in brief, after drying, a 1 mm circular adhesive was adapted to the backing of the microneedle patches and demolded. The reason behind the PVP layers was to efficiently detach the needles for release measurements and to prove mechanical stability. Prior use, the combinatorial microneedle patches were stored in a sealed container at room temperature. CMC, PVP, Eudragit®L100 polymer solutions were prepared using a dual asymmetric centrifugal mixer (Flacktek Speedmixer, DAC 150.1 KV-K, FlackTek, SC, U. S. A.), speed of 2500 rpm for 5 min (by triplicate). Combinatorial microneedle patches loaded with PLGA microparticles were fabricated following the same procedure. Nevertheless, instead of Rhd6G alone, PLGA@Rh6G microparticle suspension (30µL) was infiltrated within the cavities of the silicon molds, and polyvinylpyrrolidone (PVP) was casted on top as the matrix microneedle material. Even though the polymer matrix is made of a water-soluble material, PLGA@Rh6G microparticles provided sustained release over prolonged periods of time.

Microneedle patch imaging characterization

Fluorescent microscopy images of the combinatorial microneedle patches were developed with the use of a fluorescent microscope (EVOS FL coupled with 2x and 4x objectives and GFP and RFP filters) for the imaging of Rh6G and FITC. SEM images

were performed by a FEI Quanta 250 ESEM instrument (Hillsboro, Oregon, USA). Prior imaging, the 3D printed, and polymeric combinatorial microneedle patches were sputtered with Iridium in an Emitech K575X Sputter Coater, providing a fine grain metal deposition; samples were imaged at acceleration voltages between 3-5 keV. Bright field and colored images were obtained by a 3.5X-180X Simul-Focal Stereo Zoom Microscope coupled with an 18MP digital camera. Digital fluorescent images of the combinatorial microneedle patch before and after dissolution were carried out with a digital camera Nikon D7000 coupled with a 40mm 2.8G macro lens; microneedle patches were placed under a portable UV lamp projecting a 365nm wavelength light.

Microneedle patch dissolution experiments

To image the dissolution in solution of our combinatorial microneedle, 3 continuous microneedles (active or sustained, loaded with FITC or Nile Red, respectively) were attached horizontally to a clear glass slide with 4 acrylate walls to contain solution. To capture the dissolution in real time, Phosphate buffered solution (pH 7.4) was administrated to the microneedle setup, followed by time-set point frame images with use of a fluorescent microscope (EVOS FL coupled with a 4x objective and GFP-RFP filters).

Microneedle patch mechanical strength study

Fast-acting and sustained release microneedle arrays from the patch were set under a mechanical compression test. The set up used was comprised of a Force Gauge Model M4-20 system Mark0-10 Series 4, a metal plate and a stepping-motor controlled biaxial

stage. In brief, each microneedle array was set under a constant load, and the displacement of the base plate in reference to each needle height was monitored and plotted. The fracture (failure) force was determined by a notorious drop in force.

Release Kinetics Experiments

Fast-acting and sustained release microneedle patches were subjected to a release kinetics study. microneedle patches were dissolved in 1000 µL of PBS pH 7.4 at 37.5 °C for different set-time points: the fast-acting microneedle (from 1-10 min) and sustained release compartment (from 1-90 days). Prior each measurement samples were centrifuged at 4000 rpm for 5 min, and the solution release amount was measured by UV-vis spectrophotometry (UV-2450 Shimadzu spectrophotometer). Each measurement was conducted within a 400-700 nm spectrum window. The patches release was plotted vs time. Data was analyzed and charts were generated using Prism 7 (GraphPad software).

PLGA-Rh6G microparticle release study

PLGA@Rh6G microparticles were dissolved in 1000 µL of PBS pH 7.4 at 37.5 °C for different set-time points: (from 1-45 days). Prior to each measurement, samples were centrifuged at 4000 rpm for 5 min and the release amount was measured by UV-vis spectrophotometry (UV-2450 Shimadzu spectrophotometer). Each measurement was conducted within a 400-700 nm spectrum window. Particle release was plotted vs time. Data was analyzed and charts were generated using Prism 7 (GraphPad software).

Skin Penetration Studies

Both fast-acting and sustained release microneedle patches were set to pierce porcine cadaver skin. The skin was stored in a sealed container with PBS (pH 7.4) at room temperature prior use. The combinatorial microneedle patches were applied to the skin manually.

3.3 Experimental Results

The successful realization of the effective combinatorial microneedle array patch, based on the sequential fast and slow release of different payloads, requires judicious selection and systematic optimization of the materials, design, and size to impart the desired biocompatibility and mechanical properties, drug loading capacities and tunable dissolution. The combinatorial microneedle patch has been engineered to have 2 microneedle compartment zones, one of which is able to dissolve and rapidly deliver dosages in minutes, while the second zone is slowly dissolved to release its payload over periods ranging from weeks to months (Figure 3.1a).

Microneedle compartments were formulated using different materials to meet adequate dissolution and delivery times, and their specific composition was optimized for fine tuning the release kinetics (Figure 3.1b**).** The fast-dissolving microneedle compartment was formulated using CMC, a water-soluble and safe polysaccharide,[38] with high biocompatibility and biodegradability in the biomedical field [39,40] often used in biosensors.[41] To facilitate microneedles to dissolve instantly and ensure a rapid, forceful payload release from the fast-dissolving compartment we incorporated biocompatible

active Mg microparticles within different CMC polymer matrix concentrations. The embedded particles lead to localized generation of gas microbubbles and corresponding vortex flow that results in a nearly instantaneous release of the payload, enabling wider and greater payload distribution and permeation in the application area. Recently, our previous active microneedle platform was shown extremely useful for eradicating tumor growth in a murine melanoma model, greatly improving immunotherapeutic efficacy.[34,35]

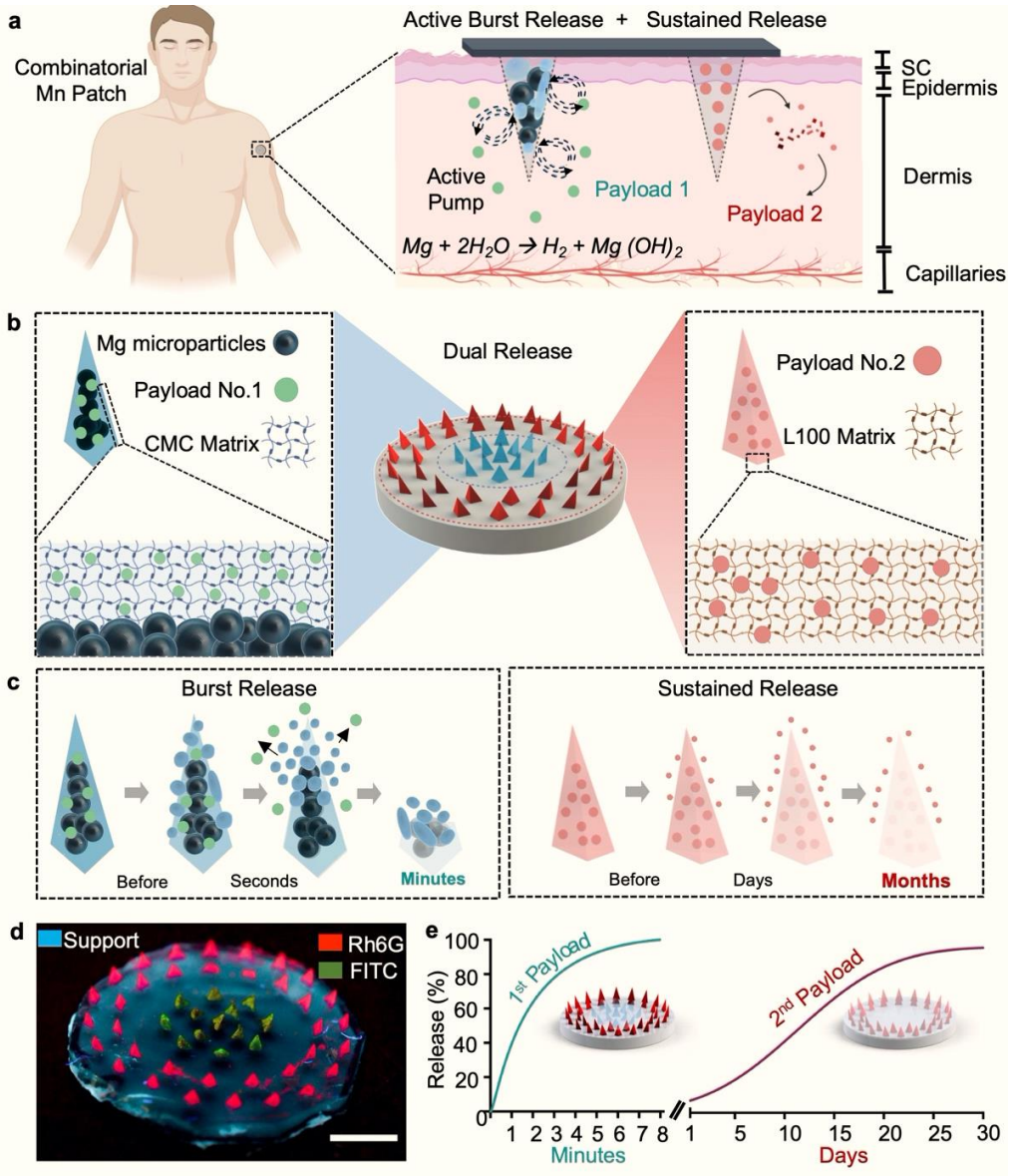

Figure 3.3.1 Combinatorial microneedle patch with programmable (fast /sustained) drug co-delivery. a) Schematics of the combinatorial microneedle patch application process to the skin and dual-stage microneedle delivery: fast-acting and sustained release of two payloads. b) Illustration of the microneedle patch composition. c) Time-frame schematics displaying the delivery performance of both compartments: a fast-active burst release of the first therapeutic, along with a prolonged-sustained delivery of a second drug. d) Digital fluorescence photograph of a combinatorial microneedle patch displaying both microneedle compartments loaded with FITC and Rh6G. Scale bar, 2.5mm. e) Release kinetics representation of a dual-stage microneedle patch, featuring the fast delivery of first therapeutic within minutes, while gradually releasing the second drug over weeks and months.

The sustained release compartment was designed and formulated of a biocompatible methacrylic acid pH sensitive co-polymer (Eudragit®L100).[42-46] The delivery and release of the sustained microneedle compartment can be tailored from weeks to months by tuning the polymer concentration used in the fabrication process, therefore obviating the need to load the drug within nanocarriers,[47-48] hence improving the loading. The different dissolution properties and behavior of the combinatorial microneedle patch (fast-acting and sustained release) are clearly illustrated in Figure 3.1c.

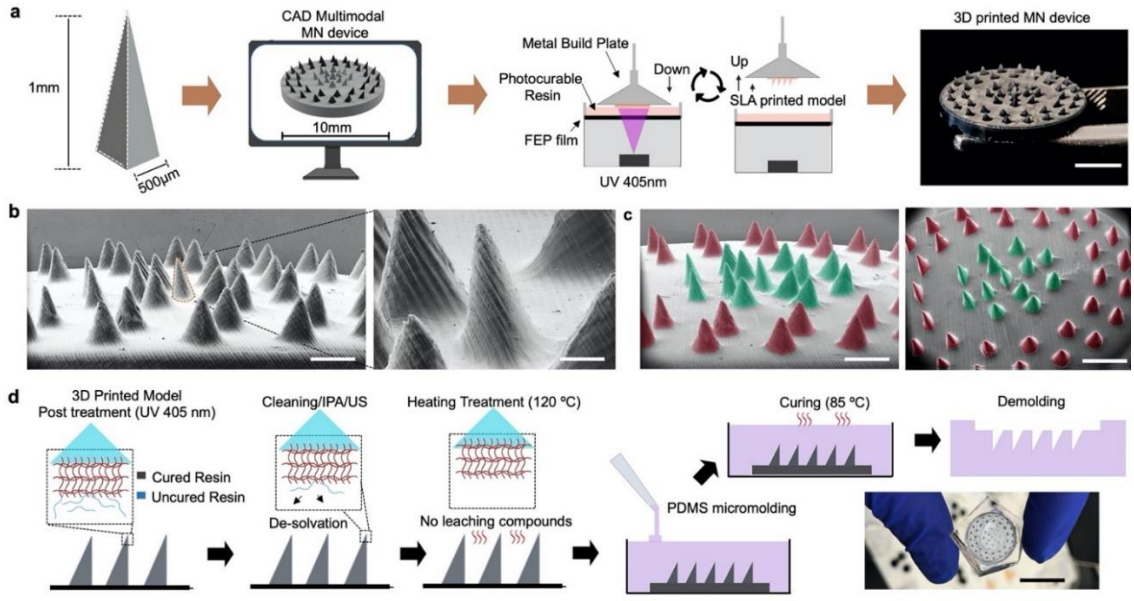

Figure 3.3.2 3D lithographic microneedle printing. a) Drafting of the computer aided design (CAD) model of the combinatorial microneedle patch and lithographic 3D printing process involved along with a digital photograph of the printed part. Scale bar, 2.5mm. b) Scanning Electron Micrograph (SEM) of the circular printed microneedle array. Scale bar, 1mm and 400µm. c) Colored SEM displaying both distributed compartments within the patch: the fast-acting (green) and sustained release (red) arrays. Scale bar, 1.2mm and 2mm, respectively. d) 3D printed microneedle array post processing steps: UV treatment, de-solvation and heating, followed by a subsequent PDMS micromold fabrication.

A characteristic combinatorial microneedle patch displaying both compartments: fast-acting needles loaded with Fluorescein 5(6)-isothiocyanate (FITC), and prolonged release needles loaded with Rhodamine 6G (Rh6g) is shown (Figure 3.1d). Moreover, the release kinetics concept of the dual-stage microneedle patch, featuring the fast delivery of first payload within minutes, while promoting a gradual-sustained release of the second payload for 30 days is shown in Figure 3.1e.

We custom designed and engineered the patch by a mask stereolithography technique (MSLA) with the use of a high-resolution 3D printer. Master microneedle (triangular right angle shaped) mold dimensions were designed to be 550μm in base (triangular base length) x 950μm long (height) arranged in a circular pattern (Figure 3.2a).

Table 3.3.1 Lithographic 3D printing parameters of **microneedle** arrays: variable layer thickness (20-100 μm), no angle.

Layer Thickness (mm)	**Exposure Time (s)**	**Off time (s)**	**Bottom Exposure (s)**	**Bottom Layers**	**Support Angle**
0.02	10	3	80	25	0
0.05	10	3	80	10	0
0.1	10	3	80	5	0

The outer compartment comprised of two concentric circular arrays of 35 microneedles while the middle compartment of 13 microneedles. The base of the array was designed to be 10mm in diameter and 2mm in thickness to ensure facile

polydimethylsiloxane (PDMS) micromolding steps. The direct light process (DLP) fabrication projected a 25W UV light source through a 2K LCD masking, photocuring a liquid acrylate resin material in a layer-by-layer additive manufacturing fashion (detailed fabrication in experimental section).

Table 3.3.2 Lithographic 3D printing parameters of microneedle arrays: variable angle (30-55 deg) with 20 µm layer thickness.

Layer Thickness (mm)	Exposure Time (s)	Off time (s)	Bottom Exposure (s)	Bottom Layers	Support Angle	Tip Sharpness
0.02	10	3	80	25	55	~20µm
0.02	10	3	80	25	45	~20µm
0.02	10	3	80	25	30	~20µm

An evaluation of different 3D printing parameters to enable controllable dimensions, surface stepping/smoothness and tip sharpness can be found in Table 3.1 and Table 3.2. Master microneedle arrays were subjected to a scanning electron micrograph (SEM) to verify needle quality after each printed batch; a characteristic SEM of the master combinatorial microneedle array printed after optimization is shown in Figure 3.2b.

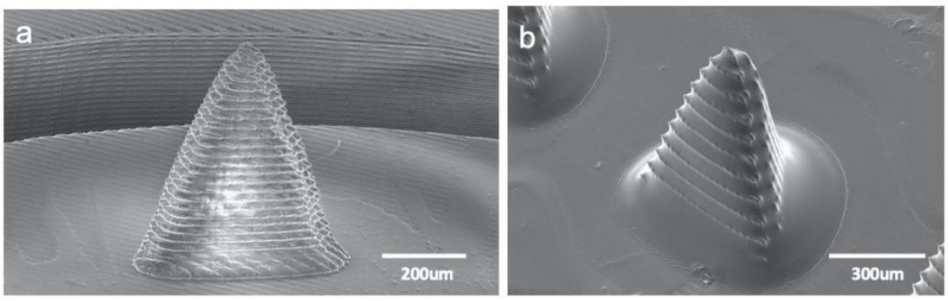

Figure 3.3.3 Lithographic 3D printed microneedles: a) 20 µm layers, b) 50 µm layers, both printed at 0 deg.

Additional SEM images of different printing parameters can be found in Figure 3.3 and 3.4, illustrating a notorious difference when microneedle models are printed at an angle above 45e deg, with best results in sharpness and smoothness at 55 deg (Figure 3.4a) when compared to the ones printed horizontally (Figure 3.3a). Colored SEM image of the master array clearly depicting the spatially resolved microneedle compartments is shown in Figure 3.2c (fast-acting and sustained microneedles in green and red, respectively).

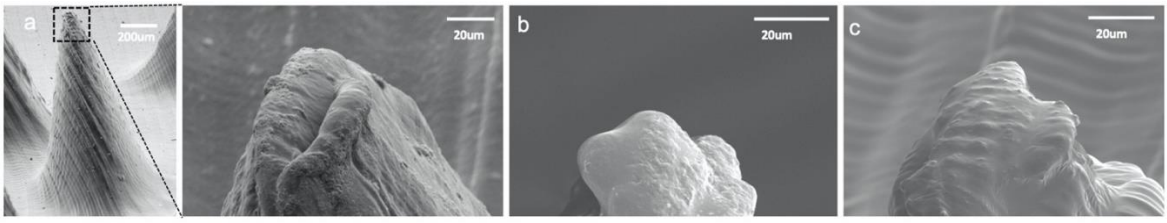

Figure 3.3.4 Lithographic 3D printed microneedle tip sharpness (20 µm layer thickness): a) support angle 55 deg, b) support angle 45 deg, c) support angle 30 deg.

Prior to the fabrication of negative micromolding steps, master microneedle arrays were subjected to a post processing procedure to remove all leaching compounds inherent

from the acrylate resin used in the printing process (Figure 3.2d). Leaching compounds demonstrated to inhibit the PDMS curing process, not enabling it to correctly reproduce master mold features, leaving behind not useful silicone molds; molds required to be subjected under UV light (405 nm) and temperature treated for different times (detailed fabrication in experimental section and Table 3.3). Following post treatment, silicone negative molds were developed by casting PDMS over post-processed master microneedle arrays (Figure 3.2e).

We molded combinatorial microneedles by casting different materials onto each compartment. Briefly, to prepare fast-acting microneedles we proceeded to pack Mg microparticles (30-100µm in diameter) into mold cavities by a drop casting process using a Mg-isopropanol suspension. After the solvent was evaporated, we proceeded to cast an aqueous solution (H_2O, pH 10.5) to solubilize CMC (2, 3 and 4%, w/v) and FITC enabling a slow evaporation under vacuum during the active compartment fabrication. The cavities designated for sustained release microneedles were subsequently filled under vacuum by casting an organic solvent (ethanol/isopropanol, 50:50% v/v) to solubilize Rh6G and Eudragit®L100 (4, 8, 16 and 24%, w/v).

Table 3.3.3 PDMS micromolding and post curing parameters: temperature and UV exposure time.

3D printed mold heating (ºC)	**Exposure Time (min)**	**PDMS base:curing agent**	**PDMS curing temperature(ºC)**	**PDMS curing time**	**Result**
120	3	84:16	85	30 min	PDMS Curing Process Inhibited
120	5	84:16	85	30 min	-
120	10	84:16	85	30 min	-
120	15	84:16	85	30 min	-
120	20	84:16	85	30 min	Mold cured correctly
120	25	84:16	85	30 min	+
120	30	84:16	85	30 min	+
120	30	84:16	Room Temperature	24 hours	+

After having both microneedle compartment cavities filled and dried, molds were allocated inside a conventional oven to enhance microneedle strength. Later, an aqueous and ethanol based polyvinylpyrrolidone (PVP, 10%, w/v) backing solution was applied to the fast-acting and sustained release microneedle compartments, respectively. The resulting combinatorial microneedle patch was then transferred to a slightly larger

medical adhesive. The patch was custom designed to be small, enabling ease of use, facile transportation and consequently easy storage and handling. Schematics of the steps involved (side and top views) in the fabrication of combinatorial microneedle patches are illustrated in Figure 3.5a (detailed fabrication in experimental section).

Combinatorial microneedle patches were formulated from different polymer concentrations. Therefore, we decided to examine their dissolution properties by imaging them at different times. Time-frame fluorescence microscopy dissolution images of characteristic fast-acting microneedle formulations can be found in Figure 3.5b. Fast-acting needle dissolution images (30s intervals) with variable concentration (2, 3 and 4% CMC) showed that the polymer matrix is dissolved almost instantly when in contact with the solution (phosphate buffered solution (PBS) pH 7.4). Images clearly show the spontaneous and vigorous H_2 pump activity from the entrapped Mg microparticles as soon as they are exposed to the solution. From this perspective, no significant difference was found within groups examined, as all demonstrated complete microneedle dissolution within a short period of time displaying rapid particle activation.

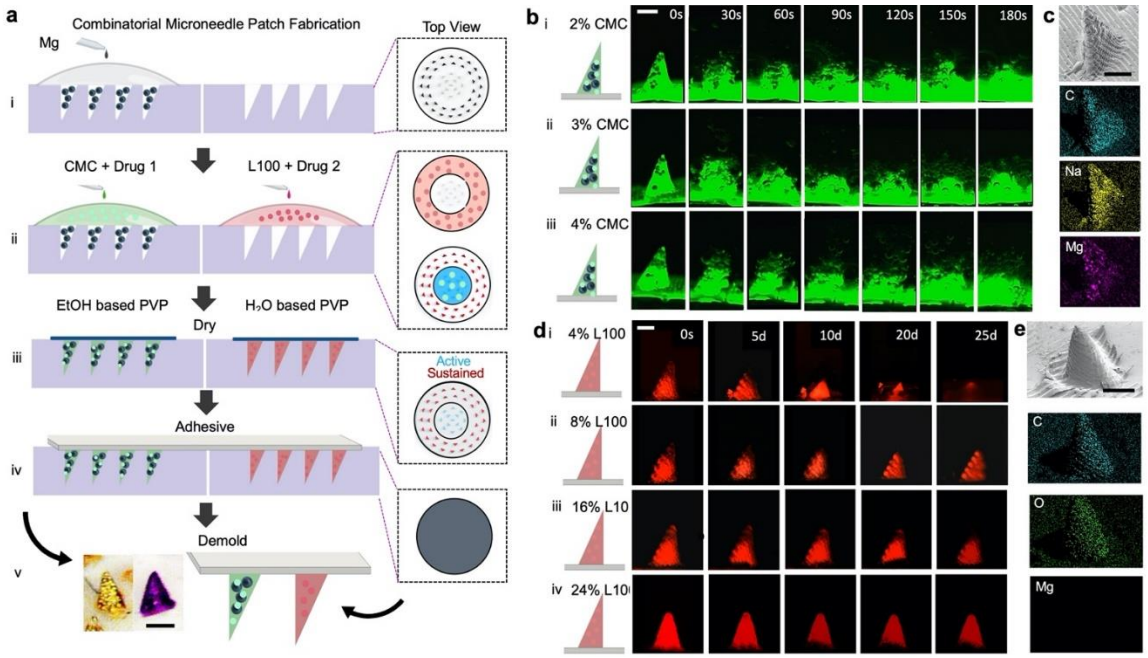

Figure 3.3.5 Dual-stage combinatorial microneedle patch for the simultaneous co-delivery of different drug payloads. a) Schematics of the steps involved in the fabrication of combinatorial microneedle patches (side and top view) for the fast-acting and sustained delivery: active particle loading (i), polymer (CMC, Eudragit®L100) and payload inclusion (FITC, Rh6G), respectively (ii), polymer base and drying (iii), adhesive application (iv) and demolding (v). b) Fluorescence microscopy time-frame dissolution images of the "fast-acting" microneedle compartment, displaying a rapid polymer matrix dissolution driven by the reactivity of Mg microparticles (30 s intervals) (i) 2% CMC, (ii) 3% CMC, (iii) 4% CMC, packed with 1mg of Mg. Scale bar, 400µm. c) SEM image of a characteristic fast-acting microneedle and its corresponding energy dispersive x-ray elemental analysis (C, Na and Mg). (iii) Scale bar, 400µm. d) Fluorescence microscopy time-frame dissolution images of the "sustained release" microneedle compartment, displaying slow polymer matrix degradation at day 5, 10, 20 and 25. (i) Eudragit®L100 4%, (ii) 8%, (ii) 16%, and (iv) 24%. Scale bar, 400µm. e) SEM image of a characteristic sustained release microneedle and its corresponding energy dispersive x-ray elemental analysis (C, O and Mg). Scale bar, 400µm.

A SEM image of a characteristic fast-acting microneedle is shown in Figure 3c. Energy Dispersive X-ray (EDX) elemental analysis of the structure displays the microneedle composition (Figure 3.5c); as expected, elemental analysis of Mg show that Mg microparticles remain entrapped within the microneedle structure. In contrast,

sustained release microneedles (4, 8, 16 and 24% Eudragit®L100) visually demonstrated to have slow dissolution properties for days while being exposed to circumvent solution around it (Figure 3.5d), where the methacrylic acid pH sensitive co-polymer starts to dissolve at pH values above 6.0. Correspondingly, sustained release microneedles were characterized by SEM and EDX (Figure 3.5e), image shows a smooth microneedle surface and sharp tip.

To investigate the optimal formulation of the combinatorial microneedle patch we performed extensive characterization of each compartment. To evaluate whether microneedles had sufficient mechanical strength to penetrate the skin, we evaluated the mechanical performance of fast-acting and sustained release microneedles under compression (schematic of the experimental setup shown in Figure 3.6a). Results demonstrated that the microneedle strength under compression increased in both fast-acting and sustained release compartments with increasing polymer (CMC/Eudragit®L100) concentration (force displacement curve shown in Figure 3.6b and c, respectively), however, no significant difference was found among the three different polymer concentrations used as fast-acting microneedles, where 3% CMC was the most optimal formulation, considering polymer solution viscosity and easier fabrication process to fill the silicone negative molds. Moreover, the area under the curve (AUC) of each microneedle compartment was estimated up to a displacement of 300μm, where the higher the AUC value, the stronger the microneedle (Figure 3.6d).

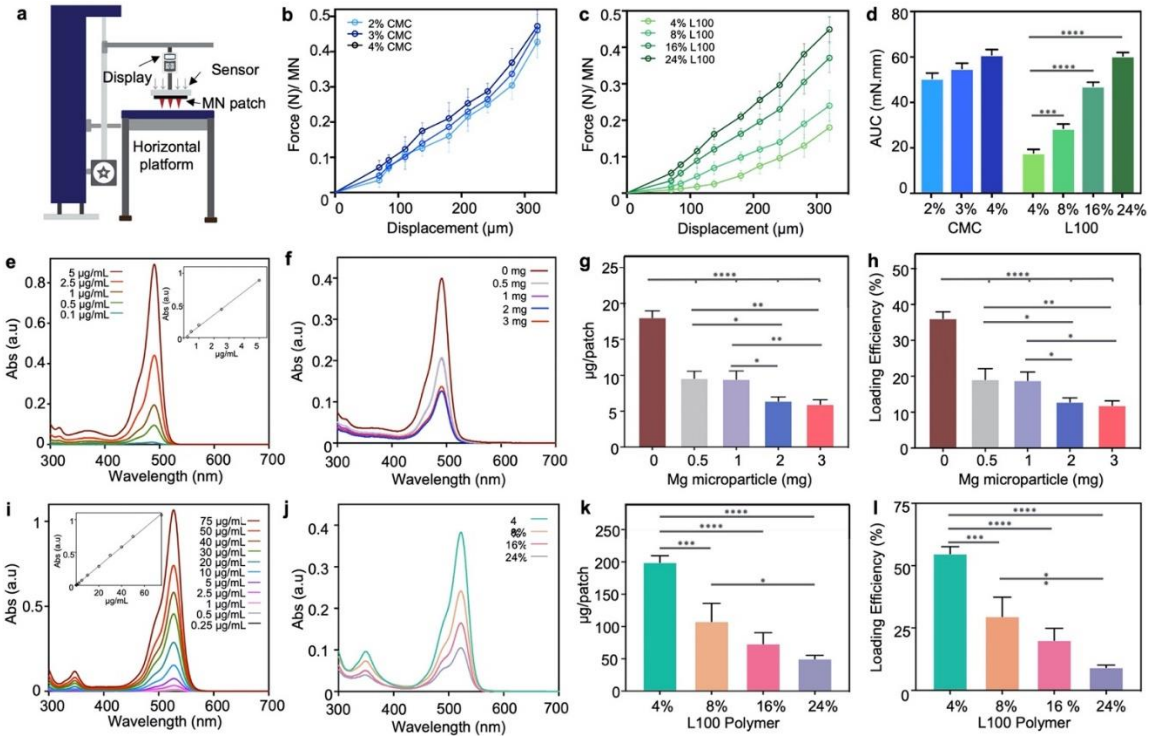

Figure 3.3.6 Mechanical properties, drug loading efficiency and microneedle compartment optimization. a) Schematic illustration of the mechanical testing stage employed. b) Mechanical strength analysis (force displacement curve) of different active microneedle formulations: 2%, 3% and 4% carboxymethyl cellulose loaded with 1 mg of Mg microparticles. Points represent means ± s.d (n=5 independent experiments). c) Mechanical strength analysis (force displacement curve) of diverse sustained release microneedle formulations: 4%, 8%, 16% and 24% Eudragit®L100. Points represent means ± s.d (n=5 independent experiments). d) Area under the curve (AUC) up to a displacement of 300 μm. A higher AUC means stronger microneedle. Data are means ± s.d (n=5). e) Fast-acting microneedle patch model payload (FITC) absorbance spectrum calibration curve. f) Active microneedle release curves from patches loaded with different amounts of Mg microparticles (0, 0.5, 1, 2 and 3mg). g) Optimization of the active microneedle compartment; micrograms of FITC loaded vs Mg microparticle packing. Bars represent means ± s.d (n=5). h) Active microneedle compartment loading efficiency vs Mg microparticle packing. Bars represent means ± s.d (n=5). i) Sustained release compartment microneedle patch model payload (Rh6G) absorbance spectrum and calibration curve. j) Sustained release microneedle release curves from patches fabricated of different microneedle formulations: 4%, 8%, 16% and 24% Eudragit®L100. k) Sustained release microneedle compartment optimization: micrograms of Rh6G loaded vs polymer concentration. Bars represent means ± s.d (n=5). l) Sustained release microneedle compartment loading efficiency vs polymer concentration Bars represent means ± s.d (n=5).Statistical significances were calculated by one-way ANOVA with Tukey's test: *$P<0.05$, **$P<0.01$, ***$P<0.001$, ****$P<0.0001$.

Although combinatorial microneedle patches with the lowest concentration were weaker, they tolerated compression forces ≥ 0.15 N needle^{-1}, value reported and expected to enable efficient and reliable skin penetration.[49]

To determine until what degree the drug loading capacity and efficiency of the fast-acting microneedle compartment could be compromised upon different amount of Mg microparticles, we examined 3% CMC fast-acting microneedles loaded with 0, 0.5, 1, 2, and 3mg of Mg microparticles. A UV-vis spectrum of the characteristic model payload (FITC) loaded, and the corresponding calibration curve (inset) is shown in Figure 3.6e. Different formulations of fast-acting microneedles were fabricated (0, 0.5, 1, 2, and 3 mg of Mg) and subjected to complete dissolution. UV-vis spectrum of the release of these arrays can be found in Figure 3.6f and the corresponding number of micrograms loaded in Figure 3.6g. As expected, we identified that regardless of the amount of Mg microparticles loaded within the fast-acting microneedle array, the relative available space to load the drug seems to be compromised and significantly reduced (~47% for 0.5mg of Mg, 49% for 1mg, 64% for 2 mg and 68% for 3mg). However, this experiment set the foundation to precisely tune the amount of drug that needed to be loaded in each patch; by just adjusting the stock payload solution we were able to fix the loading micrograms required per patch for subsequent *in vitro* release kinetics and *ex vivo* penetration studies.

Additional graph (Figure 3.6h) displays the loading efficiency of each fast-acting patch formulation, where in a very similar manner as they are closely related, the loading

efficiency seems to be reduced as the number of milligrams of Mg increase. Likewise, same characterization and optimization experiments were developed to different formulations of sustained release microneedles. A UV-vis spectrum of the characteristic model payload (Rh6G) loaded within the sustained compartment, and the corresponding calibration curve (inset) is shown in Figure 3.6i. Fabricated microneedles (4, 8, 16 and 24% Eudragit®L100) were subjected to complete dissolution. UV-vis spectrum of the release from these arrays is shown in Figure 3.6j and the corresponding number of micrograms loaded in Figure 3.6k. We identified that the polymer concentration of Eudragit®L100 and the amount of drug that can be loaded in the microneedle structure are interdependent. As the polymer concentration increases from 4-24%, the number of micrograms loaded per array is significantly reduced (~200µg for 4% L100, ~107µg for 8% L100, ~73µg for 16% L100 and ~50µg for 24% L100). This is expected due to the viscosity increments in the solutions employed (casted within the cavities of the molds) in the fabrication process, where the lower the concentration, the faster the organic solvent vaporization, therefore, higher the loading. Even though the fabrication process of combinatorial microneedle patches is very well established, the loading will tend to be higher when lower polymer concentrations are employed. Additional loading efficiency graph of sustained release microneedle compartment (Eudragit®L100) formulations is found in Figure 3.6l, clearly displaying the same behavior.

Fluorescence imaging of a characteristic combinatorial microneedle patch is shown in Figure 3.7a. The combinatorial microneedle patch image is comprised of 3% CMC (1mg/Mg) fast-acting microneedle and 16% Eudragit®L100 sustained release

microneedle compartments. Figure 3.7a(i) shows a combinatorial microneedle patch before being subjected to dissolution (t=0), clearly displaying both compartments.

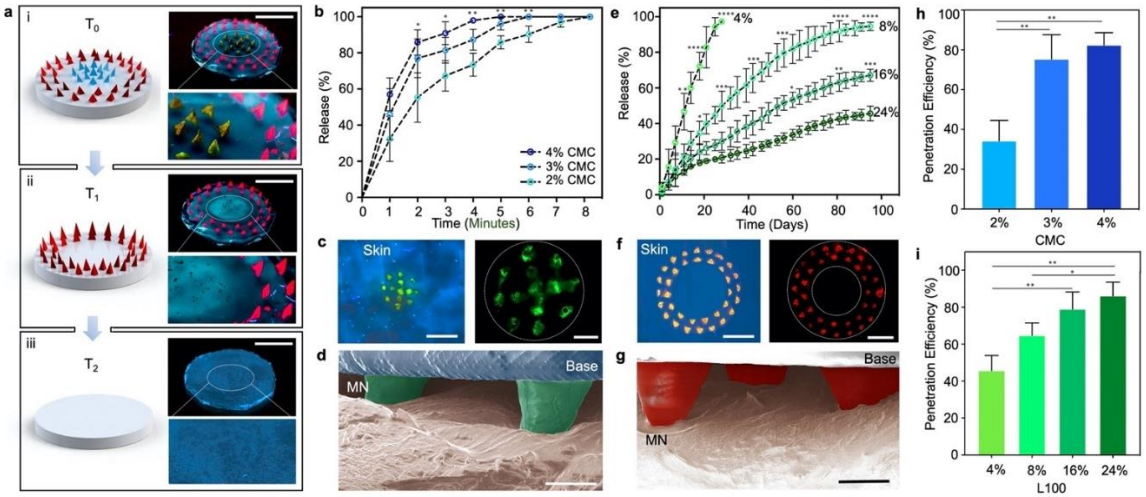

Figure 3.3.7 Dual-stage tunable release kinetics from combinatorial microneedle patch. a) Digital fluorescence photographs of the different payload delivery stages at t=0 (Before application), t=1 after active compartment dissolution (burst and fast release of FITC, and t=2 after sustained delivery of Rh6G. Scale bar, 5mm. b) Release kinetics of different formulations of the active microneedle compartment from the combinatorial microneedle array, using different CMC loadings (2%, 3% and 4%), showing a fast delivery of FITC over a period of few minutes. Points represent means ± s.d (n=5). c) Digital photograph of the microneedle patch onto cadaver porcine skin and subsequent imaging of the skin after application, under UV lamp (left) and fluorescence microscopy imaging under GFP channel (right). Scale bars, 4 and 2mm, respectively. d) Colored SEM image depicting an active microneedle compartment piercing porcine skin. Scale bar, 500 µm. e) Tunable release kinetics from the sustained compartment of the combinatorial microneedle array: the prolonged delivery of Rh6G is achieved from weeks to months (in connection to Eudragit®L100 polymer concentrations of 4%, 8%, 16% and 24%). Points represent means ± s.d (n=5). f) Digital photograph of sustained release compartment microneedle after piercing porcine cadaver skin, under UV lamp (left) and fluorescence microscopy imaging under RFP channel (right). Scale bars, 4 and 2.5mm, respectively. g) Colored SEM image depicting a sustained microneedle compartment piercing porcine cadaver skin. Scale bar, 500 µm. h) Percentage penetration of active microneedle in porcine skin. Bars represent means ± s.d (n=5). i) Percentage penetration of sustained release microneedle in porcine skin. Bars represent means ± s.d (n=5). Statistical significances were calculated by one-way ANOVA with Tukey's test: **P<0.05, **P<0.01, ***P<0.001, ****P<0.0001.*

Dual release kinetics from combinatorial microneedle patches was performed *in vitro* using release media of saline buffered solution PBS pH 7.4 (chosen to simulate *in vivo* transdermal release kinetics).[48] FITC release from the fast-acting microneedle compartment (with 2, 3, and 4% CMC) showed a burst release within the first minutes (Figure 3.7b). All three patches were fairly consistent over time with no significant difference in release within this short period of time (<8 min). Release percentage of the different patch formulations at 2 min are: 2% CMC (85±7%), 3% CMC (76±10%) and 4% CMC (55±13%) and at 5 min are: 2% CMC (100%), 3% CMC (96±3%) and 4% CMC (85±4%). This data indicates that the fast-acting microneedle compartment can deliver rapid onset of payloads, achieving the target delivery timeframe in few minutes. The 3% CMC fast-acting microneedle compartment was manually applied to cadaver porcine skin and imaged in Figure 3.7c under UV lamp and fluorescence microscopy imaging under green fluorescence protein (GFP) channel.

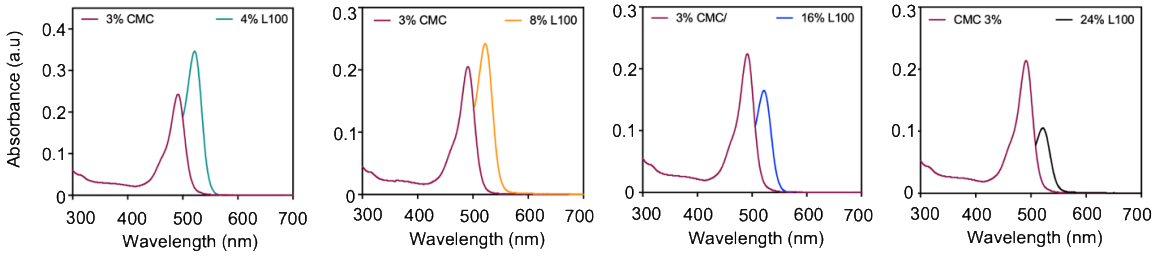

Figure 3.3.8 UV-vis absorbance curves of the release of combinatorial microneedle patches (fix fast acting microneedle compartment 3% CMC-FITC + variable Eudragit®L100/Rh6G (4-24%)

A pseudo-colored SEM image displays the penetration of two fast-acting microneedles in green to the skin (Figure 3.7d); these images show that microneedles

penetrated skin efficiently. Furthermore, the release kinetics from the sustained (slow) release microneedle compartment (4, 8, 16 and 24% Eudragit®L100) showed no initial burst release on day 1 (Figure 3.7e), with a constant Rh6G release over time (ranging from ~0.4 to ~3.8% Rh6G release per day, depending on the polymer concentration). By using 4% Eudragit®L100, the payload was released within 28 days, while using higher Eudragit®L100 concentrations resulted in longer time-frame delivery period exceeding 90 days (combinatorial microneedle release absorbance curves are shown in Figure 3.8).

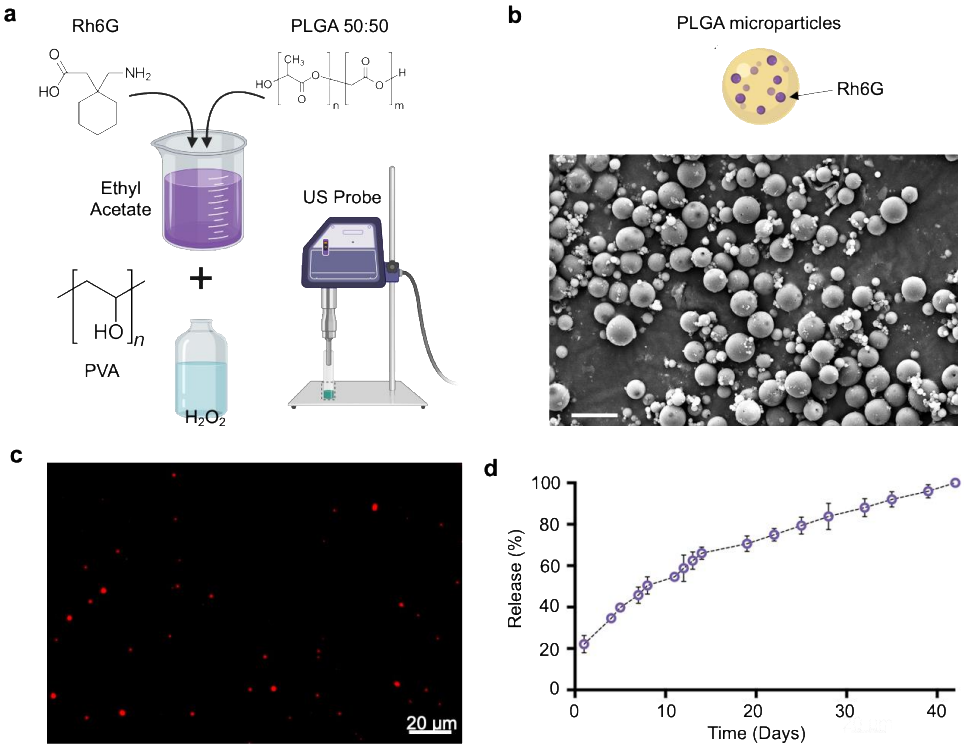

Figure 3.3.9 PLGA microparticle sustain release approach. a) PLGA microparticle formulation. b) SEM of PLGA microparticles. Scale bar, 10 µm. c) Fluorescence microscopy image (RFP channel) of PLGA microparticles loaded with Rh6G. Scale bar, 20 µm. d) Release curve Rh6G from PLGA microparticles.

These release profiles clearly illustrate the ability to tune the sustained release for period ranging from weeks to months through control of the Eudragit®L100 loading. Additional data on an alternative delivery system by the microencapsulation of Rh6G was developed by synthetizing PLGA microparticles; in contrast to our combinatorial patch, PLGA microparticles deliver full dosages within ~40 days, corresponding data of the release and procedures can be found in Figure 3.9. The 16% Eudragit®L100 sustained microneedle compartment was manually applied to cadaver porcine skin and imaged in Figure 3.7f under UV lamp and fluorescence microscopy imaging under RFP channel. Images display that the microneedle patch penetrated skin efficiently; additionally, a pseudo-colored SEM image displays the penetration of three fast-acting microneedles in red to the skin (Figure 3.7g). Combinatorial microneedle patches were applied to porcine skin and the penetration efficiency of both fast-acting and sustained compartments is shown in graph (Figure 3.7h and i, respectively). As expected, increasing the polymer concentration improved the skin penetration, regardless of the polymer used in the fabrication process. The majority of needles were able to breach dermal barriers in an efficient matter, delivering the payload and remained fully embedded under the skin surface.

3.4 Conclusions

We developed a combinatorial microneedle patch with dual and tunable release kinetics, aimed at providing greater access in delivering wide range of therapeutics with variable target delivery timeframes in a single application. The patch was fabricated to be comprised of two microneedle compartment zones: a fast-acting and a sustained release

compartment. The dual release properties of the patch with different dissolution time frame is attributed to the ability of the patch to load several drugs (even with different solubility and incompatible) within the same array, but spatially resolved, due to the additive manufacturing process employed. microneedle compartments in such combinatorial array can thus be engineered and tailored to present different release kinetics based on the specific materials and compositions used in fabrication. More encouragingly, we demonstrate that the combinatorial patch can be programmed to deliver drug payloads faster in minutes, greatly enhancing the release when compared to passive microneedles, but additionally, can deliver dosages that last over the course of weeks-to-months, for up to >90 days, with constant release over time. We envision that using different active microengine materials will allow tailoring the burst release profiles of the new ballistic microneedle. This novel combinatorial microneedle patch is expected to improve therapeutic efficacy and improve patient compliance towards substantially enhanced pain management. In the absence of effective treatment modalities for neuropathic pain, we envision that the new patch has the potential to improve control of postoperative pain of current therapy platforms, achieving powerful benefits by single patch application, decreasing daily injections, localizing the treatment, thus increasing efficacy. The new concept is expected to benefit a wide range of medical situations, beyond pain management.

Chapter 3 is based, in part, on the material as appears in Journal of Materials Chemistry B, 2021, by Miguel Angel Lopez Ramirez, Daniel Kupor, Leonardo Marchiori, Fernando Soto, Ricardo Rueda, Maria Reynoso, Lakshmi Rekha Narra,

Krishnan Chakravarthy, Joseph Wang. The dissertation author was the primary investigator and author of this paper.

3.5 References

1. E. Larrañeta, M. T. McCrudden, A. J. Courtenay, R. F. Donnelly, Pharm. Res. 2016, 33, 1055.

2. D. D. Zhu, X. P. Zhang, B.-L. Zhang, Y. Y. Hao, X. D. Guo, Adv. Ther. 2020, 3, 2000033.

3. H. Lee, T. K. Choi, Y. B. Lee, H. R. Cho, R. Ghaffari, L. Wang, H. J. Choi, T. D. Chung, N. Lu, T. Hyeon, S. H. Choi, Nat. Nanotechnol. 2016, 11, 566.

4. W. Chen, R. Tian, C. Xu, B. C. Yung, G. Wang, Y. Liu, Q. Ni, F. Zhang, Z. Zhou, J. Wang, G. Niu, Nat. Commun. 2017, 8, 1.

5. M. Zhu, Y. Liu, F. Jiang, J. Cao, S. C. Kundu, S. Lu, ACS Biomater. Sci. Eng. 2020, 6, 3422.

6. R. Jamaledin, C. K. Yiu, E. N. Zare, L. N. Niu, R. Vecchione, G. Chen, Z. Gu, F.-R. Tay, P. Makvandi, Adv. Mater. 2020. 32, 2002129.

7. M. Yin, L. Xiao, Q. Liu, S. Y. Kwon, Y. Zhang, P.-R. Sharma, L. Jin, X. Li, B. Xu, Adv. Healthc. Mater. 2019, 8, 1901170.

8. X. Xie, C. Pascual, C. Lieu, S. Oh, J. Wang, B. Zou, J. Xie, Z. Li, J. Xie, D. C. Yeomans, M.-X. Wu, ACS nano 2017, 11, 395.

9. J. Arya, M. R. Prausnitz, J. Control. Release 2016, 240, 135.

10. H. Lee, C. Song, S. Baik, D. Kim, T. Hyeon, D. H. Kim, Adv. Drug Deliv. Rev. 2018, 127, 35.

11. K. Van der Maaden, W. Jiskoot, J. Bouwstra, J. Control. Release 2012, 161, 645.

12. S. Marshall, L. J. Sahm, A. C. Moore, Hum. Vaccin. Immunother. 2016, 12, 2975.

13. J. J. Norman, J. M. Arya, M. A. McClain, P. M. Frew, M.-I. Meltzer, M. R. Prausnitz, Vaccine 2014, 32, 1856.

14. N. G. Rouphael, M. Paine, R. Mosley, S. Henry, D. V. McAllister, H. Kalluri, W. Pewin, P. M. Frew, T. Yu, N. J. Thornburg, S. Kabbani, L. Lai, E. V. Vassilieva, I. Skountzou, R. W. Compans, M. J. Mulligan, M. R. Prausnitz, Lancet 2017, 390, 649.

15. S. Bhatnagar, K. Dave, V. V. K. Venuganti, J. Control. Release 2017, 260, 164.

16. T. A. Petukhova, L. A. Hassoun, N. Foolad, M. Barath, R. K. Sivamani, JAMA Dermatol. 2017, 153, 637.

17. R. F. Donnelly, D. I. Morrow, M. T. McCrudden, A. Z. Alkilani, E. M. Vicente-Pérez, C. O'Mahony, P. González-Vázquez, P. A. McCarron, A. D. Woolfson, Photochem. Photobiol. 2014, 90, 641.

18. R. F. Donnelly, T. R. R. Singh, M. J. Garland, K. Migalska, R. Majithiya, C. M. McCrudden, P. L. Kole, T. M. T. Mahmood, H. O. McCarthy, A. D. Woolfson, Adv. Funct. Mater. 2012, 22, 4879.

19. M. T. McCrudden, A. Z. Alkilani, A. J. Courtenay, C. M. McCrudden, B. McCloskey, C. Walker, N. Alshraiedeh, R. E. Lutton, B. F. Gilmore, A. D. Woolfson, R. F. Donnelly, Drug Deliv. Transl. Res. 2015, 5, 3.

20. Y. C. Ryu, D. I. Kim, S. H. Kim, H. M. D. Wang, B. H. Hwang, Biotechnol. Bioprocess Eng. 2018, 23, 286.

21. C. Wang, Y. Ye, G. M. Hochu, H. Sadeghifar, Z. Gu. Nano Lett. 2016, 16, 2334.

22. P. C. DeMuth, X. Su, R. E. Samuel, P. T. Hammond, D. J. Irvine, Adv. Mater. 2010, 22, 4851.

23. U. Angkawinitwong, A. J. Courtenay, A. M. Rodgers, E. Larrañeta, H. O. McCarthy, S. Brocchini, R. F. Donnelly, G. R. Williams, ACS Appl. Mater. Interfaces 2020, 12, 12478.

24. X. Lan, J. She, D. A. Lin, Y. Xu, X. Li, W. F. Yang, V. W. Y. Lui, L. Jin, X. Xie, Y. X. Su, ACS Appl. Mater. Interfaces 2018, 10, 33060.

25. J. H. Park, M. G. Allen, M. R. Prausnitz, Pharmaceutical research, 2006, 23, 1008.

26. Y. Zhang, Q. Liu, J. Yu, S. Yu, J. Wang, L. Qiang, Z. Gu, ACS nano, 2017, 11, 9223.

27. W. Li, R. N. Terry, J. Tang, M. R. Feng, S.-P. Schwendeman, M. R. Prausnitz, Nat. Biomed. Eng. 2019, 3, 220.

28. W. Li, J. Tang, R. N. Terry, S. Li, A. Brunie, R. L. Callahan, R. K. Noel, C. A. Rodríguez, S. P. Schwendeman, M. R. Prausnitz, Sci. Adv. 2019, 5, eaaw8145.

29. A. V. Boopathy, A. Mandal, D. W. Kulp, S. Menis, N. R. Bennett, H. C. Watkins, W. Wang, J. T. Martin, N. T. Thai, Y. He, W. R. Schief, PNAS, 2019, 116, 16473.

30. S. Wang, M. Zhu, L. Zhao, D. Kuang, S. C. Kundu, S. Lu, ACS Biomater. Sci. Eng. 2019, 5, 1887.

31. K. T. M. Tran, T. D. Gavitt, N. J. Farrell, E. J. Curry, A. B. Mara, A. Patel, L. Brown, S. Kilpatrick, R. Piotrowska, N. Mishra, S. M. Szczepanek, T. D. Nguyen, Nat. Biomed. Eng. 2020, DOI 10.1038/s41551-020-00650-4

32. Z. Wang, J. Wang, H. Li, J. Yu, G. Chen, A.-R. Kahkoska, V. Wu, Y. Zeng, D. Wen, J. R. Miedema, J. B. Buse, PNAS 2020, 117, 29512.

33. E. Drucker, P. G. Alcabes, P. A. Marx, Lancet 2001, 358, 1989.

34. M. A. Lopez-Ramirez, F. Soto, C. Wang, R. Rueda, S. Shukla, C. Silva-Lopez, D. Kupor, D. A. McBride, J. K. Pokorski, A. Nourhani, N. F. Steinmetz, N. J. Shah, J. Wang, Adv. Mater. 2020, 32, 1905740.

35. C. E. Boone, C. Wang, M. A. Lopez-Ramirez, V. Beiss, S. Shukla, P. L. Chariou, D. Kupor, R. Rueda, J. Wang, N. F. Steinmetz, ACS Appl. Nano Mater. 2020, 3, 8037.

36. A. Devers, B. S. Galer, Clin. J. Pain, 2000, 16, 205.

37. J. Kennedy, J. M. Roll, T. Schraudner, S. Murphy, S. McPherson, J. Pain 2014, 15, 979.

38. B. Mandal, D. Das, A. P. Rameshbabu, S. Dhara, S. Pal, RSC Adv. 2016, 6, 19605.

39. K. Bekkour, D. S. Waterhouse, S. S. Wadhwa, Food Res. Int. 2014, 66, 247.

40. R. Biswal, R. P. Singh, Carbohydr. Polym. 2004, 57, 379.

41. Y. Chenga, B. Fengb, X. Yanga, P. Yanga, Y. Dinga, Y. Chena, Sens. Actuators, B, 2013, 182, 288.

42. B. Mukherjee, S. Mahapatra, R. Gupta, B. Patra, A. Tiwari, P. Arora, Eur. J. Pharm. 2005, 59, 475.

43. P. Minghetti, A. Casiraghi, F. Cilurzo, L. Montanari, Eur. J. Pharm, 2000, 10, 111.

44. S. Tokunaga, K. Ono, S. Ito, T. Sharmin, T. Kato, K. Irie, K. Mishima, T. Satho, T. Harada, T. M. Aida, K. Mishima, J. Supercrit. Fluids, 2021, 167, 105044.

45. M. Cetin, A. Atila, Y. Kadioglu, AAPS Pharm SciTech 2010, 11, 1250.

46. B. Esteban-Fernández de Ávila, M. A. Lopez-Ramirez, R. Mundaca-Uribe, X. Wei, D. E. Ramírez-Herrera, E. Karshalev, B. Nguyen, R. H. Fang, L. Zhang, J. Wang, Adv. Mater. 2020, 32, 2000091.

47. X. Lan, W. Zhu, X. Huang, Y. Yu, H. Xiao, L. Jin, J. J. Pu, X. Xie, J. She, V. W. Y. Lui, H. J. Chen, Nanoscale, 2020, 12, 18885.

48. M. Wang, Y. Han, X. Yu, L. Liang, H. Chang, D. C. Yeo, C. Wiraja, M. L. Wee, L. Liu, X. Liu, C. Xu, Adv. Healthc. Mater. 2020, 9, 1900635.

49. M. R. Prausnitz, Adv. Drug Deliv. Rev. 2004, 56, 581.

Chapter 4. Summary and Perspectives

4.1 Summary

In this dissertation, the research has been focused on the demonstration of unique and innovative active microneedle systems for enhanced drug delivery in biomedical applications. The principal achievements of this dissertation include:

1) The development of an autonomous and degradable, active microneedle platform/device. This study demonstrated that magnesium microparticles entrapped within microneedle structures work as built-in engines (micropumps) for deeper and faster intradermal therapeutic delivery. Moreover, the *in vivo* performance of the active microneedle platform results in greatly enhanced immune response and significantly longer survival in a B16F10 mouse melanoma model.
2) A versatile and effective *in situ* active microneedle vaccination system for the direct intratumoral delivery of an immunoadjuvant, cowpea mosaic virus nanoparticles, *in vivo*. The application of the active vaccination delivery platform demonstrated substantially more pronounced tumor regression and prolonged survival of tumor-bearing mice.
3) A dual-action combinatorial programmable microneedle system by integrating fast and sustained-release compartments with tunable release kinetics. We demonstrate that the fine tuning of microneedle materials allows the device to be tailored to deliver initial payloads in minutes, while simultaneously deliver a second drug over prolonged period of times ranging from weeks to months.

4.2 Perspectives

In summary, we have presented the opportunities, challenges, and advantages of conventional and active microneedle platforms in the biomedical field. The current accomplishments exemplify the versatility, dynamism, and effectiveness of the active microneedle delivery technology; nevertheless, only demonstrate the first initial steps toward broad biomedical applications.

Although microneedles were originally introduced towards the delivery of drugs or vaccines transdermally, to date, extensive research has been devoted in the development of flexible devices via different routes of application (e.g., eye, oral cavity, GI tract or brain).

Additional efforts/innovations should be pursued towards the development of next generation of microneedle systems by the incorporation of different types of activation particles (e.g., metal catalysts, biocatalytic enzymes, nanoparticles, or metal organic frameworks) within degradable and dissolvable polymeric structures for enhanced drug delivery. To address this, the microneedle field requires new material science perspectives, with consideration in the chemical and mechanical *in vivo* performance of the devices, and critical knowledge in immunology to fully understand the immune response after application. Moreover, the clinical translation of new microneedle devices should be considered a critical and essential step towards great adoption of the technology.

With the development of new micro-nano-manufacturing technology, the microneedle technology is believed to revolutionize the way healthcare is currently being managed and bring exciting new breakthroughs in the biomedical field. Such active microneedle devices are considered a promise for a wide range of therapeutic applications, achieving powerful benefits toward greatly enhanced outcome, patient compliance, convenience at low manufacturing cost. We envision a future where microneedle systems would be capable of being employed at home, from skin-care applications, pain control, vaccines to more complicated treatments that often require hospital attendance.

Chapter 4 is based, in part, on the material as appears in Advanced Materials, 2020, by Miguel Angel Lopez Ramirez, Fernando Soto, Chao Wang, Ricardo Rueda, Sourabh Shukla, Cristian Silva Lopez, Daniel Kupor, David A. McBride, Jonathan K. Pokorski, Amir Nourhani, Nicole F. Steinmetz, Nisarg J. Shah, Joseph Wang. The dissertation author was the primary investigator and author of this paper.